Effect of mechanical deformation and microstructural evolution on the magnetic performance of Soft Magnetic Composite components

Investigation of the deformation behaviour and microstructural evolution of Soft Magnetic Composite components under compaction and heat treatment processing steps, and their direct relationship to their magnetic performance.

by

DANIEL CASTILLO GUTIÉRREZ

Diploma work No. 166/2015

at Department of Materials and Manufacturing Technology
CHALMERS UNIVERSITY OF TECHNOLOGY
Gothenburg, Sweden

Diploma work in the Master program Materials Engineering

Performed at:

Department of Materials and Manufacturing Technology
Chalmers Univ. of Tech.
41296 Gothenburg, Sweden

Department of Soft Magnetic Composite Technology
Höganäs AB
26383, Höganäs, Sweden

Micro and Nano-Mechanics Program
IMDEA Materials Institute
28906, Madrid (Spain)

Main Supervisor: Tekn. Lic. Christos Oikonomou[1]

Co-Supervisors: Dr. Ann-Cathrin Hellsén[2]
Prof. Uta Klement[1]
Prof. José Manuel Torralba Castello[3]

Examiner: Prof. Lars Nyborg[1]

1)
Department of Materials and Manufacturing Technology
Chalmers University of Technology
SE412 96 Gothenburg

2)
Soft Magnetic Composite Technology
Höganäs AB
26383 Höganäs, Sweden

3)
Departamento de Ciencia e Ing. de Mat.
Universidad Carlos III de Madrid
28911 Leganés, Spain

Effect of mechanical deformation and microstructural evolution
on the magnetic performance of Soft Magnetic Composite components

Investigation of the deformation behaviour and microstructural evolution of Soft Magnetic Composite components under compaction and heat-treatment processing steps and the direct relationship to their magnetic properties

DANIEL CASTILLO GUTIÉRREZ

Department of Materials and Manufacturing Technology
Chalmers University of Technology

SUMMARY

Soft Magnetic Composite (SMC) components designed for electromagnetic applications are being produced based on traditional Powder Metallurgy (PM) techniques. The latter provide profitable and sustainable production routes that yield net-shaped parts, optimizing the number of post-operations after compaction besides annealing processes. The concept of SMC technology is based on encapsulating each individual iron particle with a thin electrically insulating surface coating and subsequently pressing them together in a three dimensional array to form a finished compact. In this manner, uniform and isotropic 3D magnetic properties are acquired that offer design freedom in creating unique and innovative application concepts, as opposed to the more traditionally used laminated steels. The SMC products exhibit improved magnetic performance for a wide range of frequency applications, due to the fact that they offer higher bulk electrical resistivity by effectively confining the deleterious effects of core losses, especially in high frequency applications. Equally important to the insulating coating is the microstructure of the SMC parts and its evolution thorough the manufacturing process. Investigations on this context are important as to improve and tailor the process in producing parts of desired properties. The objective of this thesis work was to implement techniques and methods that would provide valid information on the microstructural evolution and magnetic behaviour of SMC along different steps of the production process. The development of internal microstructure and grain orientation of the powder particles under different processing conditions has been assessed by means of Electron Backscatter Diffraction (EBSD) technique, emphasizing the degree of mechanical deformation based on misorientation maps, as well as the subsequent recovery and recrystallization of the components. Additional mechanical tests done by nanoindentation have been correlated to the EBSD analysis, in order to quantify the degree of contribution of the aforementioned factors to the magnetic properties of the SMC parts. The contribution from factors related to particles characteristics, i.e. grain size and amount of plastic strain were also investigated and the results were correlated to the magnetic behaviour.

Keywords: Soft Magnetic Composites (SMC), Electron Backscattered Diffraction (EBSD), magnetic properties, nanoindentation, microstructural characterization, Powder Metallurgy (PM)

Cover:
Powder particle images constructed by EBSD technique showing strain state through low angle boundaries.

Chalmers Reproservice
Gothenburg, Sweden 2015

Table of Contents

List of Acronyms

SMC	Soft Magnetic Composites
PM	Powder Metallurgy
SEM	Scanning Electron Microscopy
EBSD	Electron Backscattered Diffraction
BC	Band Contrast
LAB	Low Angle Boundaries
HAB	High Angle Boundaries
IPF	Inverse Pole Figure
AC	Alternating Current
DC	Direct Current
3D	Three Dimension (s/al)
SE	Secondary Electrons
FSD	Force Scattered Detector
WD	Working Distance
B	Magnetic Flux density
H	Magnetic Field Applied
μ	Magnetic Permeability / Permitivity

1. Introduction

In the introduction section, the background of the subject will be presented together with some literature research on Soft Magnetic Composites (SMC), followed by the topic description including purpose, delimitations, disposition and contribution.

Soft Magnetic Composite materials designed for electromagnetic applications are produced based on traditional Powder Metallurgy (PM) techniques. The concept of SMC technology is based on encapsulating each individual iron particle with a thin electrically insulating surface coating and subsequently pressing them together in the required three dimensional shape. Although, the idea of iron based composites appeared more than 100 years ago, the first iron-resin components were rarely used due to the underdeveloped processing technology (1). These initial limitations were overcome with the development of improved raw materials and new shaping technologies. Nowadays, SMC components find increasing use in electrical applications such as DC motors, inductors, filters, etc.; replacing existing laminate materials and providing competitive magnetic properties (2) (3).

The aim of this thesis is to understand both the principles and applications of SMC from a material engineering point of view, relating the manufacturing process and the obtained microstructures to the final properties of the material.

1.1 Background

The interest in SMC products has accelerated over the last few years (1) (4), owing to the fact that recent advances in materials development and production with unique physical properties show great potential for technological applications. Possible applications for SMC materials range from power distribution to data storage in information systems. In addition, these components present several advantages, such as considerable weight and size reduction, along with other powder based material strong points, mass production and economic viability in manufacturing. Powder Metallurgy (PM) technology provides profitable and sustainable production routes that yield net-shaped parts, optimizing the number of post-operations apart from the annealing processes after compaction.

Basic understanding of PM technology as well as the basics of the SMC concept will be reviewed as part of the theoretical background (Chapter 2). As opposed to more conventional PM techniques, production of SMC parts does not require sintering since that would compromise the viability of the insulating coating. Conversely, a heat treatment at lower temperatures is performed in order to relax stresses, which are introduced during the compaction process step, improving thus the magnetic induction of the part and promoting curing of the surface layer for mechanical strengthening. Permeability and other magnetic parameters also experience improvement. Fully processed components were produced and analyzed in the current investigation in order to accurately determine the crystallographic state of the material of interest. Additionally, considerations regarding the relaxation of internal strain in the components are addressed in respect to the different compaction and annealing processes.

1.2 Research Questions

The SMC products exhibit improved magnetic performance for a wide range of frequency applications, due to the fact that they offer higher bulk electrical resistivity by effectively confining the deleterious effects of core losses, especially at high frequencies. Besides usual issues for PM materials, such as porosity and weaker mechanical properties, microstructural state characterization and its direct relationship to the magnetic behaviour remains under investigation.

- Are the core losses related to the microstructure of the SMC component?
- How do the manufacturing processes in PM influence the magnetic flux within the material?
- Can magnetic and mechanical properties be correlated by means of electronic microscopy?

1.3 Purpose

From the above, it becomes apparent that the insulating coating is equally important as the microstructure of the SMC. Investigations of the nature and behaviour of the microstructure evolution through the manufacturing process are required to improve and tailor the process and produce parts of desired properties. The objective of this thesis work is to providing valid information on the microstructural evolution and magnetic behaviour of SMC at different steps of the production process. From the point of view of material engineering, this project is also trying to relate the microstructure, to the magnetic and mechanical properties.

1.4 Disposition

One mix of SMC powder and lubricant was completely analysed, considering three different compaction pressures and five different heat treatment temperatures. In the following chapter, a review on material science and materials technology will take place, focusing on PM, SMC, mechanical and magnetic properties of metals, in addition to texture of crystalline materials. Thereafter, experimental techniques will be explained, as well as relevant results obtained. Additional measurements are included in the Appendix. Finally, a discussion of the correlation of the different techniques is followed by a conclusion. Acknowledgments and references are also included in the present project work.

1.5 Research Contribution

The development of internal microstructure and grain orientation of the powder particles under different processing conditions has been assessed by means of Electron Backscatter Diffraction (EBSD) technique; emphasizing the degree of mechanical deformation based on misorientation maps, as well as the subsequent recovery and recrystallization of the components. Additional mechanical tests performed by nanoindentation have been correlated to the EBSD analysis, in order to quantify the degree of contribution of the aforementioned factors to the magnetic properties of the SMC parts. To serve this purpose, all the samples have been subjected to magnetic tests in order to state the core losses and correlate them to the microstructural component status.

The contribution from factors related to powder microstructural characteristics, such as grain size, amount of strain and recrystallization state were evaluated by correlating results to the magnetic behaviour. Discussion of the state of the microstructure, and their effect on the hardness and core loss properties are still open to interpretation. However there are certainly microstructural features that should be taken into account when assessing behaviour of powder based materials, as it has already been done with metals obtained through conventional metallurgical methods.

2. Theoretical Background

2.1 Powder Metallurgy

Powder Metallurgy (PM) refers to a series of techniques applied to manufacturing metallic net-shape components starting from a powder base. Among the advantages of this technology are the ability to produce large product quantities with high tolerances and low cost, the flexibility in the range of materials, properties and control over the microstructures obtained as well as the low production cost of the overall process. In essence, PM takes a metal powder of a specific composition and converts it through compaction and heat treatments into strong and precise shape. The key parameters are summarized in Figure 2.1a below, where the interdependence between several aspects of PM can be appreciated (4).

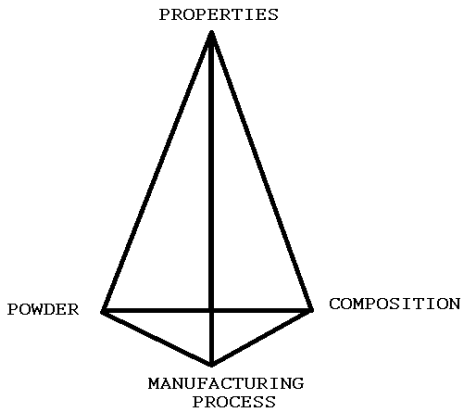

Figure 2.1a – Elements involved in Powder Metallurgy (4)

This fabrication technology can be considered to have four basic steps: powder production, compaction, sintering and secondary operations. The initial part after compaction is denominated *green*, and the shape of the component is maintained through the following steps. Subsequent heat treatments produce dimensional changes on the pieces due to the bonding between the particles changes. This process is known as *sintering* and it is normally achieved on temperatures below the melting point, so the geometry of the parts is maintained. The components using this technique have lower mechanical properties than conventional metallurgical ones. However today it is possible to produce components with high reliability and performance. Besides, in the case of some applications, PM is the only alternative possible. Either the final part presents the best properties processed this way or PM is the unique technique for processing a specific material (5).

There exists many ways of producing metal powder: reduction of oxides, precipitation from solution, electrolytic deposition, grinding or crushing them to name a few. However the dominant mode of powder fabrication is atomization. The major event in the production of finely divided metal is the generation of new surfaces. Powder based materials present the highest ratio surface-volume, which is of vital importance when understanding chemical reaction or compression effects on powder particles. Control of size, shape and surface morphology of the powder particles is possible in several modes of atomization. In addition, atomization allows a high degree of flexibility in alloying powders as well as profitable high production rates. This technique is considered to be a rapid solidification since droplets experience convective cooling. Among the commercial methods of atomization there are two predominant: water and gas atomization. The basis of both methods are really similar, however water atomization is cheaper than other methods, since it is intrinsically a high volume and low cost process. As can be seen in Figure 2.1b, whatever fluid employed over the molten metal, it results in ellipsoidal particles (6).

Diverse size and shapes of powder rely on the manufacturing process, from flakes to ellipsoidal, which is the case of atomized metal powder. Referring to size, powder metallurgists pay attention to the distribution of sizes, not to the average size. The difference between gas and water atomized metal powders though can be found in the nature of the particle surface. While water atomized powder is rounded, with an irregular shape, gas atomized is almost perfect spherical. The first type is prone to mechanical joining due to surface roughness, while the second one is thought as a sintering. Moreover, water atomization oxidizes the powder more than gas atomization, so the surface reactivity would be completely different between them. Powder characterization, as it has been described above, it is the key to define the optimal process, that is, the pressures used in compaction, and the temperatures used in subsequent heat treatments (7) (8).

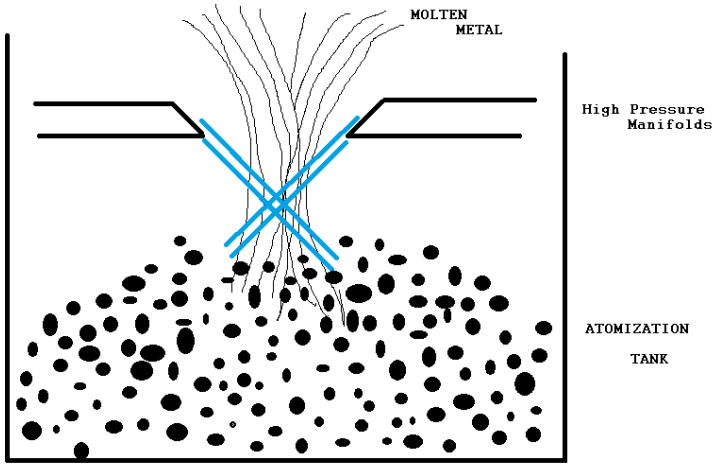

Figure 2.1b – Atomization Process (6)

In the specific field of powders used for magnetic applications, the properties rely on purity and processing parameters. These materials are used in unsintered form, although thermal treatment for stress release is advisable in order to optimized magnetic properties. Field properties describing materials response in magnetic fields (for example magnetic permeability), depend in a complicated manner on porosity and pore geometries as well. Another property controlled by the mass of a given composition is, for example, the magnetic saturation (9). To sum up, any disruption of the uniform magnetic field is detrimental to soft magnetic properties and for that purpose a low interstitial level, high density and coarse grain are generally desirable. Moreover, a high density raises the maximum permeability and lowers the coercive force (7).

Magnetic parts are fabricated from water atomized metal powders, with the exception of MIM (Metal Injection Moulding), which employs gas-atomized powder. Water atomized powders are -100 mesh powders with a normal distribution, in order to achieve the highest green density possible. The higher the compaction pressure, the higher density, and consequently the higher magnetic induction and amount of flux carried by a given cross section. However, fabricator and user must agree on the critical density of the section, generally between 6,8 and 7,2 g/cm^3. Avoiding variations within the cross section, as well as carbon and nitrogen, are important, parameters that should be borne in mind when designing the piece and the PM process ahead (8).

2.2 Mechanical Properties in metals

Mechanical properties of metals, as any other property of materials, are directly related to crystal structures. Metals are characterized by the metallic atomic bonding and the notion of "order" specified in terms of a unit cell. Crystalline materials, such as metals have the atoms disposed in repeating or periodic array over large atomic distances. Atoms and ions are thought as solid spheres, where nearest neighbour atom touch one another. The term lattice is used to define the 3D array of points coinciding with atoms positions or sphere centres. A relatively common crystal structure is the body centred cubic (BCC), depicted on Figure 2.2a, where two atoms fit inside a single unit cell, taking sections from 8 different atoms (10).

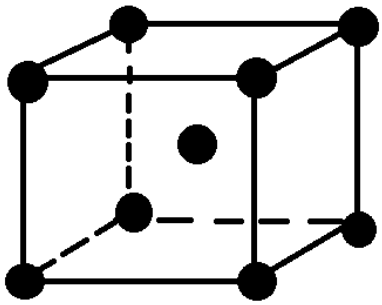

Figure 2.2a – Unit Cell of a Body Centred Cubic Structure (BCC) (11)

The vast majority of crystalline solids are polycrystalline; being composed of many small crystals or grains, where a grain boundary is the line where two crystallographic orientations meet, giving birth to an atomistic mismatch. Low Angle Grain Boundaries (LAGB or LAB) between adjoining crystal grains consist of arrays of dislocations. The boundaries tilt, generating misorientations that can be described as a rotation over the common axis of the crystal relative to the other. In Figure 2.2b the beginning of the dislocation is represented by the arrow. This distribution of dislocations along small-angle grain boundaries has been proved experimentally and further developed into a theory of interfacial energy (12).

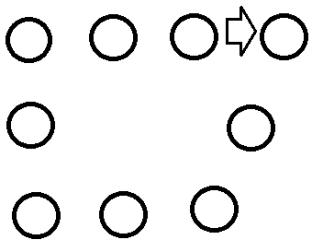

Figure 2.2b – Initial dislocation in a low angle grain boundary (12)

Order and crystalline influence the final mechanical properties of metals, and what it is understood by mechanical properties specifically is the behaviour of materials when subjected to loads. Designing requires the knowledge of properties such as hardness, toughness, stiffness, strength and ductility in order to avoid fracture of the materials in service. Mechanical behaviour of metals can be divided in elastic and plastic zones. In the first one, stress and strain are proportional to each other through a relationship known as the Hooke's law:

$$\sigma = E\epsilon \qquad \text{(Eq. 2.2)}$$

where σ is the stress, ϵ is the strain to which the material is subjected. The constant of proportionality also known as the Elastic or Young Modulus is noted by an E.

The simplest way to visualize tensile tests, and mechanical properties during increasing stress conditions is a stress-strain curve, see Figure 2.2c. The stress is the force per unit area, expressed according to the International System (SI) of units in Pa (N/m^2). The deformation or strain, ϵ, has no units since it is the fractional change in length ($\Delta l/l_0$, where l_0 is the initial length considered) (13).

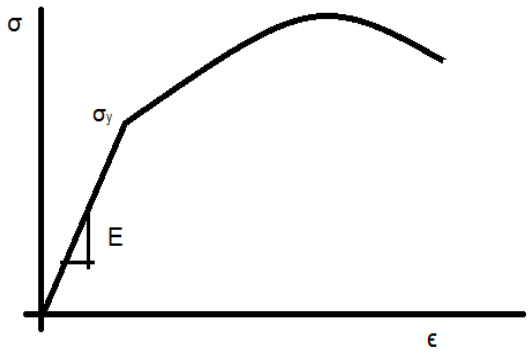

Figure 2.2c – Typical Stress- Strain curve for a metallic material (13)

At some point around a deformation of 0,005, stress and strain are not proportional anymore. This is considered the plastic zone, were metals experience irreversible deformations. Even though it is difficult to identify the yielding point where the elastic/plastic transition occurs, the consensus is that it usually occurs around a deformation of 0,002. The stress corresponding to that strain is called the Yield strength; σ_y. After yielding, the stress necessary to continue plastic deformation increases to a maximum point, denominated tensile strength (TS), and then decreases to the eventual fracture point. In the conventional PM technique, iron powder is deformed by compaction. Permanent and non-recoverable plastic deformation occurs within each particle where dislocations tend to accumulate. Measuring the microstructural amount of deformation is difficult due to the small scale involved, since it is not possible to offer a simplistic representation of a stress-strain curve of an iron particle (10).

Plastic deformation in crystalline materials occurs by slip. One part of the crystal slides across an adjacent part, in what it is called slip plane. These movements take place on specific crystallographic planes, an example of which is plane (123) for bcc metals, being the slip direction in the line of the closest atomic packing, [111]. According to Schmidt's law, slip takes place when the corresponding component of shear stress reaches the critical value. Deformation by slip is inhomogeneous: large shear displacements occur on a few widely separated planes, while parts of the crystal lying between slip planes remain essentially un-deformed. This boundary between slipped and un-slipped regions is called dislocation. Near the dislocation, the crystal is highly strained, since atoms at the slip plane experience repulsive forces from some neighbours and attractive forces from some others across the slip plane. There exist edge, screw and mixed dislocations. The density of dislocation stands for the number of dislocation lines that intersect a unit area in a crystal, where the best crystals are situated below 10^2 dislocations/cm^2 and heavily deformed materials range between 10^{11} and 10^{12} dislocations/cm^2 (12).

2.2.1 Strengthening and Annealing

The strengthening of alloys is strictly related to the dislocation movement, with the pursued objective to increase the yield strength so that the material will be able to withstand higher shear stresses and toughness. The four most important ways to make this happen are the mechanical blocking of dislocation motion, pinning of dislocation by solute atoms, impeding dislocation motion by short range order (reducing grain size), and increasing dislocation density. The objective is that the tangling of dislocations results in the enhancement of the mechanical strength and restriction of dislocation motion results in a harder and stronger material.

In the case of the strengthening of materials by grain size reduction, grain boundaries act as a barrier to dislocations. During plastic deformation, dislocation motion must take place across this common boundary. Considering that two grains are of different orientations, it becomes more difficult as the misorientation increases. Dislocations tend to pile up at grain boundaries, as they are unable to transverse the high angle boundaries; so a fine grained material will be stronger than a coarse grained one. There is a useful mathematical expression, relating grain size and yield strength called the Hall-Petch equation:

$$\sigma_y = \sigma_o + \kappa_y d^{-1/2} \qquad \text{(Eq. 2.2.1)}$$

where σ_o and κ_y are constants for a specific material, and d is the average grain diameter. This equation is only valid in the case of fine grained polycrystalline materials.

Strain hardening is another strengthening method where dislocations play a principal role. Ductile metals become harder and stronger as they are plastically deformed, that is because dislocation density grows due to *work hardening*. Dislocations are positioned closer together, so the stress necessary to deform a metal increases. This is really common to enhance properties of metals during fabrication procedures. After strengthening of metals, an annealing process is followed in order to soften some of the mechanical properties. The stored energy in the material, by dislocations and vacancies, is the driving force during annealing. There are usually three stages: recovery, recrystallization and grain growth:

- **Recovery**

There is an energy reduction related to the realignment of dislocations into sub-grain boundaries and the relief of some stresses, this results in a slight reduction in hardness. A number of point defects diffuse to edge dislocations and grain boundaries, but there are no major changes in the microstructure. The overall grain shape and orientation remain unchanged. The changes during recovery cannot be observable under a light microscope. (10)

- **Recrystallization**

The driving force for recrystallization is the reduction of energy as old grains with many dislocations are replaced by new grains with fewer dislocations. In this stage, new strain-free equiaxied grains are formed, consuming the old ones in a process that involve short range diffusion. This process is also known as *polygonization*. The recrystallization is affected by purity, more than by grain size. Solid solution impurities tend to segregate at grain boundaries, slowing their motion and increasing the recrystallization temperature. However, in this recrystallyzation stage, the nucleation rate is increased more than the growth rate, so with the sufficient amount of cold work the recrystallized grains remain smaller. Mechanical properties recover their pre-worked values; that is the material becomes weaker softer and more ductile. The extent of the whole process depends on time and temperature. The recrystallization behaviour of a metal alloy can be specified in terms of a recrystallization temperature, after a heat treatment of one hour. This is usually between one half and one third the melting temperature (10) (14).

- **Grain Growth**

In the grain growth stage of annealing, recrystallized grains grow at the expense of other recrystallized grains. The driving force for grain growth is the reduction of energy associated with grain boundaries, so they tend to move towards the centre of curvature in order to reduce their surface area. Large grains tend to be concave, and consequently they grow at the expense of their smaller neighbours (See Figure 2.2d). Even when the whole process is driven by temperature there is a limiting grain size that decreases when more particles are formed. The growth rate is also retarded by impurities in solid solution and second phase particles, but overall the average grain size is dependent on the time (12).

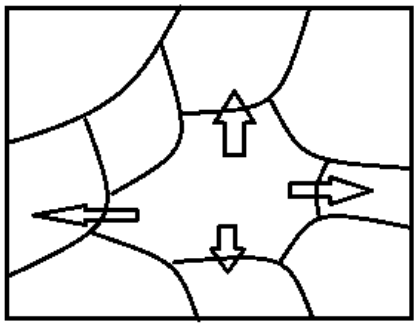

Figure 2.2.1 – Growth of large concave grains at expense of small shrinking ones (14)

2.2.2 Hardness

Another important mechanical property is hardness, which is the resistance of a material to localized plastic deformation, normally performed by an indenter. The depth and size of resulting indentation is measured, and then related to a hardness number; the softer the material the larger and deeper the indentation and vice-versa. Normal scales and tests are Rockwell and Vickers. Some other advances techniques such as nanoindentation are explained further in the experimental part, Chapter 4 of this thesis. Both tensile strength and hardness are indicators of metal's resistance to plastic deformation, consequently they are roughly proportional (10).

2.3 Magnetic Properties in metals

Magnetic behaviour in materials always relies on their atomistic magnetic nature. Based on the excess of electrons, occupancy of the bands and net magnetic moment, metals and their alloys can be classified according to their magnetic behaviour as diamagnetic, ferromagnetic, antiferromagnetic, ferrimagnetic or paramagnetic (10).

Ferromagnetic materials are of primary interest in engineering, since their spin atoms are aligned, the interaction of neighbour atoms is positive in a way that their magnetic moments add up (15). In other words, they have a permanent magnetic moment in the absence of an external field. This positive interaction is gradually decreased with increasing temperature. As shown in Figure 2.3a, approaching the Curie temperature the interaction falls toward zero. Iron becomes paramagnetic above 770°C, that is, essentially nonmagnetic. The ferromagnetic characteristics are displayed by the transition metals iron (BCC), cobalt, nickel and other rare earth metals (10).

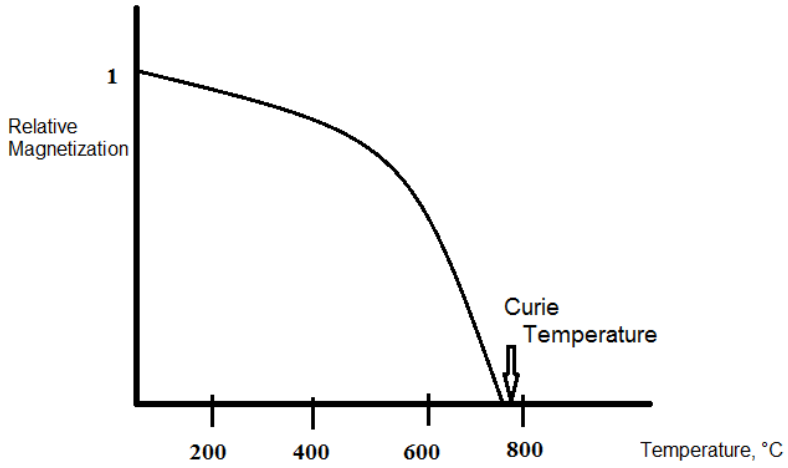

Figure 2.3a - Effect of Temperature on Magnetic behaviour of Iron (15)

A magnetic domain is a region in which the magnetic moments of the atoms are aligned and point in the same direction. A Bloch wall in a crystalline structure is the transition layer that separates adjacent domains magnetized in different directions. Domain structures of metals are complex, since they are based on the magnetic energy stored in a material. Systems drift from a saturated configuration, at a maximum magnetic induction, to a lower energy state based on the movements of its magnetic domains. In the presence of an external magnetic field, the walls between domains tend to move, at same time as the domain in the direction of the applied field grows within the internal structure, as shown in Figure 2.3b. The difference in magnetic behaviour is what defines a magnetic material as either *soft* or *hard*; where a soft magnetic material can be easily demagnetized after the magnetizing field is removed (12).

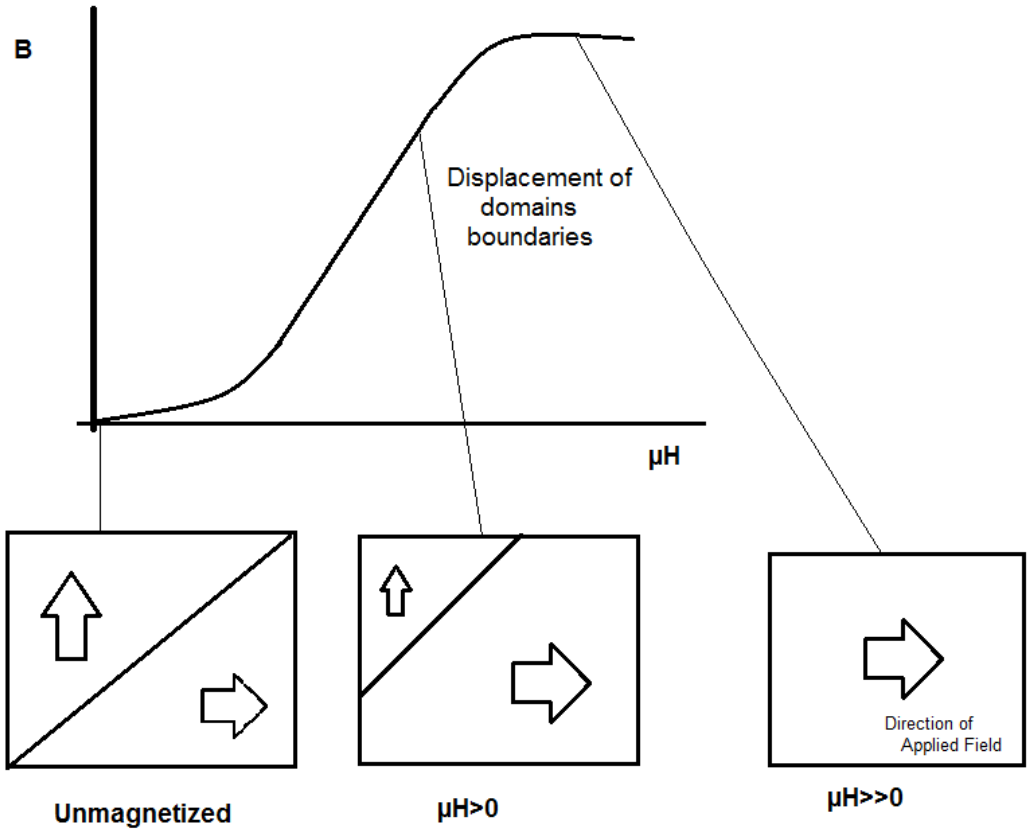

Figure 2.3b – Domain behaviour under an increasing external magnetic field. Adapted from (15)

Soft magnetic materials have easily moveable domains, only stopped by inclusions, grain boundaries or defects; in the case of PM produced materials pores are the most common defects. As can be seen in Figure 2.3c, the area of the hysteresis loop on a soft material is much smaller than in a hard magnetic material, since the first one is more easily magnetized in the presence of the same external field. In SMC materials (see section 2.4) sufficiently small particles are always magnetized to saturation as a single domain (12). Characteristics like this are highly appreciated in for instance high frequency applications. Hard magnetic materials, on the other hand, are what we can call permanent magnets. They are really difficult to demagnetize, having large hysteresis loop and coercive force, which makes them ideal for applications that require permanent magnets, for energy storage for instance (14).

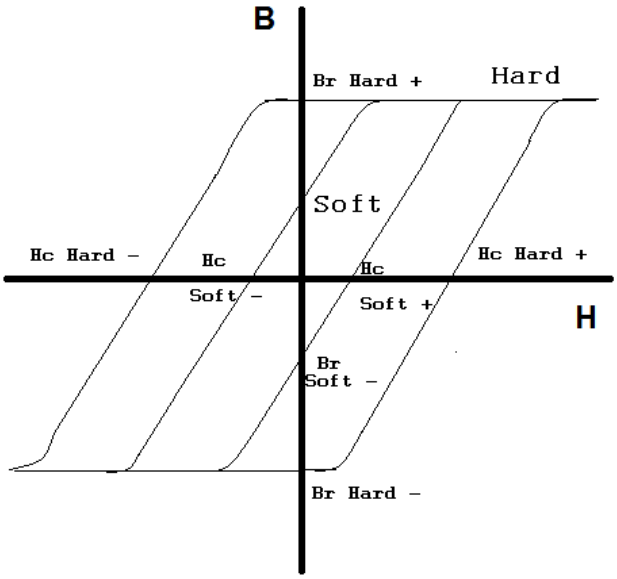

Figure 2.3c – Comparison between Soft and Hard Magnetic Materials (14)

The slope of the hysteresis loops in Figure 2.3c is the permeability (μ). This is a property of the specific medium, and it can be defined as μ=B/H, where B is the flux density within the material and H the magnetic field applied (10). The coercivity or coercive force (H_c) is the magnetic field required to reduce the magnetization or the induction (B) to zero. So in these terms, a low coercivity material is also called *soft magnet* and vice versa a high coercivity would be *hard magnet*. The coercivity is also affected by the impurity content and internal strain, which is annihilated by the annealing processes. Amorphous ferromagnetic alloys have low coercivity, low hysteresis losses and, on the other hand, high permeability (μ), due to the easy movements of their magnetic walls (12). The hysteresis effect is produced when B field lags behind the applied H field. At zero H there exists a residual B field called *remanence* (B_r), which is the intercept with the y-axis. This behaviour, bound to the coercivity concept, may be explained by the motion of domain walls. The relative area within the hysteresis loop gives an idea of the energy losses during magnetic induction of the material. Hysteresis curves depend on various factors, among others the preferential orientation of the grains in a polycrystalline material. Controlling the presence of pores and the stress state of the material would result in desired hysteresis parameters (10).

To sum up, soft magnetic materials should have domain walls which are able to move easily so that the area of the hysteresis loop becomes as small as possible. The shape of it would be also narrow due to low dislocation content, low residual stresses and low interstitial impurities. Inclusions and other defects are important obstacles to domain wall movement because the energy of the system is lowered. An air gap, for example creates a magnetic field in the opposite direction to the applied field, so the magnetic induction also lowers due to discontinuities (8). Soft magnetic materials applications include transformers, motor and generator cores. These applications employ silicon-iron alloys in the case of laminated steels and SMC, being ferritic at all temperatures. Silicon increases the electrical resistance of iron, which is desirable because power loss is inversely proportional to resistance (see Section 2.4.1). Energy losses may result from electrical currents that are induced by the magnetic field: *eddy currents*. Increasing electrical resistivity minimizes energy losses. Use of thin sheets also minimizes eddy current, and a similar effect occurs for powder based components (14).

2.3.1 Magnetic Anisotropy

Magnetic anisotropy is the dependence of magnetic behaviour on crystallographic orientation, as there is always a crystallographic direction in which magnetization is easier. This means that the magnetization saturation can be achieved at the lowest H field, and there is a higher area under the M-H curve associated with a higher slope (μ-permeability). In the case of Fe, the easy magnetization direction is [100], as can be seen in Figure 2.3.1a.

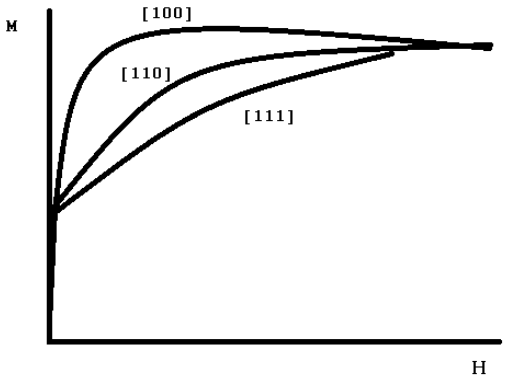

Figure 2.3.1a – Magnetization curves for single crystal iron (10)

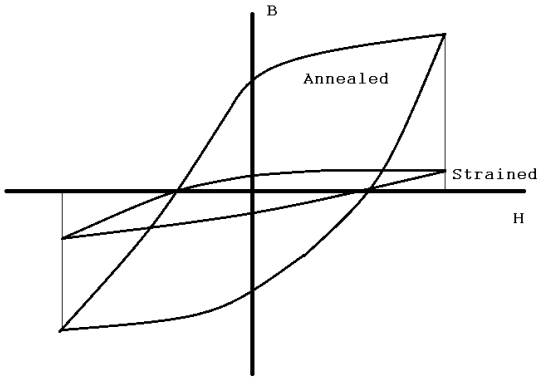

Figure 2.3.1b – Difference in magnetic behaviour between annealed and strained magnetic metals (16)

It is possible to control the crystallographic texture of an iron sheet, by controlling the rolling and heat-treating manufacturing processes. The [100] direction should be oriented parallel to the direction of the applied magnetic field, in a way that the easy direction of magnetization is aligned with the prior rolling direction. What is achieved by rolling is to orientate all crystals towards this easy magnetization direction. For body-centred cubic metals (BCC) such as iron, directions [100] and [001] are equivalent, that is, both directions are easily magnetized (14).

Energy losses in a transformer core, for example, could be minimized by taking advantage of anisotropic magnetic behaviour. Since the magnetization lies naturally along the [100] direction, cold rolling is able to introduce a marked texture or preferential orientation of the crystallites. This effect is also denominated *induced magnetic anisotropy*, and it can be also observed in powder based materials (13).

However the *domain rotation* could be affected by the plastic deformation introduced in the cold working process, and this actually it makes magnetization more difficult. In Figure 2.3.1b it can be appreciated that the larger coercivity value, and thus bigger area in the hysteresis loop for the same applied field, on strained and another annealed materials. These changes are caused by the increased number of dislocations and other micro-stresses, which impedes the motion of domain walls. A cold-worked material can be restored to a condition of maximum magnetic softness only by annealing above the recrystallization temperature of the material, which in the case of iron it is above 600°C (16).

2.4 Soft Magnetic Composites (SMC)

Soft Magnetic Composites (SMC) are powder based materials developed for electric applications at high frequency ranges. They are based on high purity powder particles, normally water atomised, of pure iron or iron alloys with a minimum content of Silicon or other additives. The basic structure includes an insulation layer of an organic or inorganic coating on the surface, see Figure 2.4a.

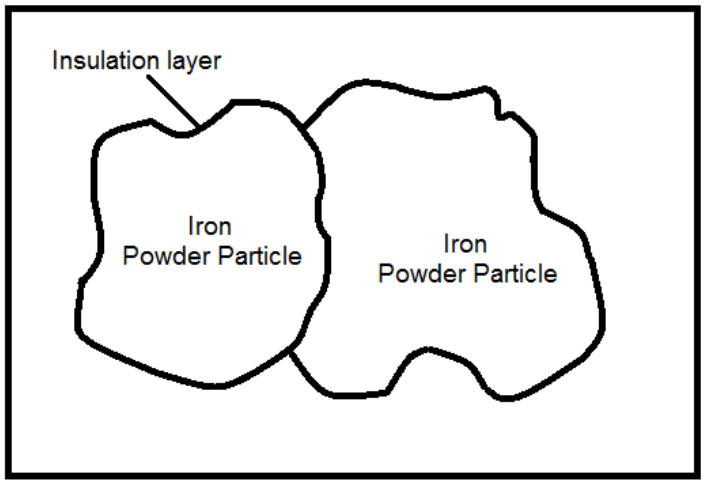

Figure 2.4a – Structure of SMC powder, adapted from (3)

SMC components opened up possibilities for 3D complex design solutions for electrical applications, which traditionally employed laminated steel sheets. Rotor and stator cores for instance use steel sheets stacked on top of each other resulting in good magnetic properties in the plane of the laminates, but at the same time poor magnetic properties in the normal direction. (See Figure 2.4b) Isotropic properties of powder based materials, and their unique shaping possibilities, makes SMC perfect for high frequency applications. The magnetic flux can move equally well in all three dimensions of space, and this gives a higher degree of freedom to place the material where is most needed. Another advantage of PM is the possibility to manufacture with close tolerances, important to avoid machining and air gaps, which could increase the reluctance of the magnetic circuit. In addition, the processing steps of PM i.e. mixing, compacting, dewaxing etcetera result in good quality cost-effective components (3).

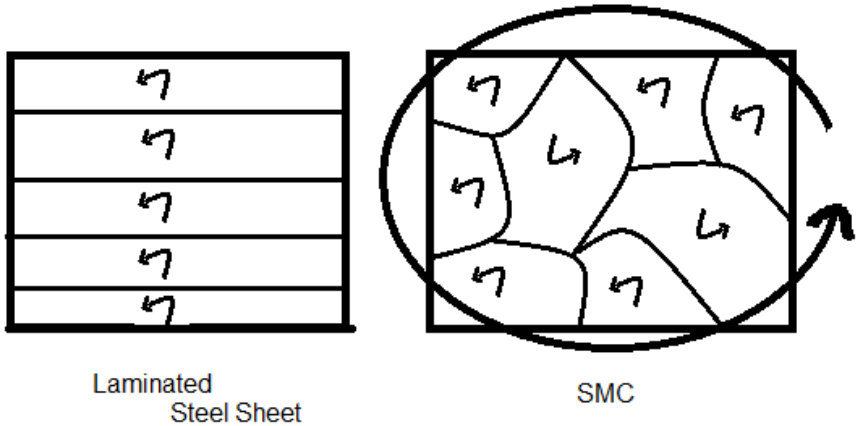

Figure 2.4b – Eddy Current behaviour in laminated steel and in SMC material (17)

Magnetic powder based materials do not follow a sintering process, as this can affect the nature of the insulating coating around particles. The insulation layer must be as thin as possible, while keeping good insulation properties, and at the same time it must also withstand the friction between particles caused during compaction (18). Ideally the powder should maintain its compressibility properties even after the implementation of the coating. Furthermore, the mechanical strength in SMC materials is lower than laminates or sintered components, though their magnetic properties should be competitive or even superior. The strength of the SMC components is much based on the particle surface morphology and the use of binder additives. The use of lubricants such as Kenolube^{TM} in the surface of SMC powder has been recently studied by Christos Oikonomou in his Licentiate Thesis (19), in addition to the mechanical strength obtained from the oxide scale layer formed in the exterior regions of the components, which also acts as a "binder".

Due to the processing route, a final compromise between the optimal magnetic properties, aiming for a higher density, and the stress within the particles has to be accomplished. A heat treatment after compaction is in charge of the stress relief of the particles. The limit in temperature is established by the binder and the insulation layer around particles. Even when the choice among different lubricants can differ in more than 200°C the upper limit in temperature during the heat treatment, the magnetic induction suffer less comparative difference (20).

From the magnetic point of view, high induction is always desirable, so a component with high density and thus processed under higher pressures, would be ideal. Unfortunately, density levels desired for mass production are often a compromise between the material performance and the production cost, which tend to increase with compaction pressure and complexity of the component. When the component is compacted, plastic deformation of the powder particles occurs, obstructing magnetization process, i.e.: increased hysteresis loss, decreased permeability and lower induction. The influences of internal stresses create particles behaving as permanent magnets, increasing the area of the hysteresis loop of the material. That is why the subsequent heat treatment is so important. When applied to a compacted component, it is not only an improvement of the magnetic properties what it is desired, but also a relief mechanical stresses and increase mechanical strength (17).

2.4.1 Iron core losses

The magnetic losses in ferromagnetic materials arise because of the change in magnetic induction, generating voltages in closed paths in the material. The voltages generate eddy currents in the material, and thus resistive Joule heating. The classical Eddy-current loss calculation derives from Maxwell's equations, for which the general form is (21):

$$P=kf^2d^2B_m^2/\rho \qquad \text{(Eq. 2.4.1)}$$

where P is the power loss per mass unit (normally expressed in W/kg), f is the frequency (Hz), d is the thickness considered of the material (m), B_m is the maximum induction level (T) and ρ is the electrical resistivity (Ωm); k is a geometrical factor

In an electric machine, the I^2R are the losses in the windings that can be reduced with an effective design. The core losses, also called losses in the soft magnetic materials, are traditionally divided in hysteresis losses (DC) and dynamic losses (AC). Last one is generated in alternating magnetic fields, giving birth to eddy currents. On the other hand, hysteresis losses are more related to the change in magnetic state of the iron.

In a pure DC use of the material, only hysteresis losses would be present, since they are related to the microstructure and not to the coating of SMC. They also show a linear dependency with frequency, while the dynamic losses show a square dependency. At some

frequency there is a cross over point, where SMC take advantage of laminates materials, whose hysteresis losses are much lower. This cross over point depends on the powder mix and the manufacturing parameters.

Resistivity is the main factor to keep eddy currents low, and it can be controlled by alloying elements and the manufacturing processes. The type and concentration of alloying elements, density and crystal structure have influence on the resistivity. Good insulation and fine particles are generally required to minimize eddy currents, especially in high frequency applications. The absence of diffusion-bonded particles (sintered powder based materials) reduce the eddy currents near zero, so SMC are considered for frequency applications between 50 and 10^6 Hz, covering a wide spectrum of high frequencies (18).

The magnetic saturation depends on the alloy, purity and density, as well as the microstructure. The saturation level of a high density SMC component is comparable to laminates. However, most electric machines operate below saturation and due to the lower permeability, the magnetic induction will be also lower. SMC materials are not sintered, since the dynamic losses would increase rapidly with frequency if the insulating coating is compromised. In an SMC component, the magnetic flux has to pass through non-magnetic barriers such as the interparticulate insulation coating and pores, which make that the maximum relative permeability significantly, lower in SMC-materials than in plane-laminates (3).

In conclusion, the ideal SMC is isotropic with high initial magnetic permeability, low coercivity and high saturation induction. It can be easily 3D shaped thanks to PM technology in order to take complete advantage of its isotropic nature. The plastic deformation after compaction steps results in internal stresses in the particles, and consequently in higher hysteresis losses. A heat treatment after compaction partly relieves the stresses, changing the hysteresis loop, (see Figure 2.3a). The induced stresses in the material during compaction are responsible for the increase in the hysteresis losses. The saturation induction is close to laminates, while eddy currents are significantly lower, due to the small size of powder particles compare to steel sheets in laminates (1).

2.5 Texture

Texture can be defined as the crystallographic orientation of polycrystalline materials, in other words, when atomic planes in a volume of a crystal are positioned relative to a fixed reference. Grain orientations in polycrystalline materials can be fabricated during the manufacturing process. This usually occurs in two ways: either during crystallization directly from melt to solid state, where certain orientations are induced to follow a determined pattern; or during subsequent thermo-mechanical processes once the material has already crystallized. This tendency known as *preferred orientation* or *texture* can influence material properties to a high extent, both mechanical and electric/magnetic. This effect is exploited in material technology to produce materials with specific characteristics or behaviours, as has been already explained in the case of magnetic anisotropy (Section 2.3.1). One of the few examples where grains are oriented randomly is in a polycrystalline aggregate made by compaction of powder. Texture can change after processes such as in deformation or recrystallization, which probes texture analysis as a valid diagnostic tool to investigate the history of the material (22).

2.5.1 Representation of Orientation

The most established method for measuring texture is X-ray diffraction using a texture goniometer. However, depending on the technique used, the representation of the orientation would be different. Other techniques such as optical microscopy, Scanning Electron Microscopy (SEM), and Transmission Electron Microscopy (TEM) also give information of both microstructure and crystallography. The traditional approach has been to make parallel but separate investigations based on several techniques (22).

Electron Backscattered Diffraction (EBSD) technique, also known as backscatter Kikuchi diffraction, is nowadays the backbone of most texture research. This technique has the ability to obtain microstructure-level information with a special resolution of the nanometre range, this will be further explained in section 4.1. The structures of crystals are often represented by the *pole figure* of its crystallographic plane. A plane is chosen as the equator of a sphere used for the stereographic projection of the Miller indices, as poles. A pole figure will plot that direction (pole) for each and every crystal relative to a set of directions in the material. When poles are randomly distributed in an equal area pole figure, the material is considered to have a random texture, as can be seen in Figure 2.5.1a. An inverse pole figure is another stereographic projection whose vertices are the crystal direction instead of sample directions, as can be seen in Figure 2.5.1b (23) (24).

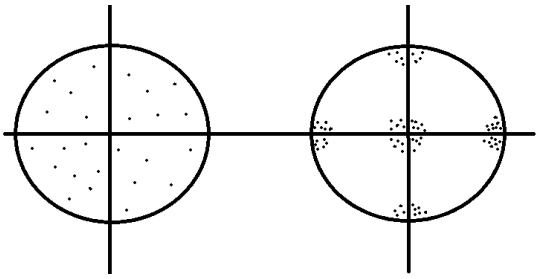

Figure 2.5.1a – {100} Pole figures showing random texture and cube texture (left and right respectively) (23)

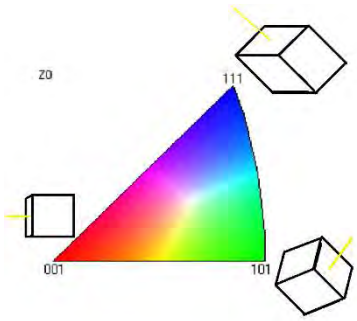

Figure 2.5.1b. – Inverse Pole Figure - based on (24)

3. Materials

In this thesis the SMC powder provided by Höganäs AB (Höganäs, Skåne - Sweden) was analysed. It consists of water atomised iron powder, coated with an ultrafine electrically insulating layer. Depending on the lubricant used to prepare the samples, several mixes are possible, being the one studied including 0,5 wt% Kenolube^{TM}.

The powder was examined both in as received state and as a finished SMC component of toroidal shape, 5x5 mm cross section, an outer diameter of 55mm and an internal diameter of 45mm as the one illustrated in Figures 3a and 3b below.

Figure 3a – Standard SMC ring

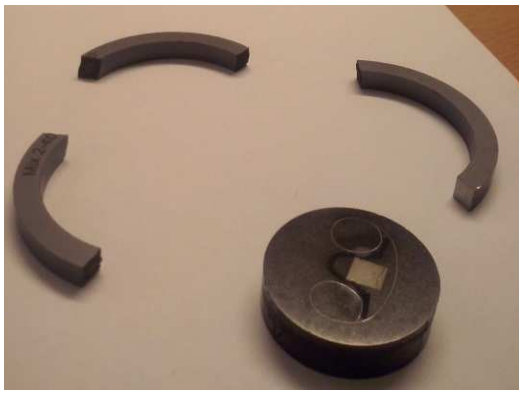

Figure 3b – Cut ring and view of the cross section

For the purpose of this project work, only the mentioned mix was examined, since SMC components having Kenolube^{TM} as lubricant exhibited optimum performance (25). In the appendix A are shown the results of the analysis of ABC100.30 powder, also produced in Höganäs AB, which was used as a reference and compared to the SMC powder.

The production of the SMC parts included the compaction by uniaxial pressing at 400MPa, 800MPa, and 1100MPa and heat treatment at 400ºC, 500ºC, 550ºC, 600ºC and 650ºC in air.

3.1. Sample preparation

For the nanoindentation and the electronic microscopy analysis, the cross sections of the rings were considered. The samples were cut in sections of 10mm height approximately, then hot mounded to conductive resin Polyfast (Struers), and the external surface polished by conventional metallurgical procedures. The cross section shown in Figure 3b is approximately 5x5 mm, being the height of the specimen the 10 mm mentioned before. Specimens for microstructural characterization were polished to a mirror-like surface using standard metallographic techniques. All test samples were polished down to 1µm using diamond suspension, followed by fine abrasive polishing step with silica suspension OPU (Struers), as it is advisable for soft and ductile materials (26).

4. Experimental Techniques and Methodology

4.1 EBSD analysis

Electron Backscattered Diffraction (EBSD) technique is embedded and conducted in the Scanning Electron Microscopy (SEM). Specimens are tilted 70° in vacuum conditions in the SEM chamber (see Figure 4.1 below). Electrons diffracted are detected by a phosphor screen, where the formed Kikuchi patterns are processed through mathematical transformations. In this way, the information about the microstructure can be overlapped to the secondary imaging of the grains which is collected by a Secondary Electron (SE) and Force Scattered Detector (FSD) in the SEM (24).

SEM is set on spot mode and back scattered electrons are collected and able to solve for wide angle Kikuchi Patterns. Information from the surface (50-150nm) is revealed from a crystallographic point of view, e.g. local texture, grain size and morphology, recrystallized fraction and strain state among others. The most interesting piece of information is the local misorientation of the grains inside the iron particles (see Section 4.1.1) (27).

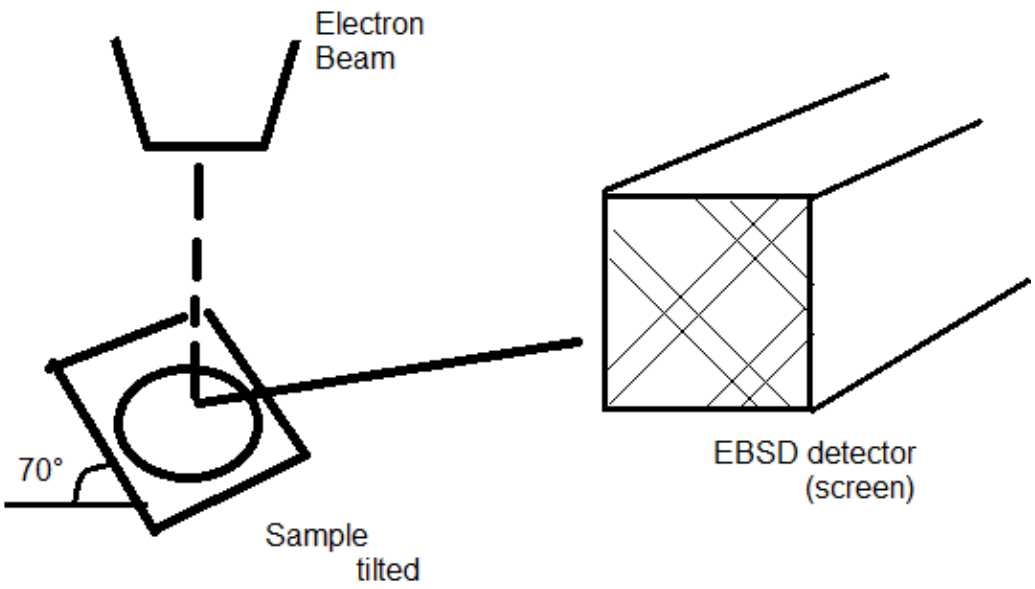

Figure 4.1a - Setting up of the EBSD detector

All single particle maps were performed with a step size of 0.5µm between pixels, considering the smallest grains observed were 1µm diameter following the *circle equivalent diameter method*. Magnification was set between 750x and 1,5kx in all cases. For the big maps, the step size selected was 1 µm, plotting always two maps, one on the edge and other in the centre of the cross section. Grains smaller than twice the step size were discarded, in this case below 2 µm. The Working Distance (WD) was between 15 and 20mm for all the maps, while the acceleration voltage on the electron beam was set at 20kV. For all cases an identical area of 700x500µm (350000µm^2) at 300x magnification was mapped for all conditions.

4.1.1 EBSD maps

EBSD maps convey visually the basic character of the material microstructure based on the phase and orientation of each pixel. The software can generate an enormous variety of visual and analytical information; in other words, maps comprised of schemes used to colour map pixels or boundary between pixels. As a background for other components, a scalar value is measured for each diffraction pattern. This map is known as the Band Contrast (BC) and gives an idea of the pattern quality, being affected by deformation or any crystallographic defects, but independent of the index result. Grain boundaries are visible as low pattern quality (dark lines), as well as other defects (like scratches during sample preparation), giving a SEM-micrograph type image as a result (24).

Other results based on crystallographic information (24) (28) and plot over the Band Contrast are:

- **Boundary Distribution Maps**: It shows deformed regions with a high density of *Low Angle Boundaries (LAB)*, where the misorientation considered between metal crystallites of 2° to 15º is considered. *High Angle Boundaries (HAB)* are considered when the misorientation is bigger.

- **Recrystallization Factor**: The system calculates an average value of misorientation, considering all grains and regions. Grains with an internal value below this average are considered recrystallized. (blue) Deformed grains, misorientation above mean value, are marked red on the maps, and grains having partially deformed regions will be shown in yellow as a substructured region.

- **Local Misorientation Maps**: Average misorientation between each measurement and its 8 neighbour pixels, excluding high angle boundaries above 5º has been investigated in all cases in the current work. As a colour scheme for particles a rainbow pattern is used, as can be seen in Figure 4.1.1b.

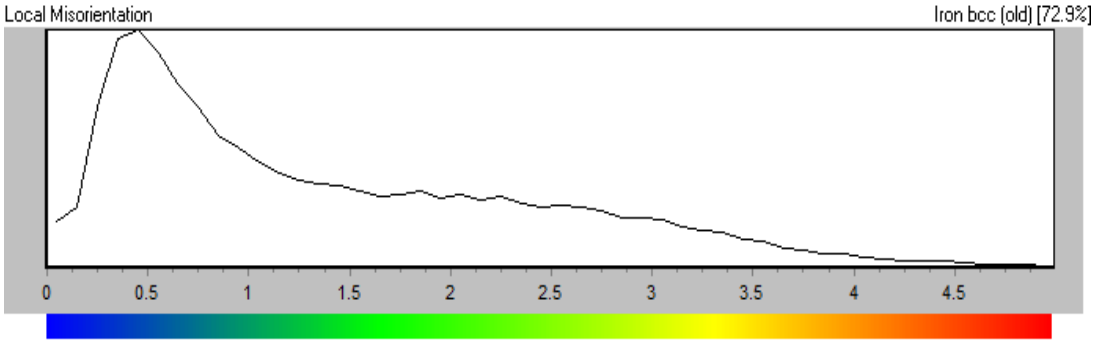

Figures 4.1.1 – Example of a Rainbow Colour Scheme for a Local Misorientation Map

- **Texture Components**: A colour scheme, relative to a specific orientation of interest, is used. These components visually and quantitatively allow understanding of the conformity between orientation in the sample and the orientation of interest. Inverse Pole Figure (IPF) colouring components as the one shown in section 2.5 are used.

4.1.2 Assessing deformation using EBSD

As explained in previous section, there are several measurements within the EBSD technique that reflect plastic strain on polycrystals. However, most part of these measurements are correlations. The technique asses changes in polycrystals that are the result of plastic deformation, not the percentage of deformation or plasticity itself. EBSD is sensitive to collective effects of dislocations, accumulated in the lattice during deformation. Normally, these can be divided in geometrically necessary dislocations and statiscally stored dislocations, the first one being referred to lattice rotation and the second ones associated to lattice imperfections (27).

Another observations in individual EBSD patterns differenciate between elastic and plastic strain. Elastic strain distort the lattice, changing the width of the diffraction bands (in case of uniform distortion). In case of a *bending* of the crystall, the pattern would also degrade, blurring the edges of the diffraction band. Plastic strain on the other hand, include the distortion in the lattice produce by dislocations (29)

4.2 Nanoindentation measurements

Hardness test is one of the most commonly used techniques to measure the mechanical properties of materials. It is performed when a prescribed load is applied to an indenter in contact with the material being measured. The load divided by the area of the residual impression is called the hardness. On the submicron scale, advances in nanoindentation allow to measure the depth of penetration as the load is applied (30). With this high resolution load-displacement data discrete events can be explained, such as recrystallization or phase identification (31) (32). The two mechanical properties measured most frequently are the modulus, E and the hardness H (33).

The components in a nanoindentation experiment are the test material, the sensors and actuators (transducer), and the indenter tip (34). The three-sided Berkovich indenter is the most common one, conventionally made of diamond, formed into 65.27 – 65.3°. It gives the same projected area to depth ratio as the more commonly used Vickers indenter, facing 68°, used in micro-hardness testing. The reason why Berkovich indenters are increasingly used in nanoindentation instead of the more familiar Vickers tip, is due to its higher accuracy and to the fact that a sharper tip is possible (35). Also, the experiments by Samuels and Mulhearn (36) showed some problems with indenters sharper than 60-70°, which not follow the *Slip-Line Theory*. This was proposed for frictionless contact of rigid plastic solids by Hill, Lee and Tupper in 1947 (37), where an upward flow around the indenter is produced by critical shear stresses, as can be seen in Figure 4.2a.

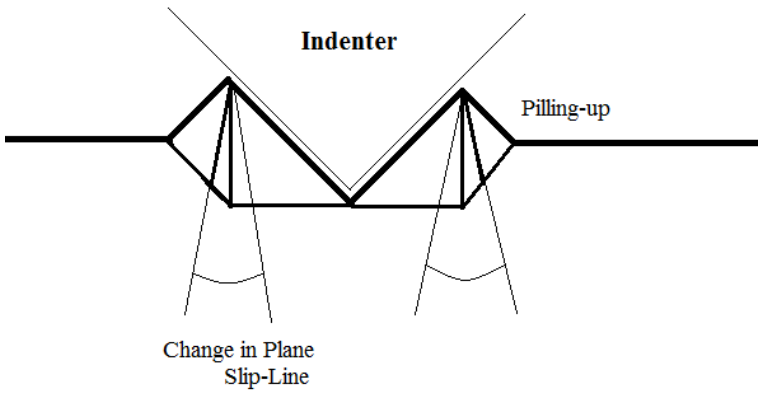

Figure 4.2a. - Pilling up effect around Indentation Impression – Adapted from (38)

Prior to the actual test, in one area not affected by the measurement, a *depth-sensing indentation testing* is performed in order to reference the specimen surface (30). A contact between the specimen and the indenter with a very small initial force applied is performed. During a nanoindentation test, force and displacement are recorded as the indenter is compacted into the test surface of the material, with a prescribed loading and unloading profile. This way a load-displacement curve is obtained, often called the P-h curve. The global shape of the curves differs from one material to the next, and these variations reflect different mechanical properties. In the case of metallic materials, the curve shapes as a tooth, as can be seen in Figure 4.2b. Also, in case of discrete physical events happening beneath the tip, this would reflect in the contour (30).

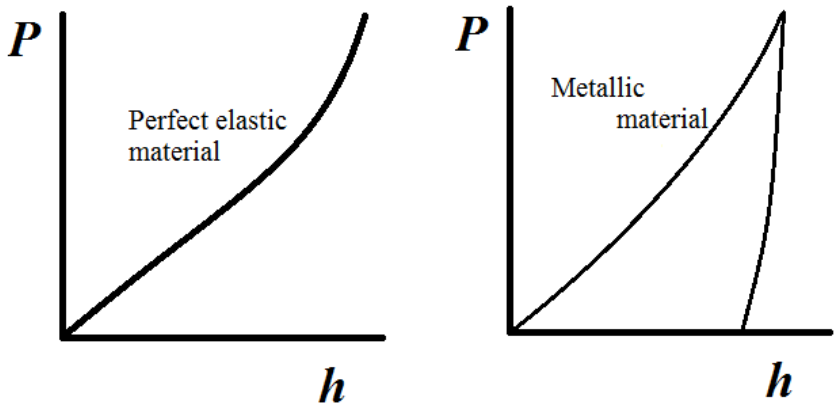

Figure 4.2b - Typical load-displacement curve, comparing metallic and perfect elastic materials (30)

Oliver and Pharr in their 1992 publication (39), assessed a procedure to determine the depth that should be used to establish the contact area at peak load, and consequently the hardness of the material. As can be seen in Figure 4.2c, there are some pilling up around the edges of the indentation due to the incompressibility of plastic deformation (40), this means that the hardness measurement may be incorrect if it is based on optical techniques to calculate the area. The Oliver and Pharr method guarantees a physical justifiable procedure for determining these values based on the first stages of the unloading curves, where the slope of the P-h curve can be considered linear. However, when measuring residual stresses, the elastic modulus, which is an intrinsic property of the material, should not be affected. The hardness and elastic modulus should be significantly independent of the residual stresses (41).

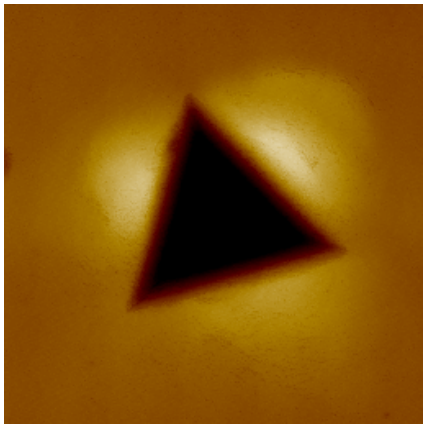

Figure 4.2c - AFM image of an Indent performed in an SMC particle annealed at 400ºC

Nanoindentation can also be considered a form of non-destructive testing, since the dimensions of the tip are very much smaller than the sample tested. The defects produced are negligible on the surface of the material, as the impressions are always at least one order of magnitude smaller than the grain size of the specimen material. In Figure 4.2d the effect of the pressure of

the tip to generate a plastic zone is shown. The stress induced on the material is 0.1-0.2 the pressure of the tip (42). The possibility of getting mechanical properties without damaging the structure of the material, and being able to focus on specific areas to measure residual stresses, makes this technique very promising in the future.

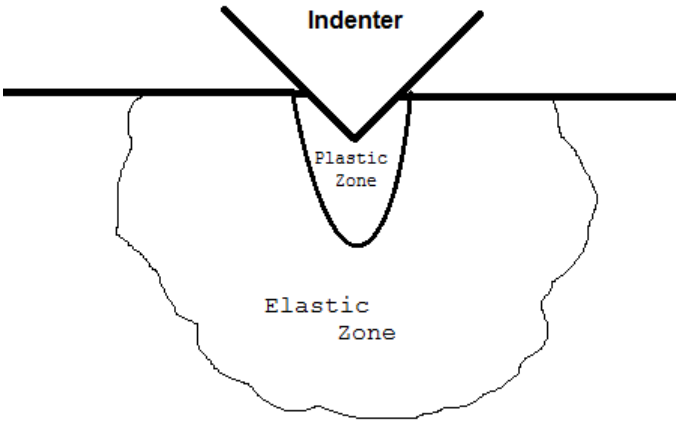

Figure 4.2d - Plastic and elastic induced zones in the material (38)

The nano-hardness maps were obtained using a Triboindenter TI 950 (Hysitron Inc., Minneapolis, MN, USA) in displacement control testing mode, at an imposed maximum depth of 200 nm using a Berkovich type diamond indenter. Loading, holding and unloading times of 10, 5 and 5 s, respectively were used, which resulted in maximum applied forces in the range of 2 - 3 mN. For each sample an array of 10x10 indentations was performed with spacing between indents of 5 µm in both vertical and horizontal directions. Thus, the dimensions of the area that was studied via nanoindentation were inside an iron powder particle. The nanohardness and Young's modulus values were determined from the analysis load-displacement curves using the method developed by Oliver and Pahrr (39).

Nanohardness maps were generated to analyse the nanohardness distribution inside the powder particles in order to differentiate stress free areas observed on the EBSD results. As shown in Figure 4.2c, Atomic Force Microscopy (AFM) topography scans were performed in contact mode on selected residual imprints using a Park XE150 instrument (Park Systems Corp., Suwon, South Korea), in order to check the applicability of the Oliver and Pharr method.

4.3 Magnetic testing

Three types of magnetic tests were performed per ring: resistivity, AC and DC measurements. While the first one was performed on the ring itself, on a four-point-measurement set, both AC and DC tests were performed in a Brockhaus Measurement equipment (43). In the last two cases, magnetic testing of the rings implies coiling them two successive times. The first coiling, the inner one, drives the magnetic flux within the ring while the second or outer one gets the output signal, where the losses and the induction in the material are obtained. Both include 100 turns around the ring, performed automatically by a Struers coiling equipment, getting an even separation between wires around the samples. The result is shown in Figure 4.3a, where the wires of the same polarity are marked with a loop and the inner and outer coiling are separated by tape.

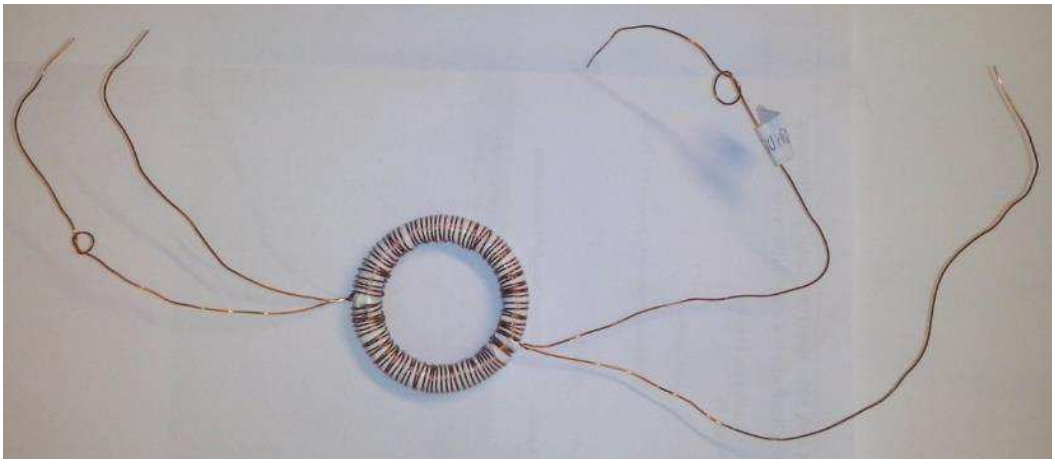

Figure 4.3 - Ring coiled for magnetic test

Measuring the dimensions is compulsory before AC/DC magnetic test, as well as the measurement of density or mass of the sample. The software MPG2 Brockhaus Measurements ID was used to calculate the hysteresis and dynamic losses per unit of mass, in addition to the permeability, coercivity and other characteristics.

Resistivity tests were performed in a simple four-point measurement set implemented with a current source and a voltmeter. The input to calculate the resistivity of each sample consists of the values extracted from measuring the voltage between four different couple of points distanced a constant value of 2cm, as well as the cross section of the standard ring considered, 0.25 cm^2 in our case. The operation and the units used are summarized in the next equation:

$$\rho = \frac{Average(V1, V2, V3, V4) \cdot 2 \cdot A}{I \cdot l} \qquad \text{(Eq. 4.3)}$$

where the resistivity is expressed in Ohms*m, the Voltages 1 to 4 expressed in mV, A is the cross section area of the rings in this case expressed in cm^2, I is the intensity in mA, and l is the length between the points, in cm.

All tests were performed keeping a fixed voltage of 30V and a current of 100mA in the current source. So in this equation, A, I and l are always kept constant.

For the DC test, a first field of 10000 A/m is induced in order to get to the saturation level. Then a complete hysteresis loop is completed. In the AC tests performed, three different maximum induction values were allowed per ring successively: 0,5T, 1T and 1,5T, with values of frequency increasing by 100Hz till the maximum of 1000Hz was achieved. The starting point was always 50Hz.

4.4 Mechanical testing - TRS

Tensile Rupture Strength (TRS) is a simple mechanical test performed on bars with a cross section of approximately 10x6 mm of the material studied. Specimens are hold by two points in the lower part, while a punch is lowered applying a force in the central part of the specimen, as can be seen in Figure 4.4.1a. The force applied will increase until the sample collapses due to the coalescence of cleavages in the central part.

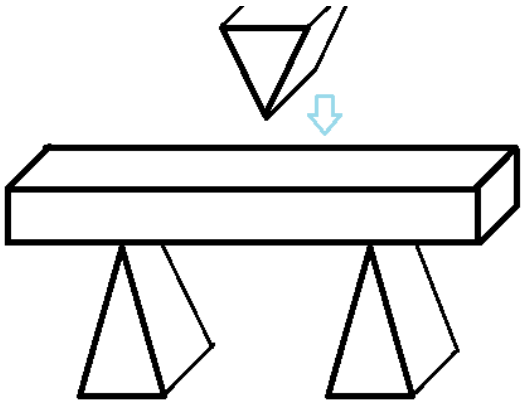

Figure 4.4 – TRS set up

The strength necessary to break the sample is calculated through the dimensions of the bar and the force applied by means of:

$$TRS = \frac{3 \cdot F \cdot L}{2 \cdot t^2 \cdot w}$$

(Eq. 4.4)

Where TRS value is expressed in pressure units considering the force applied (F) and the cross section of the bars (t*w), and the distance between the support points is kept constant (L = 25 mm).

5. Results

5.1 Analysis of SMC Particles in Components compacted at 800MPa

In this section, a qualitative analysis of particles of SMC components have been performed using the technique described in section 4.1, EBSD. The following results refer only to 800MPa series, which will be relate to nanoindentation further in section 5.2. The results for particles in components compacted at 400MPa and 1100MPa are presented in Appendix C.

5.1.1 Low Angle Boundaries (LAB) and High Angle Boundaries (HAB) maps

These maps show the misorientation between indexed points, where 2° to 15º are the Low Angle Boundaries (LAB) and above 15º High Angle Boundaries (HAB). As a background for the following maps the Band Contrast (BC) has been used. Areas surrounding grain boundaries and peripheral areas, where the particle to particle contact is taking place, are usually blurry since the EBSD technique did not successfully index points in strained zones, see section 4.1.1. The next couple of particles show on the left both LAB and HAB over the BC, see Figure 5.1.1 So in the left the small misorientations can be visualised as thin black lines, while on the right the grains constituting the particle can be visualised in within the thicker black lines.

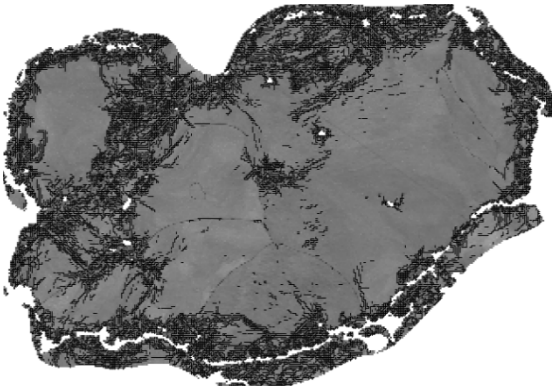

a) Green - LAB

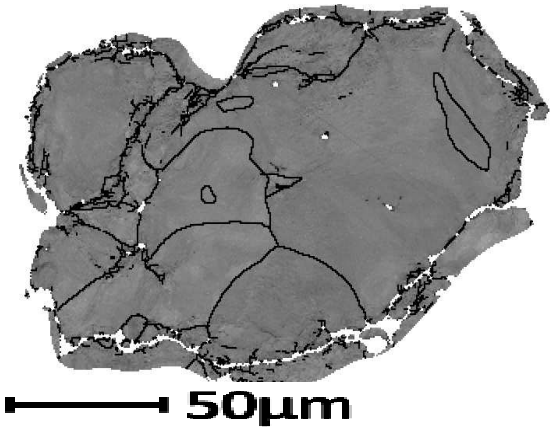

b) Green - HAB

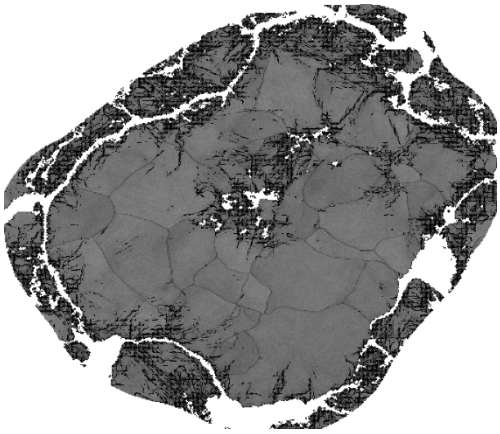

c) 400ºC - LAB

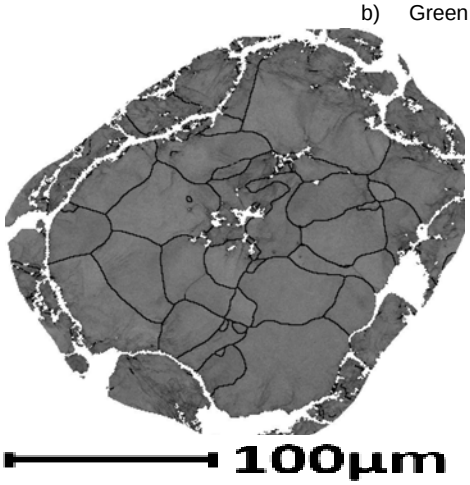

d) 400ºC - HAB

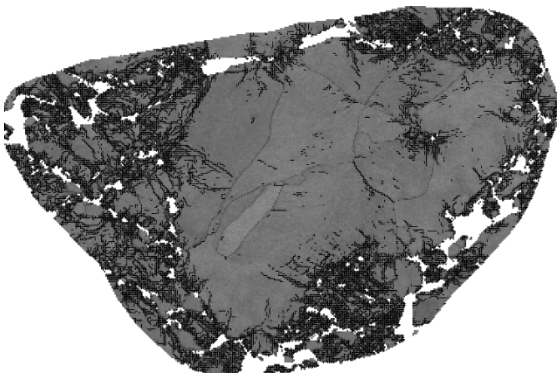

e) 500ºC - LAB

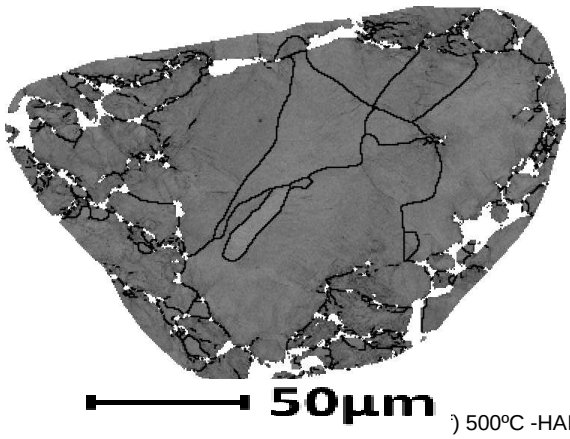

) 500ºC -HAB

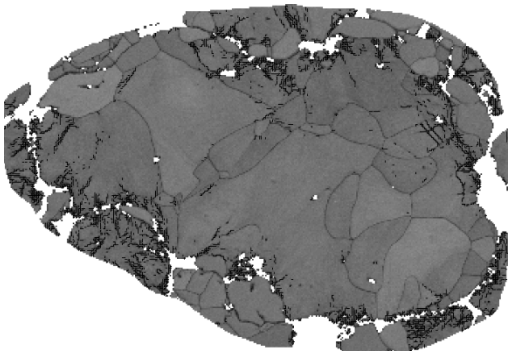

g) 550ºC - LAB

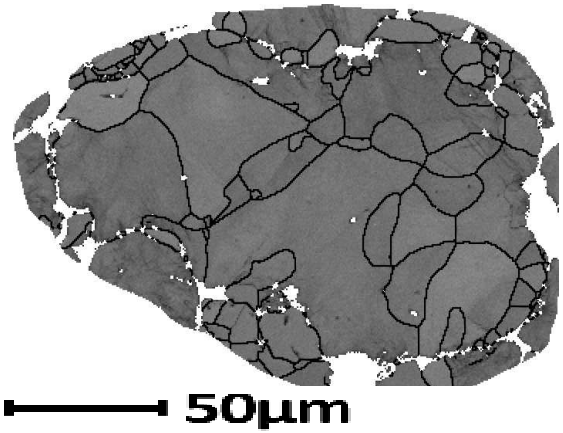

h) 550ºC - HAB

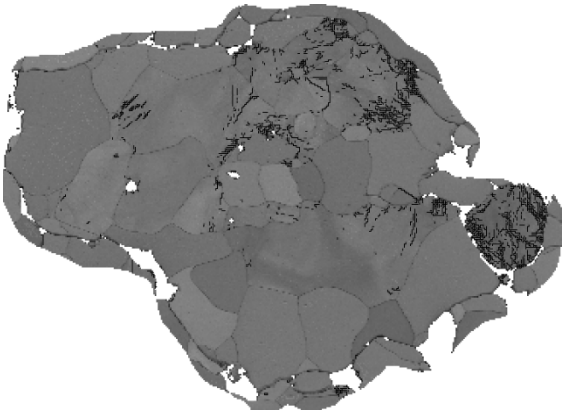

i) 600ºC - LAB

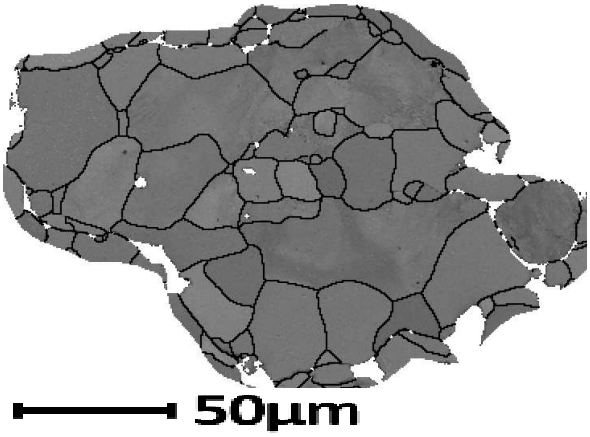

j) 600ºC - HAB

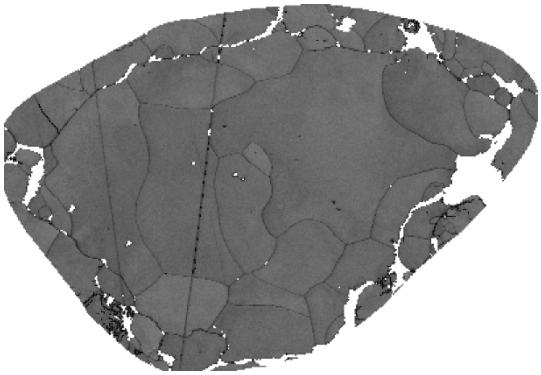

k) 650ºC - LAB

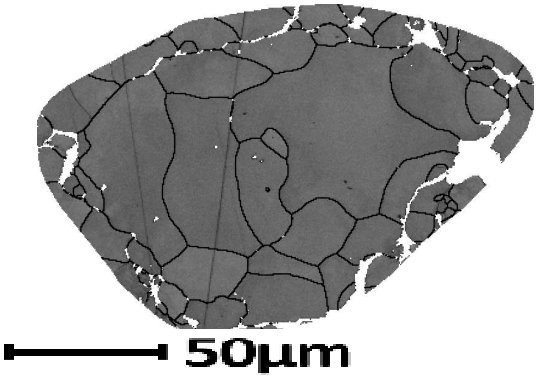

l) 650ºC - HAB

Figure 5.1.1 – LAB and HAB representation of single particles for: (a,b) Green Parts, (c,d) 400ºC, (e,f) 500ºC, (g,h) 550ºC, (i,j) 600ºC, (k,l) 650ºC

As can be observed for the last two conditions, at 600ºC and 650ºC, the LAB and HAB maps differ. That means that the small misorientations (LAB) are disappearing, as described in section 2.2, and the annealing process is affecting the microstructure generating new grains in the edges of the particles, free of strain concentration. This description of the microstructure will continue on the following sections.

5.1.2 Recrystallization Factor

Regions and grains are divided in recrystallized, substructured or deformed, as blue, yellow and red respectively, as explained in section 4.1.1.,. LAB are also included for the better understanding of the recrystallization phenomenon.

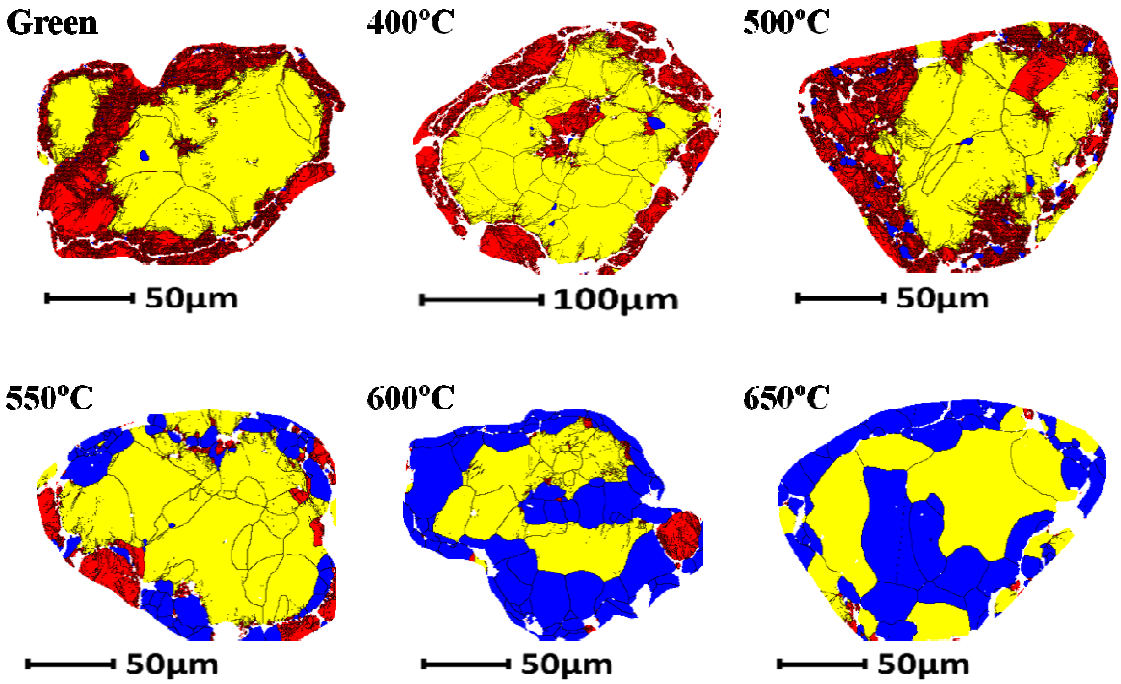

Figure 5.1.2 – Recrystallization factor of single particles

The amount of recrystallized areas in the last two particles studied is significantly larger than in medium temperatures. At 500ºC the recrystallized areas are big enough to be visualized, blue small regions in Figure 5.1.2 are located on the edges of the particle, embedded in deformed areas denoted by colour red and a higher concentration of LAB. Nanoindentation measurements in section 5.2 will clarify these aspects of the microstructure.

5.1.2 Local Misorientation Factor

As explained in section 4.1.1, an average orientation per pixel is set comparing it to 8 of its neighbours. Grain size and angle boundaries are not taken into account, even though HAB and LAB are still included in the images for a better understanding of the strain state of the particles.

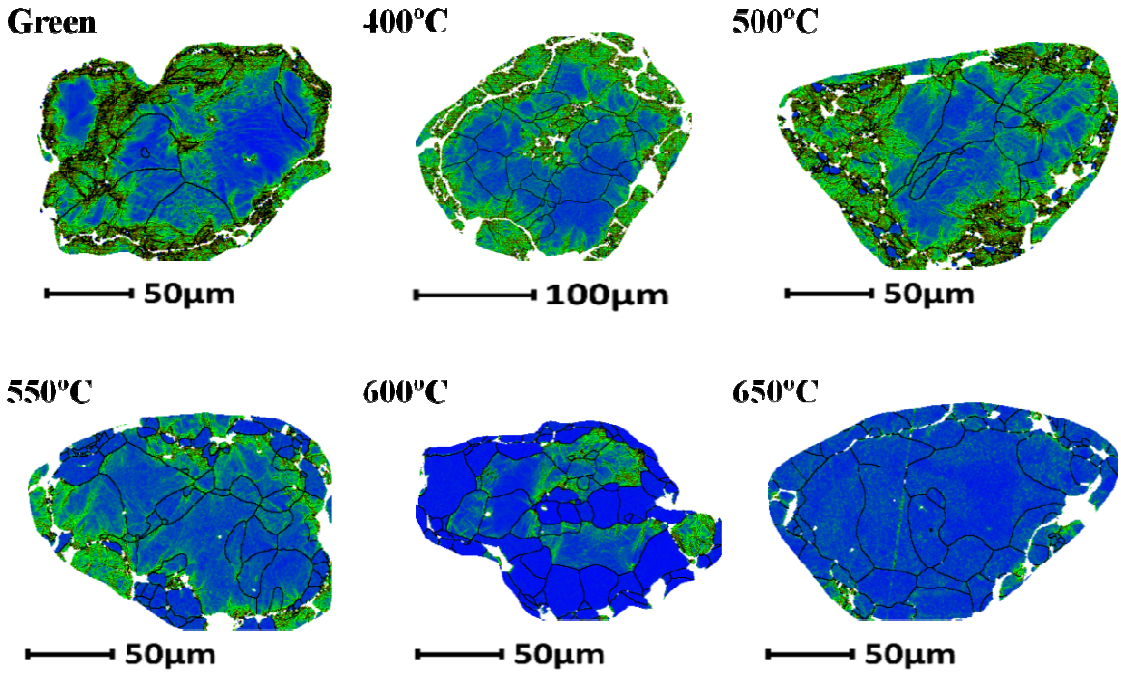

Figure 5.1.3 – Local Misorientation Factor of Single Particles

A rainbow colour scheme is used on these maps, and as observed in the low angle boundaries and in the recrystallization maps, the misorientation turn from 3 (yellow colour) to 0 (blue colour) over the temperature range. This means that at 600ºC there are almost no local neighbour points misoriented for bigger areas of the particles. When compared to the previous recrystallization results, new recrystallized grains have blue colour.

5.1.3 IPF maps

Considering three axis, IPF maps are represented along with the HAB to correctly delimit the change in colour per grain.

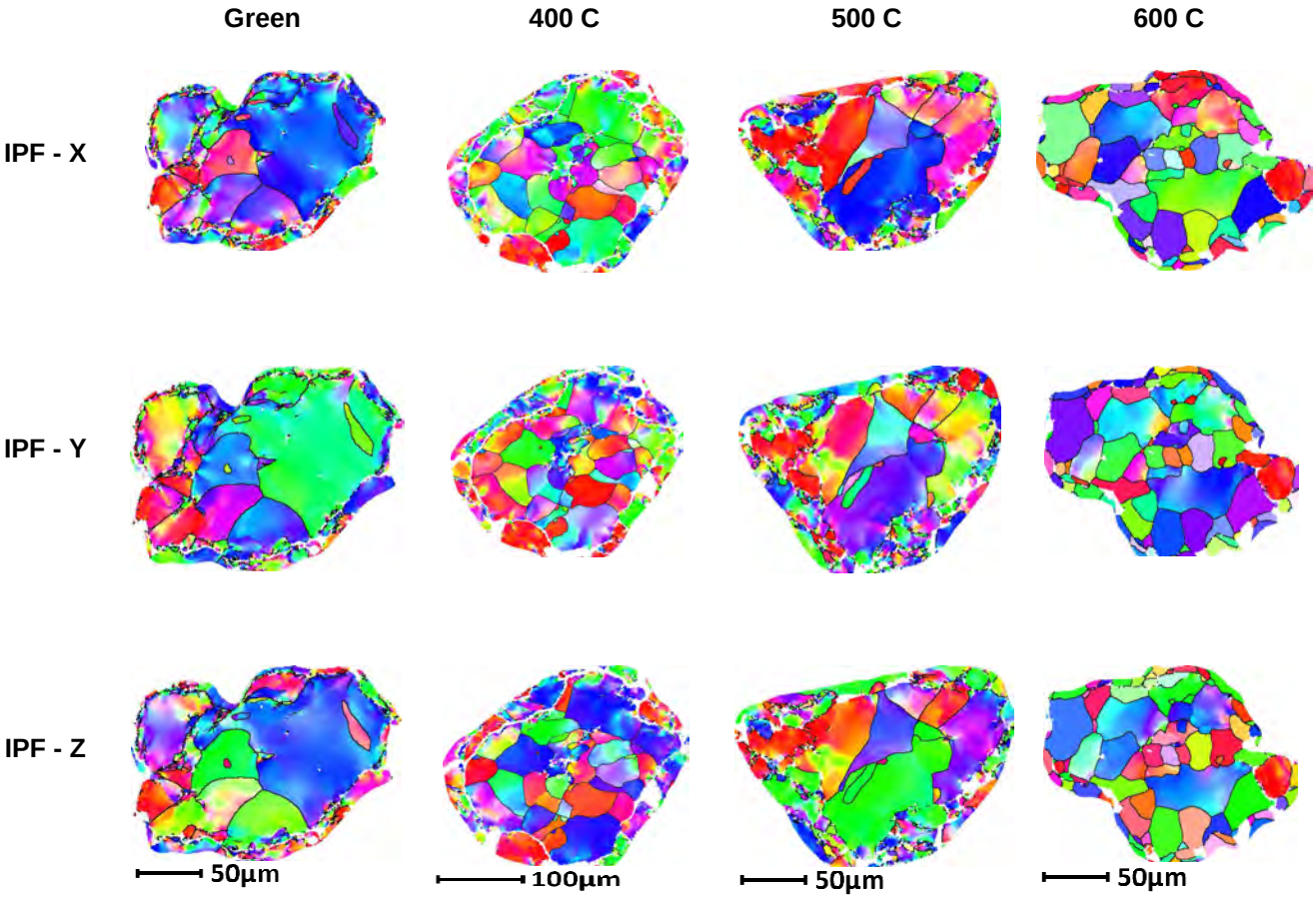

Figure 5.1.4 – IPF colouring maps over single particles

A random orientation of all grains is shown in all particles, each one having a clearly different colour. The watery colours correspond to the deformed grains, while the defined ones correspond to the recrystallized or unstrained grains.

5.2 Nanoindentation measurements performed in Particles of Components compacted at 800MPa

The areas, where the nanoindentation tests were performed, were selected as a function of the amount of misorientation observed in the EBSD pictures. The Low Angle Misorientation images (below 2º) gave an idea of the highly strained areas, and also the zones free of stresses. Both were included under the scope of the nanoindentation matrix, trying to obtain a wide range of hardness values within a particle. Also the areas where the recrystallization was not clear for the EBSD criteria, were analysed using the nanoindentation technique.

5.2.1 Particle in Green Component

A big particle of 170x115 µm was chosen, and the nanoindented area covered the centre till the edge of the particle, close to the contact with the other particle, as can be seen in Figure 5.2.1a.

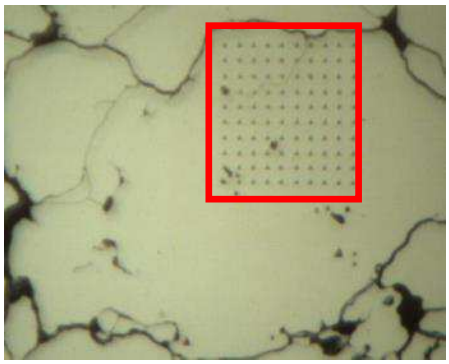

Figure 5.2.1a – Optical image of the particle after the nanoindentation

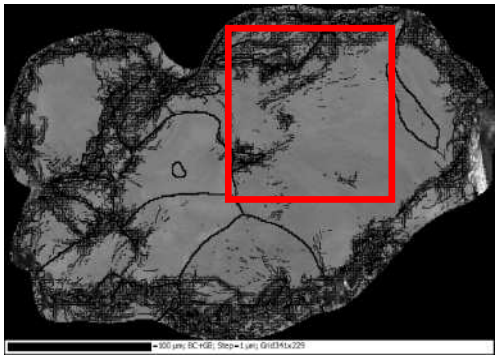

Figure 5.2.1b – HAB and LAB, mapped over the Band Contrast

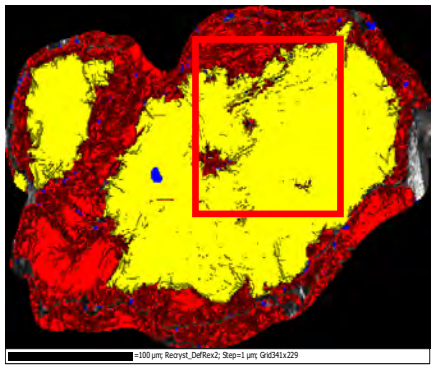

Figure 5.2.1c – Recrystallization and LAB Map, where deformed areas are shown in Red

The nanoindentation results are shown in the following two figures:

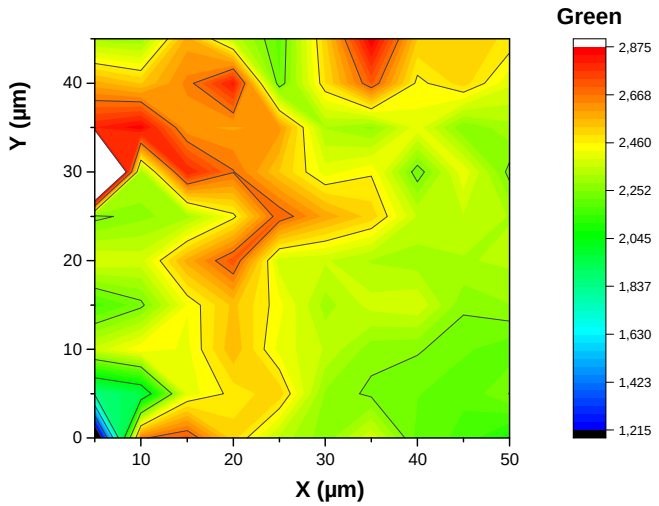

Figure 5.2.1d – Nanohardness map of Matrix performed on a particle of a green component

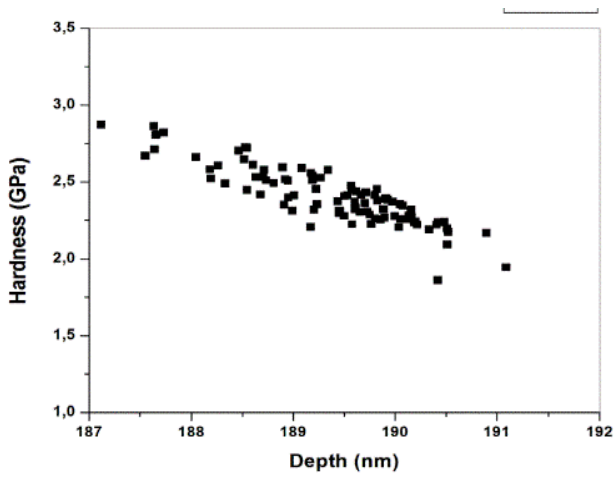

Figure 5.2.1e – Nanohardness values of Matrix performed on a particle of a green component

5.2.2 Particle in Component Heat Treated at 400ºC

Four nanoindentation maps were performed in a big particle found in a sample heat treated at 400ºC, named respectively Map 1 to 3 and the last one Map-Edge, as shown in Figure 5.2.2a.

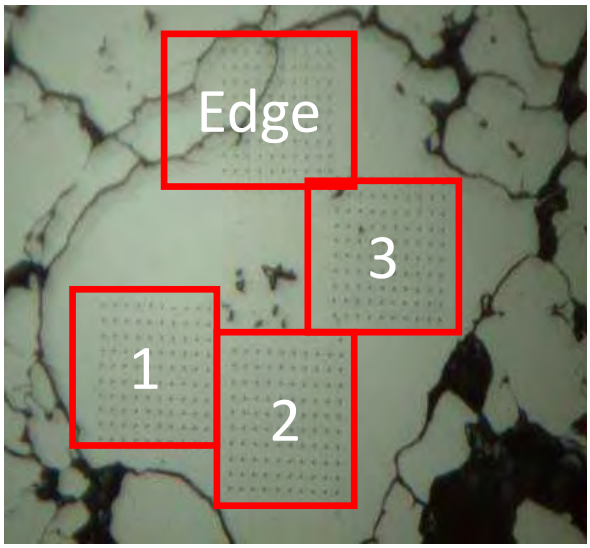

Figure 5.2.2a – Optical image of the nanoindentation matrixes performed on a particle of a component heat treated at 400ºC

In Figures 5.2.2b to 5.2.2d values of nanohardness are represented in contour maps, corresponding to matrixes 1 to 3 respectively.

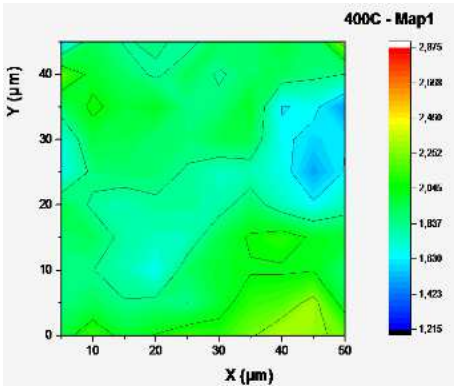

Figure 5.2.2b – Nanohardness map of Nanoindentation Matrix 1 on a particle of a component heat treated at 400ºC

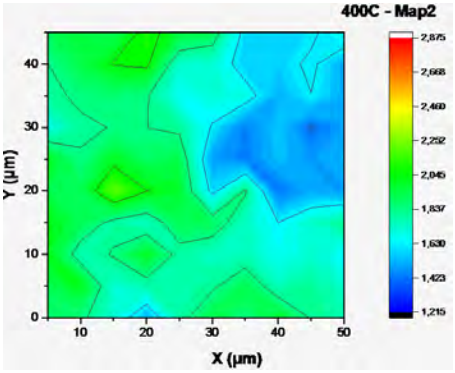

Figure 5.2.2c – Nanohardness map of Nanoindentation Matrix 2 on a particle of a component heat treated at 400ºC

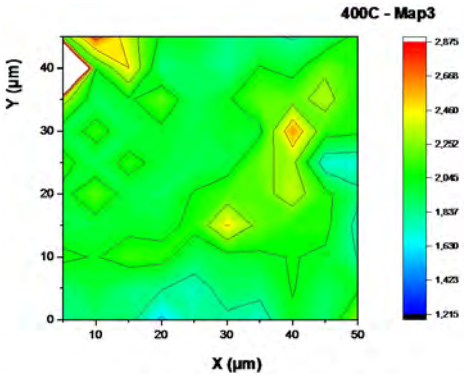

Figure 5.2.2d – Nanohardness map of Nanoindentation Matrix 3 on a particle of a component heat treated at 400ºC

The most representative information is extracted from the nanoindentation matrix performed on the edge of the particle, coupled in Figures 5.2.2f and 5.2.2g to the LAB and the Recrystallization respectively.

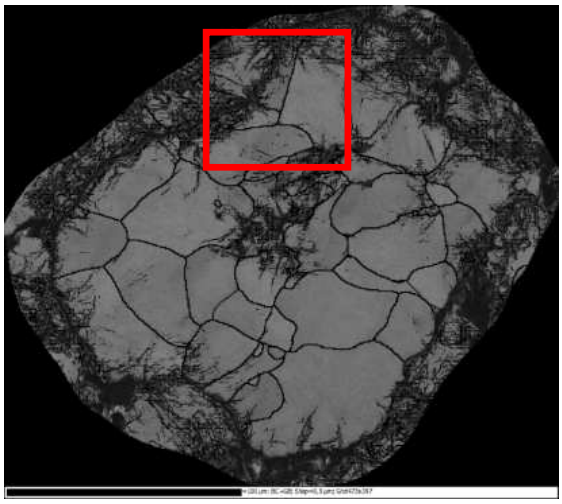

Figure 5.2.2e – Low Angle Boundaries represented over Band Contrast on a particle of a component heat treated at 400ºC

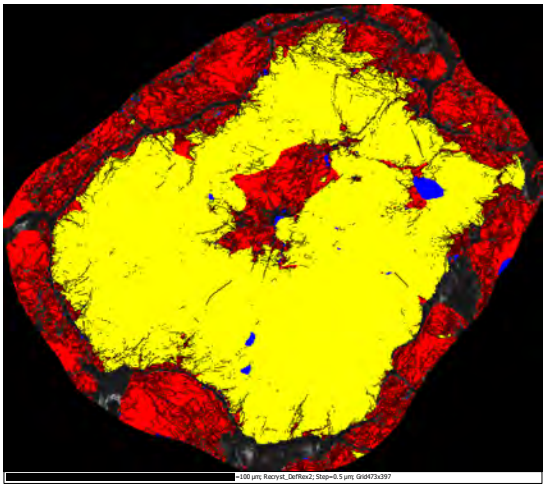

Figure 5.2.2f – Low Angle Boundaries and Recrystallization factor on a particle of a component heat treated at 400ºC

The nanoindentation results from the matrix performed on the edge are shown in Figures 5.2.2g and 5.2.2h.

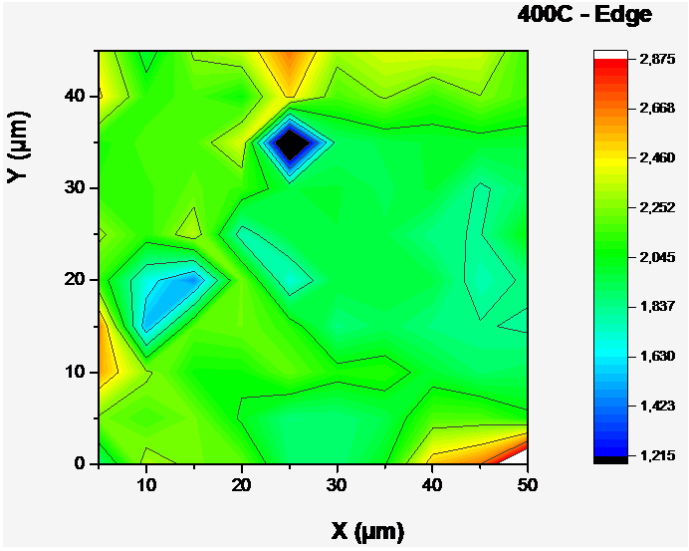

Figure 5.2.2g – Nanohardness map of Matrix performed on the edge of a particle of a component heat treated at 400ºC

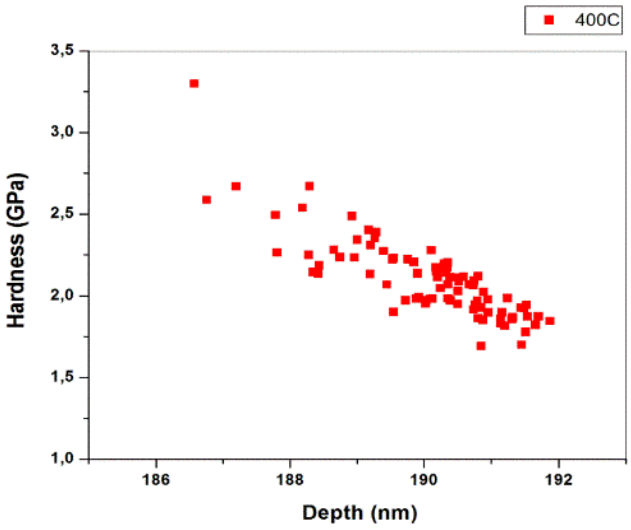

Figure 5.2.2h – Nanohardness values of Matrix performed on the edge of a particle of a component heat treated at 400ºC

5.2.3 Particle in Component Heat Treated at 500ºC

Two nanoindentation matrixes were performed in a big particle found in a sample heat treated at 500ºC, named Map 1 and Map-Edge. The results of Map 1, coupled with the Low Angle Boundaries image of the particle are shown in Figures 5.2.3c and 5.2.3b respectively.

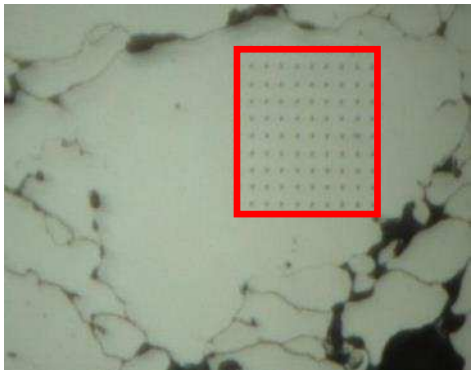

Figure 5.2.3a – Optical image of a particle of a component heat treated at 500ºC after a nanoindentation test

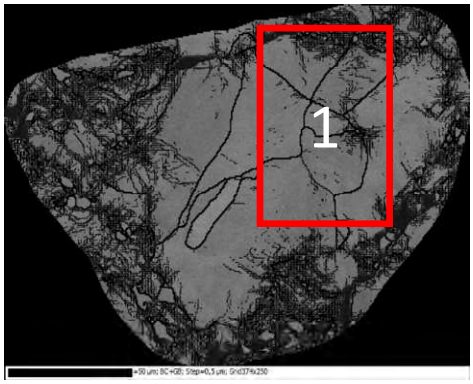

Figure 5.2.3b – Low Angle Boundaries image of a particle of a component heat treated at 500ºC

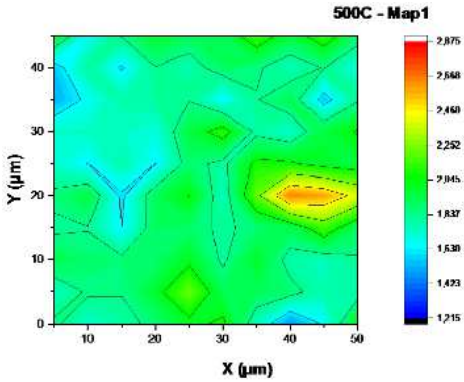

Figure 5.2.3c – Nanohardness contour map of Matrix 1 performed on a particle of a component heat treated at 500ºC

The matrix performed on the edge of the particle reveals some relevant information about the recrystallization, and the formation of new grains, shown as small areas free of low angle boundaries (see Figure 5.2.3 f) within the reach of the nanoindentation test.

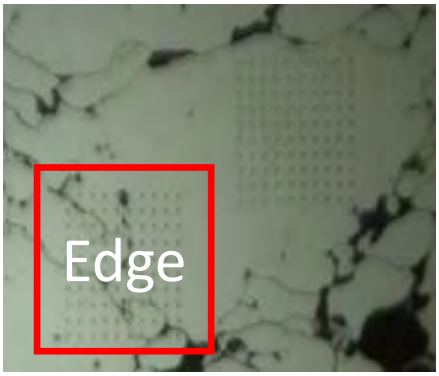

Figure 5.2.3d – Optical image of a particle of a component heat treated at 500ºC after a second nanoindentation test performed over the contact area with other particle

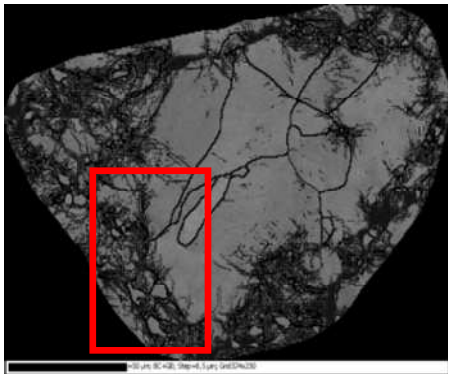

Figure 5.2.3e - Low Angle Boundaries image of a particle of a component heat treated at 500ºC. Red framework shows the approximate area where the Nanoindentation matrix on the edge was performed

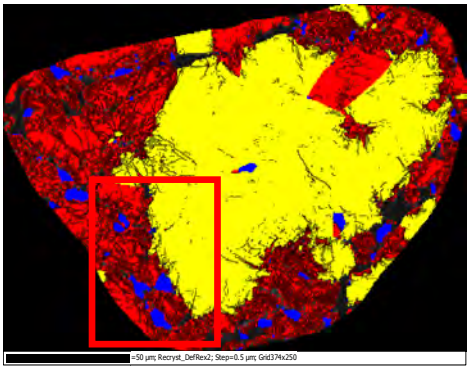

Figure 5.2.3f – Low Angle Boundaries and Recrystallization factor on a particle of a component heat treated at 500ºC

The nanohardness contour map and the values of the nanoindentation test are shown in Figures 5.2.3g and 5.2.3h respectively.

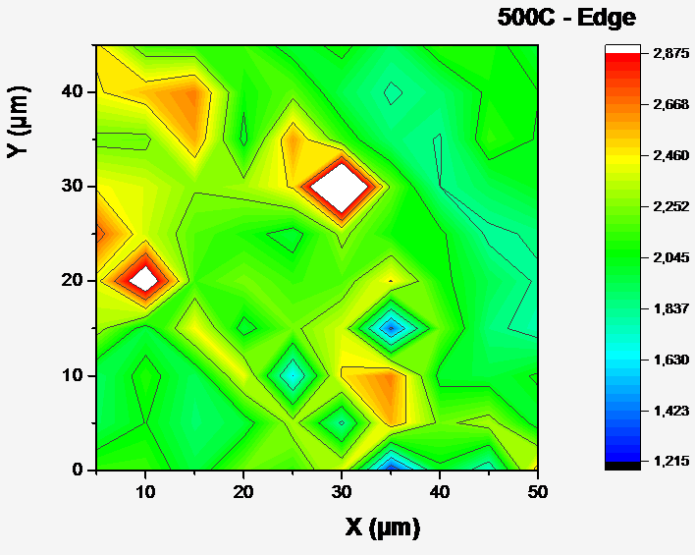

Figure 5.2.3g – Nanohardness contour map of test performed on the edges of a particle of a component heat treated at 500ºC

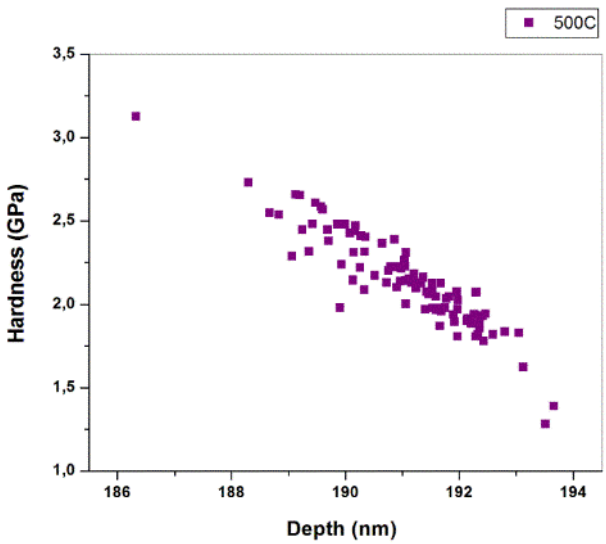

Figure 5.2.3h – Nanohardness values of Matrix performed on the edge of a particle of a component heat treated at 500ºC

5.2.4 Particle in Component Heat Treated at 550ºC

Two nanoindentation matrixes were performed in a big particle found in a sample heat treated at 550ºC, named Map 1 and Map-Edge. The results of Map 1, coupled with the Low Angle Boundaries image of the particle are shown in Figures 5.2.4c and 5.2.4b respectively.

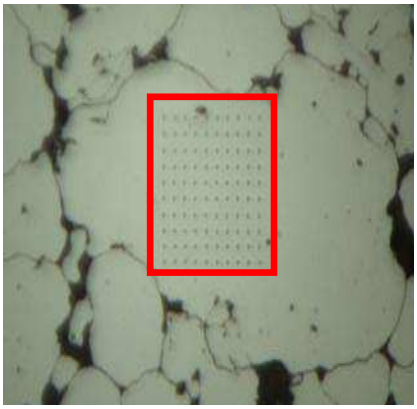

Figure 5.2.4a – Optical image of a particle of a component heat treated at 550ºC after a nanoindentation test

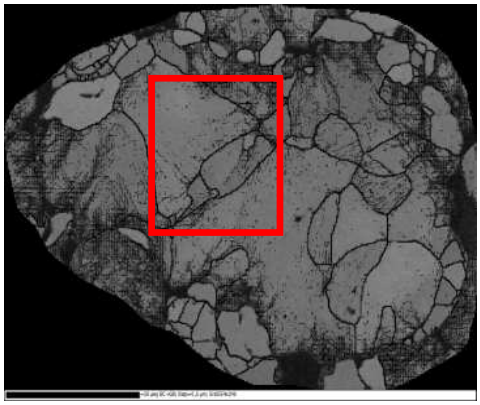

Figure 5.2.4b – Low Angle Boundaries image of a particle of a component heat treated at 550ºC

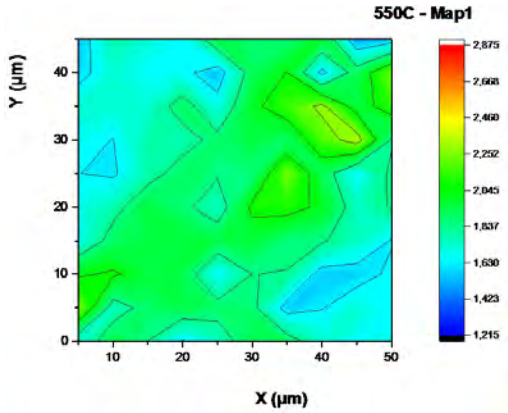

Figure 5.2.4c – Nanohardness contour map of Matrix 1 performed on a particle of a component heat treated at 550ºC

The matrix performed on the edge of the particle reveals some relevant information about the recrystallization, and the formation of new grains, shown as small areas free of low angle boundaries (see Figure 5.2.4f) within the reach of the nanoindentation test. In Figure 5.2.4f Recrystallized areas are shown in blue.

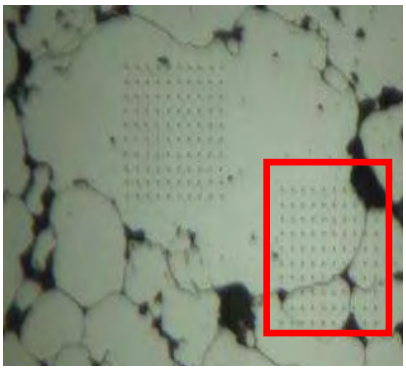

Figure 5.2.4d – Optical image of a particle of a component heat treated at 550ºC after a second nanoindentation test performed over the contact area with other particle

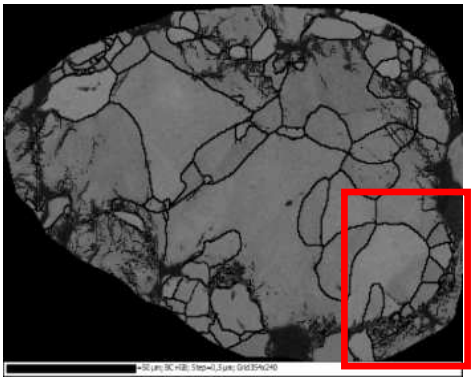

Figure 5.2.4e - Low Angle Boundaries image of a particle of a component heat treated at 500ºC. Red framework shows the approximate area where the Nanoindentation matrix on the edge was performed

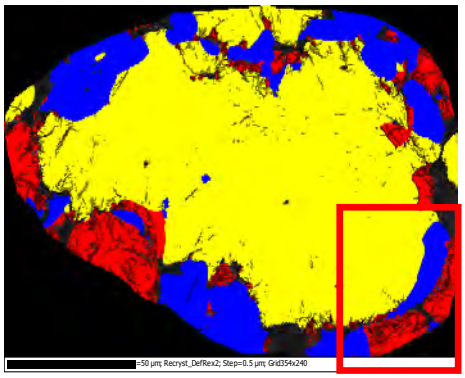

Figure 5.2.4f – Low Angle Boundaries and Recrystallization factor on a particle of a component heat treated at 500ºC

The nanohardness contour map and the values of the nanoindentation test are shown in Figures 5.2.4g and 5.2.4h respectively.

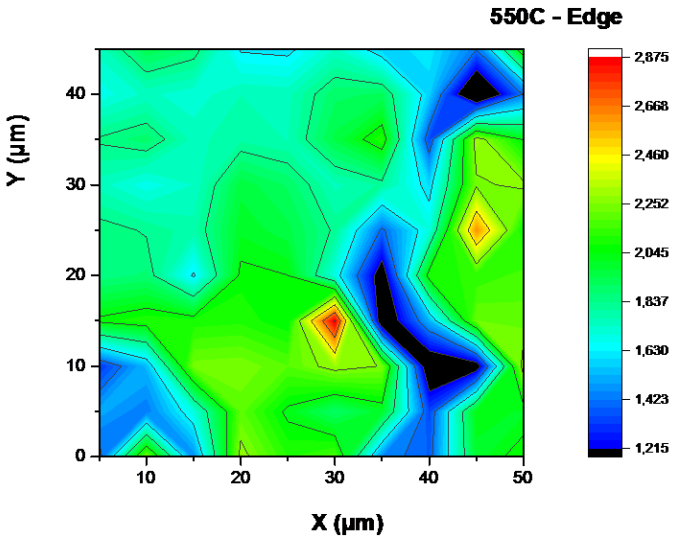

Figure 5.2.4g – Nanohardness contour map of test performed on the edges of a particle of a component heat treated at 550ºC

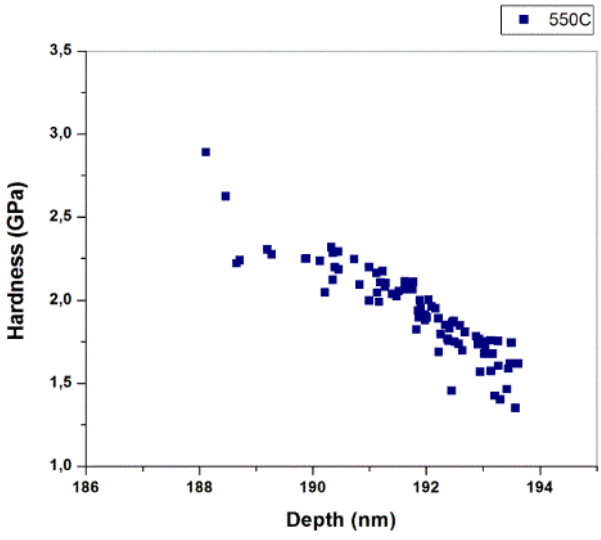

Figure 5.2.4h – Nanohardness values of Matrix performed on the edge of a particle of a component heat treated at 550ºC

5.2.5 Particle in Component Heat Treated at 600ºC

A big particle was examined, so the nanoindented area was able to cover a wide area from stress free zones to high concentration of low angle boundaries, as can be seen in Figure 5.2.5b.

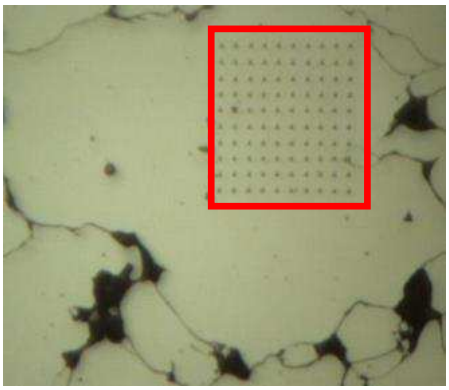

Figure 5.2.5a – Optical image of the particle on component heat treated at 600ºC after the nanoindentation

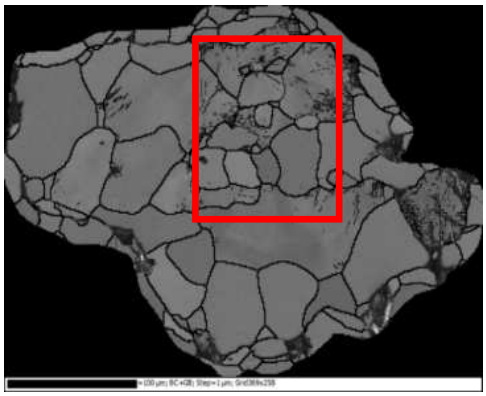

Figure 5.2.5b – Low Angle Boundaries, below 2º, mapped over the Band Contrast on a particle belonging to a component heat treated at 600ºC

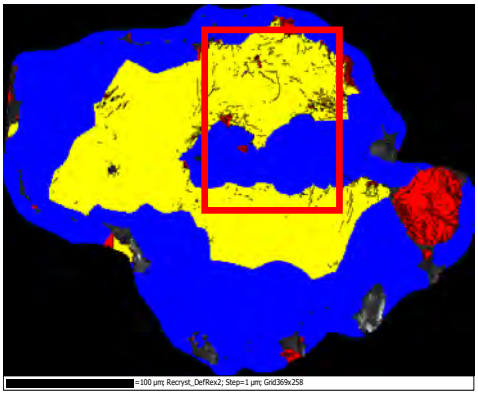

Figure 5.2.5c – Recrystallization and Deformed areas (Red) over Band Contrast and Low Angle Boundaries

The nanoindentation results are shown in the following two figures:

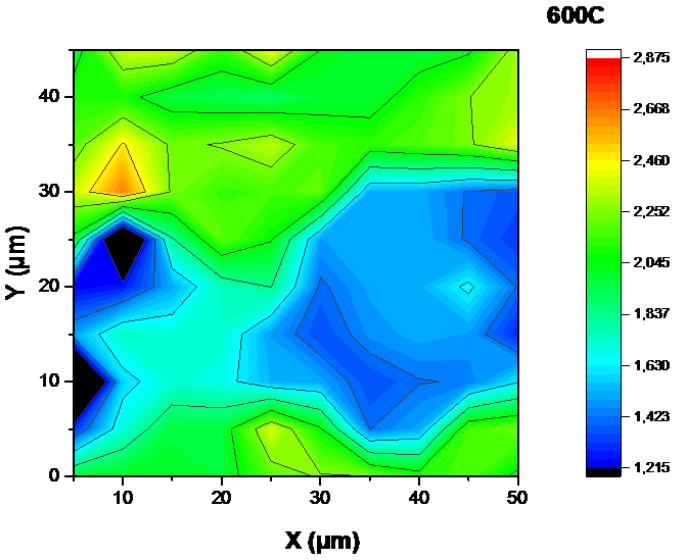

Figure 5.2.5d – Nanohardness map of Matrix performed on a particle of a green component

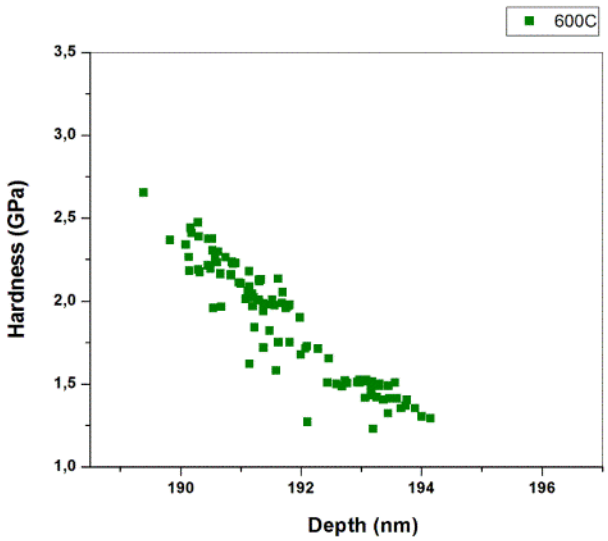

Figure 5.2.5e – Nanohardness values of a Matrix performed on a particle belonging to a component heat treated at 600ºC

5.2.6 Comparison of Green and 600ºC nanoindentation results

When comparing extreme values, a decreasing tendency in the hardness values is depicted in Figure 5.2.6, where an overlap of low values of the Green component with the high values of the 600ºC can be observed.

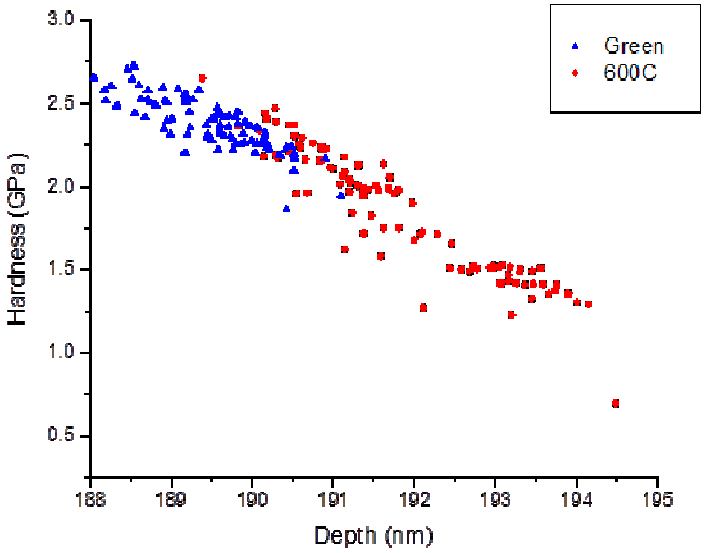

Figure 5.2.6 – Representation of Green and 600ºC hardness values

5.2.7 Comparison of all Nanoindentation results

Results of maps at the edges at intermediate temperatures have been plotted along with the values for Green and 600ºC matrixes, these values being the extremes of the scattering. For the cases of 400ºC, 500ºC and 550ºC values remain in the middle of these extremes, both in hardness and in depth.

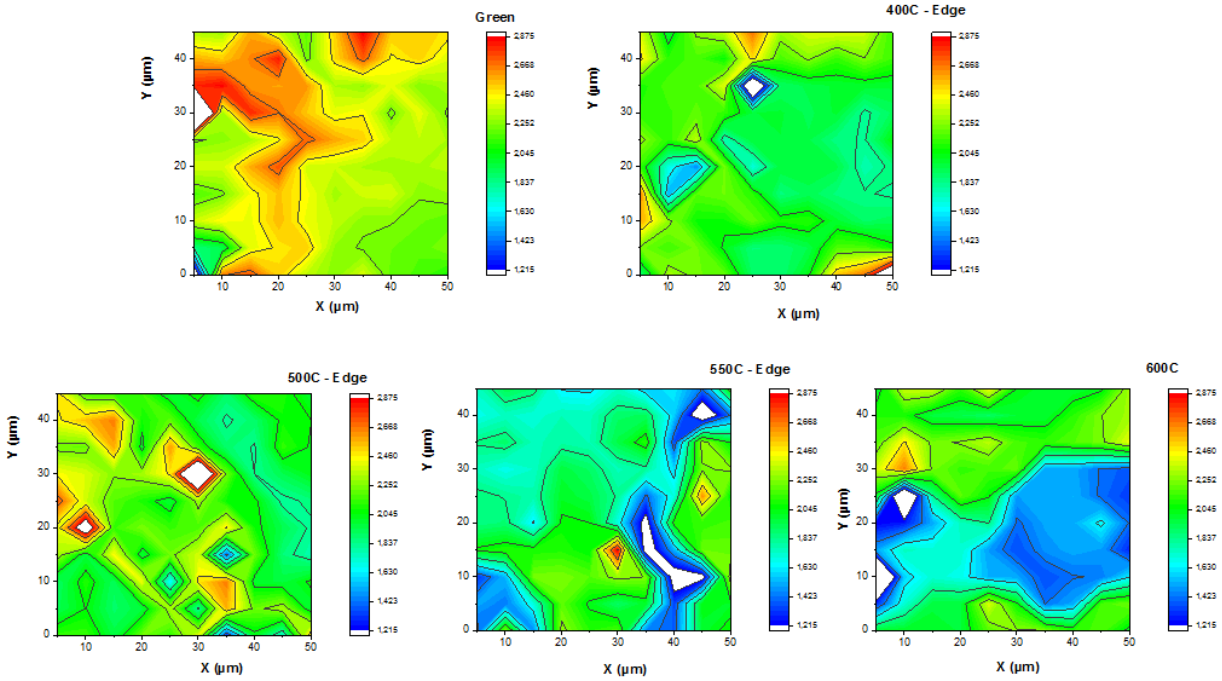

Figure 5.2.7 – Contour maps of hardness values of all conditions

5.3 Analysis of Big Areas on the Cross Section of Final Components compacted at 800MPa

5.3.1 EBSD imaging

Following the same structure as for the particle analysis, High Angle Boundaries (HAB) and Low Angle Boundaries (LAB) maps will be taken into account for this section, revealing the evolution of the microstructure over temperature.

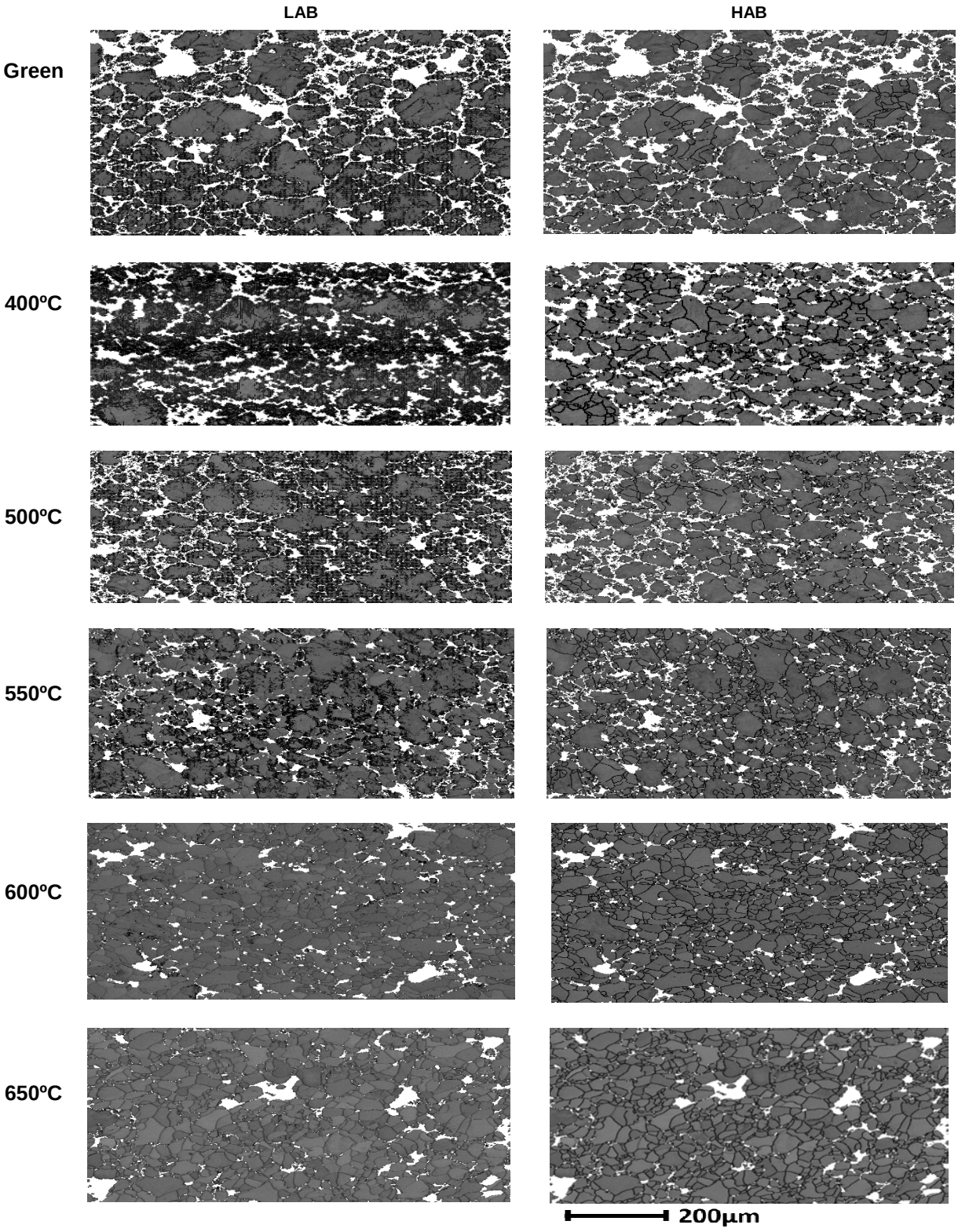

Figure 5.3.1a – HAB and LAB maps for 800MPa big areas

Recrystallization maps are shown in Figure 5.3.1b, where the evolution from deformed to recrystallized material can be visualized:

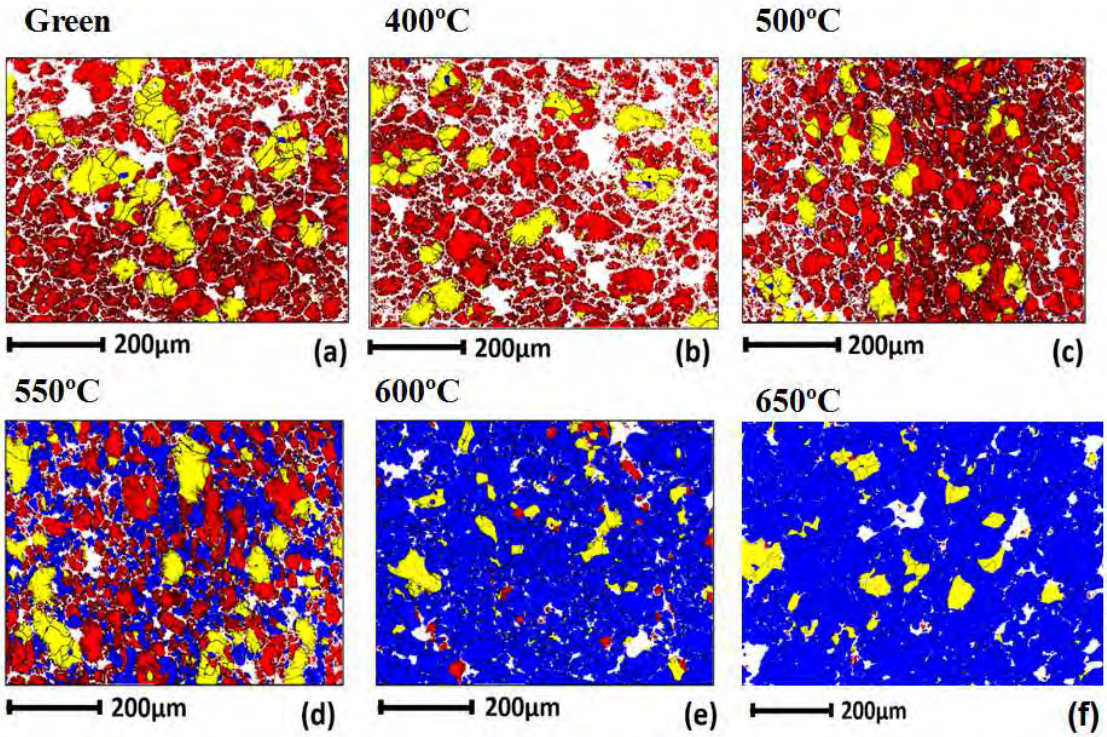

Figure 5.3.1b – Recrystallization Factor maps of Big Areas of 800MPa components

5.3.2 Grain size analysis

Two big areas were mapped, one on the edge of the cross section, and other one in the centre, both using identical EBSD set up described in section 4.1. Figure 5.4.2a, shows the grain probability over the grain size, in other words, the probability of finding a grain of a specific size, and its evolution over temperature for the 800MPa compaction pressure. Next to it, the fraction of the area covered per grain of different sizes, over the total area considered is also shown in Figure 5.4.2b.

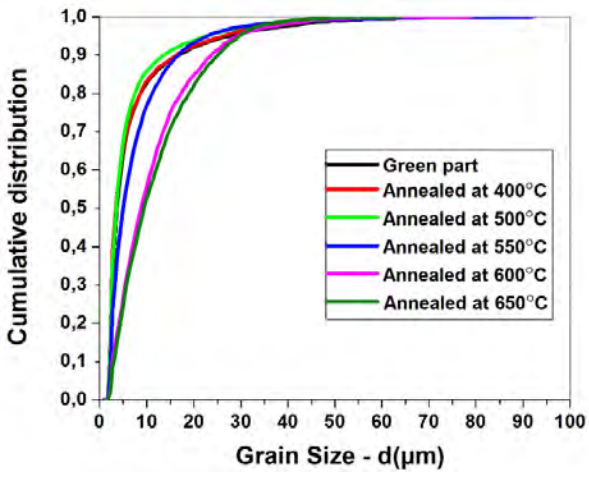

Figure 5.3.2a – Probability over grain size

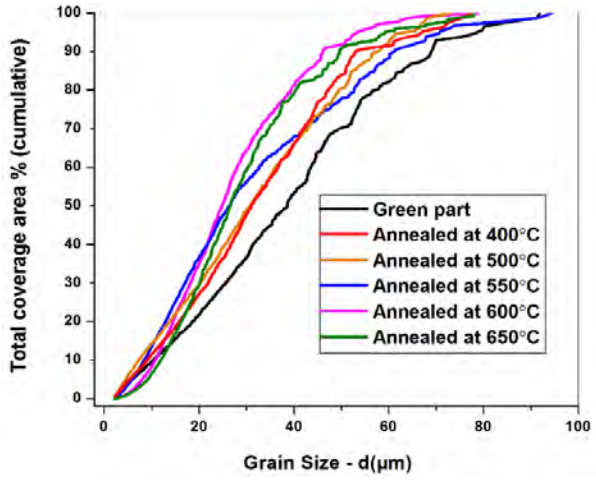

Figure 5.3.2b – Area coverage over grain size

- **Mean, median and maximum values**

The following data are extracted from the study of both maps, on the edge and in the centre of the cross section. For the mean calculation, the numbers of grains in batches of 0.5µm of difference in diameter have been studied. For the median analysis, grains from both maps have been sorted together from biggest to smallest, giving a statistical idea of the grain size in one given area.

800MPa	Green	400C	500C	550C	600C	650C
Mean (µm)	7,52	7,16	6,62	8,14	11,69	12,25
Median (µm)	4,07	3,74	3,91	5,41	9,17	9,96
Max. (µm)	91,87	77,41	73,34	94,44	78,97	77,92

Figure 5.3.2c – Mean, Median and Maximum values for grains of big areas at 800MPa components

5.3.3 Low Angle Boundaries

The following Figure 5.4.3a shows the distribution and evolution of low angle boundaries density, in a cumulative way, over the value of the misorientation angle. It gives the idea of the degree of misorientations and its influence over the whole area considered, two maps in this case.

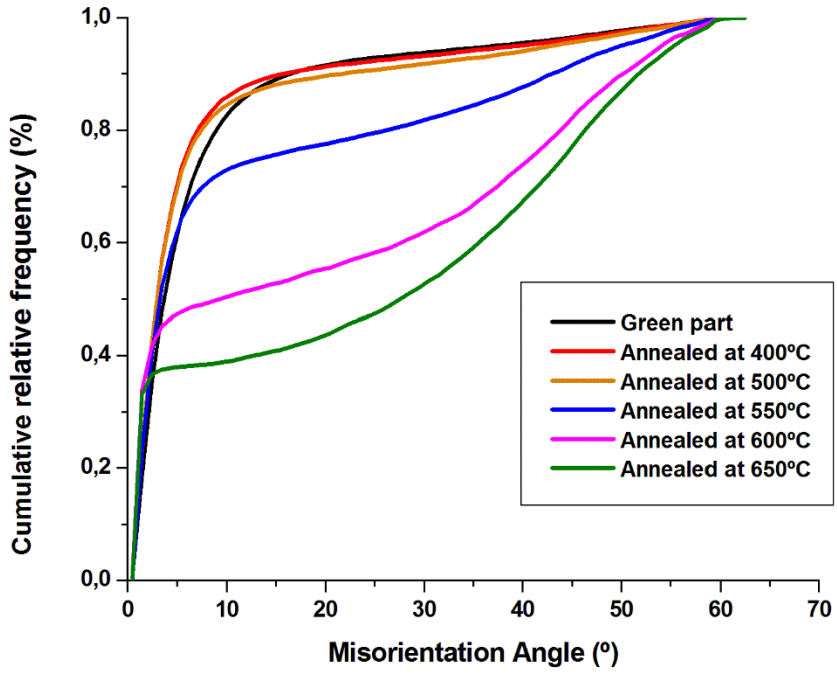

Figure 5.3.3 – Low Angle boundaries evolution over annealing temperatures (800MPa)

5.3.4 Boundary density parameter

The boundary density parameter express the relation between the length of the HAB, using the *circle equivalent diameter*, and the area contained per grain, in function of the temperatures.

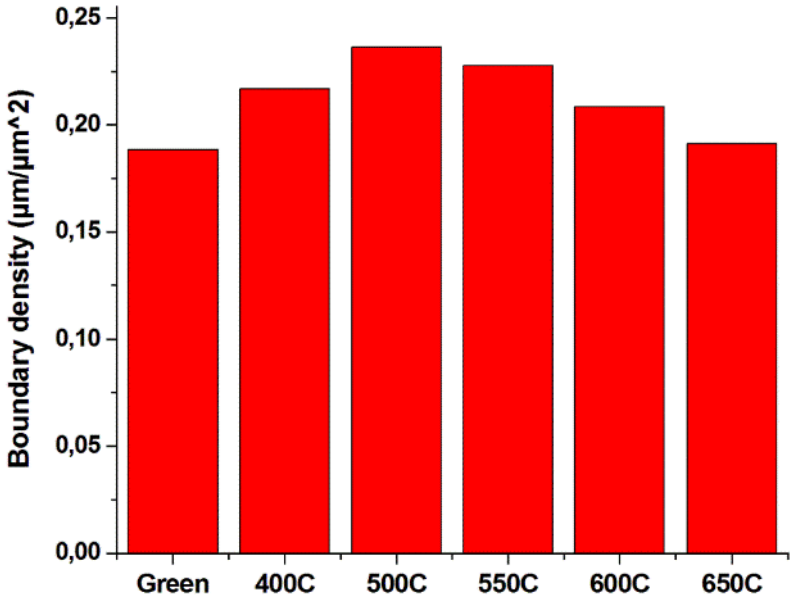

Figure 5.3.4 – Boundary parameter for big areas of the cross section of components compacted at 800MPa

5.3.5 Recrystallization

Setting the parameters for the recrystallization factor in an identical way of the nanoindentation performed shown in section 5.2, the following values are registered considering the two maps at 800MPa, edge and centre, and the total area analysed.

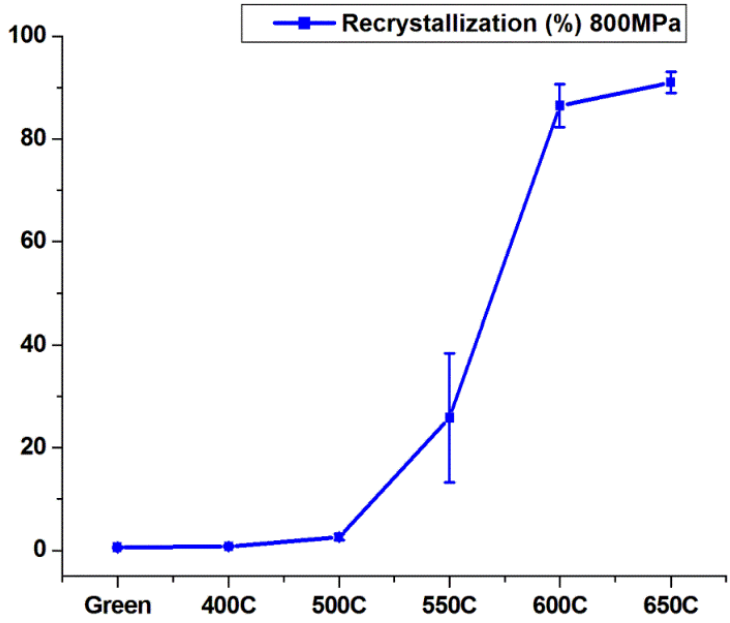

Figure 5.3.5 – Recrystallization factor over temperature (800MPa)

5.3.6 Texture analysis

These IPF coloured maps in Figure 5.3.6a and IPF figures in 5.3.6b show the orientation distribution over the area.

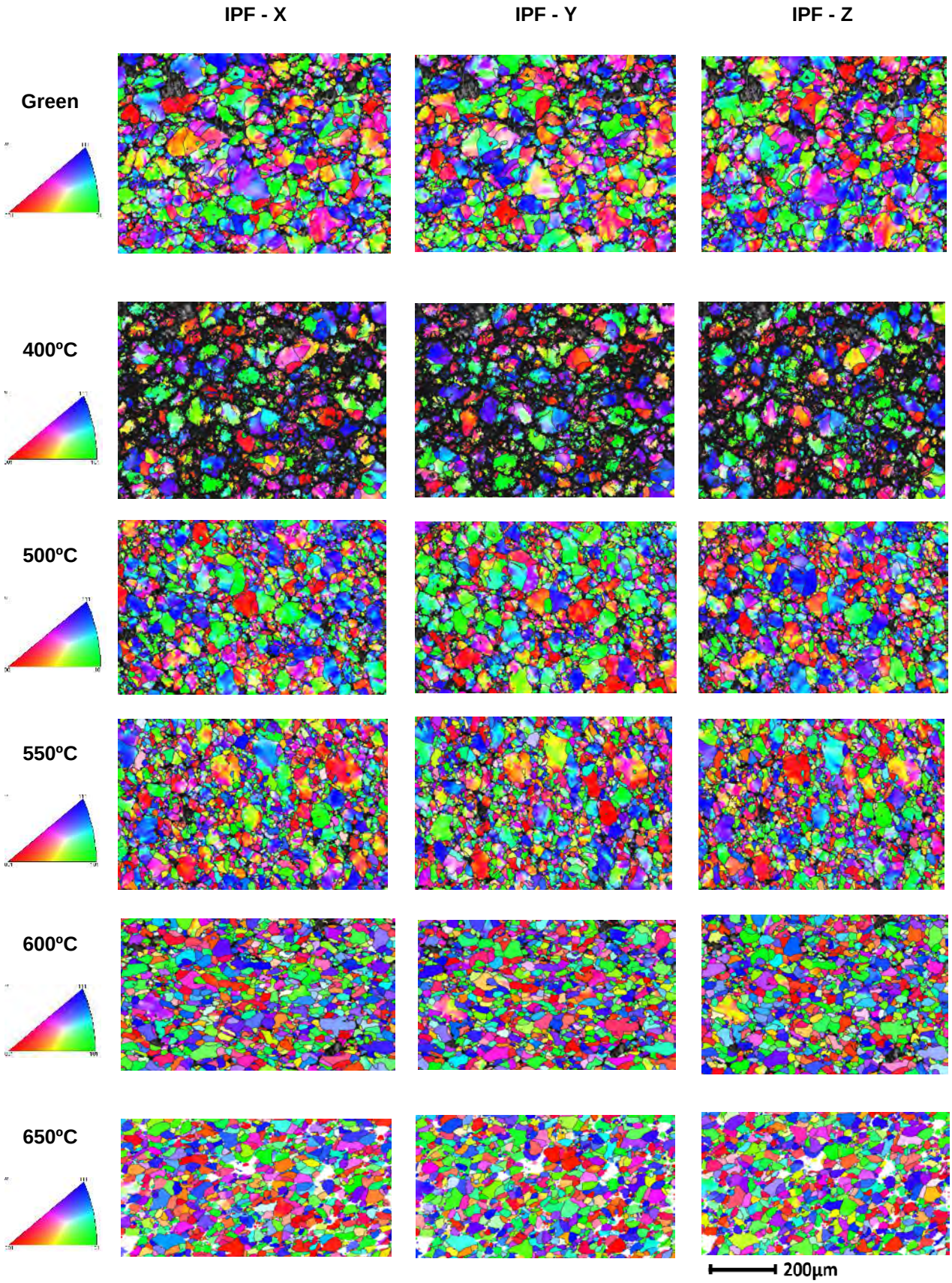

Figure 5.3.6a – IPF colouring maps over big areas of 800MPa compacted components

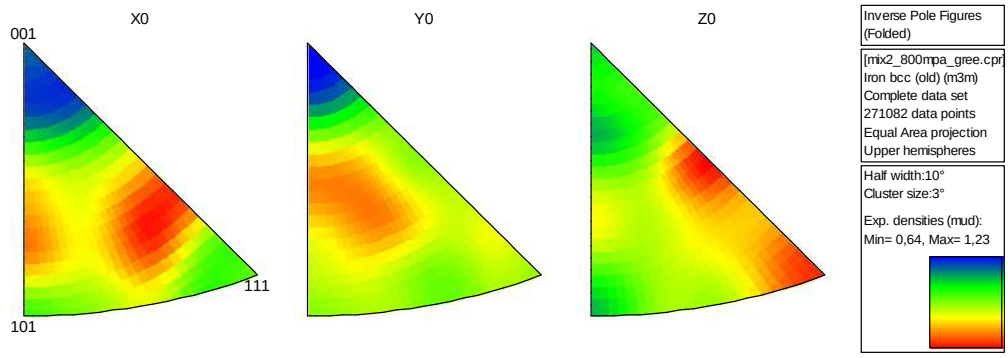

GREEN

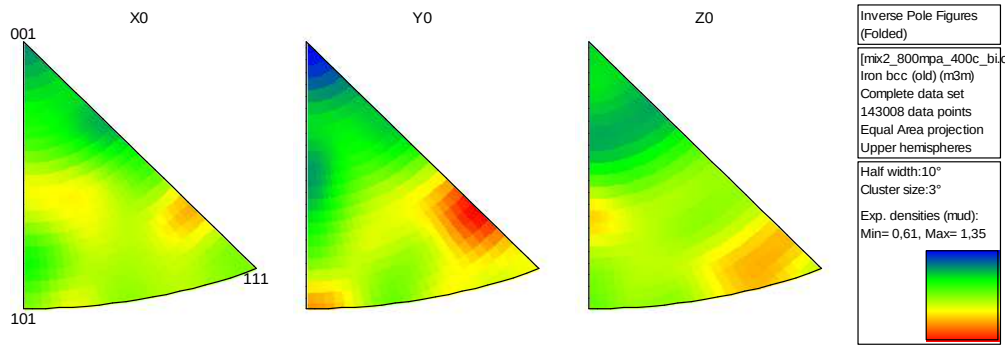

400ºC

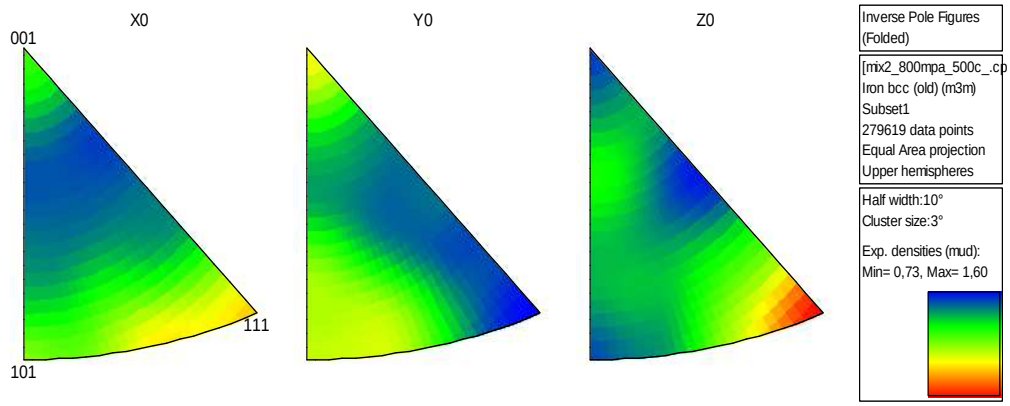

500ºC

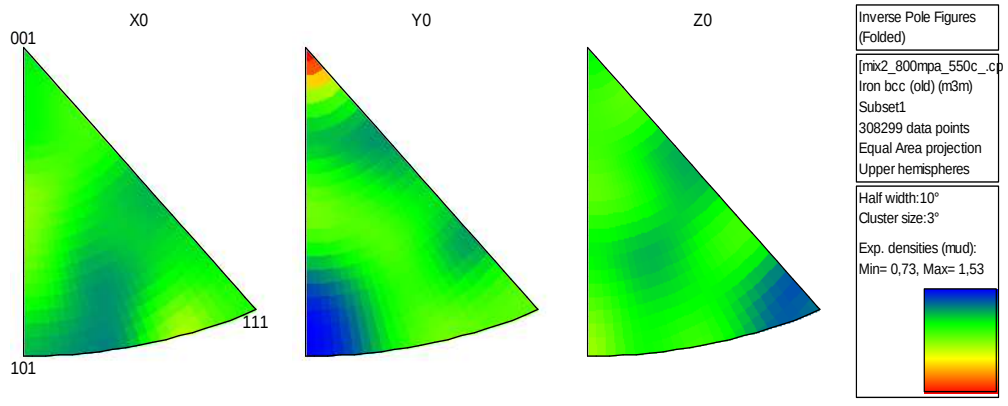

550ºC

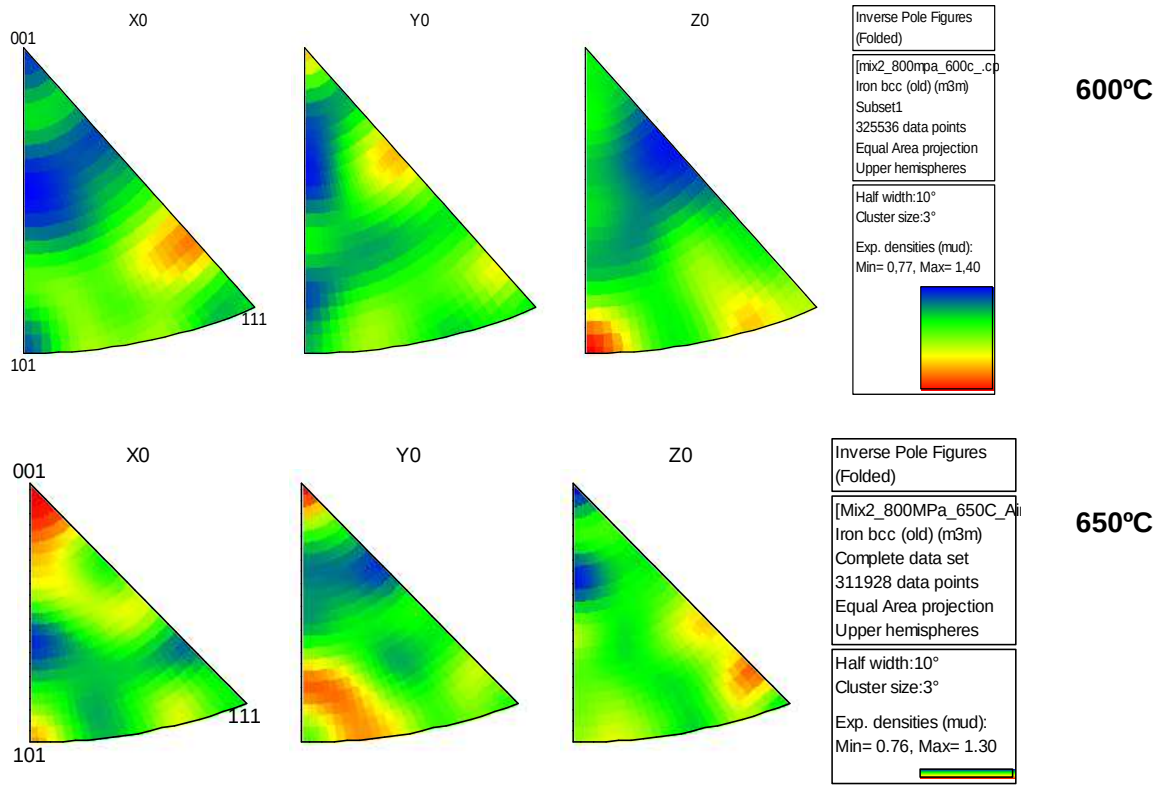

Figure 5.3.6b – IPF of big areas of 800MPa compacted components

Both IPF maps, and Inverse Pole Figures reveal a random texture of a big area of the cross section of the rings, since the same order of magnitude in the points indexed on the EBSD is obtained, and the minimum and maximum values of the distribution in Exp. Densities remain close in magnitude, revealing a non-preferential orientation in the microstructure.

5.4 Magnetic tests

5.4.1 Resistivity tests

The resistivity tests described in section 4.3.1 were performed over three rings per condition. The representation of the values and its corresponding deviation is shown in Figures 5.4.1, both sorted by temperature and pressure showing the influence of both parameters. Resistivity values of green rings are not comparable to the heat treated samples, since the delubrication had not taken place, and that is why these results are not shown in Figure 5.4.1. All values can be found in Appendix B.

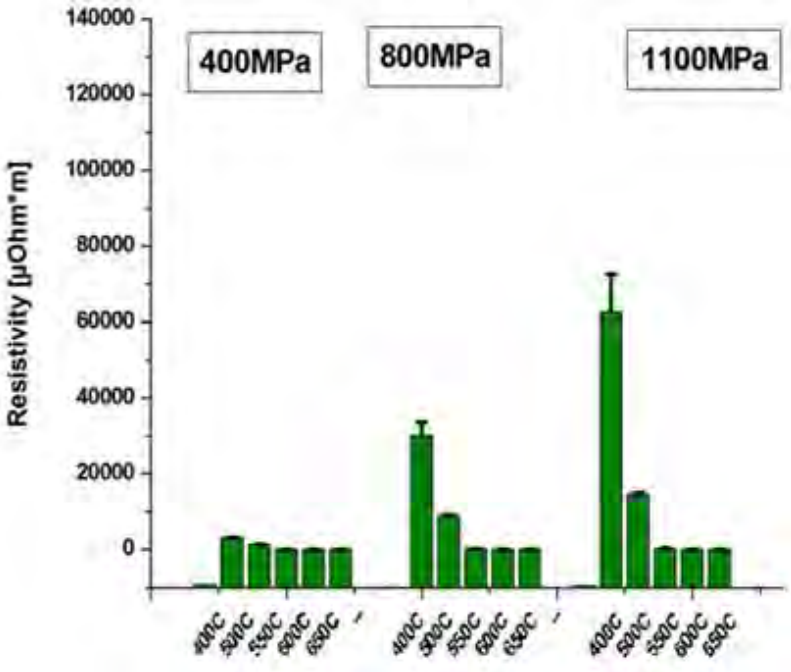

Figure 5.4.1 – Resistivity Plot in function of the pressure in the compaction process

5.4.2 DC tests

The DC results shown in table 5.6.2 were performed at Höganäs AB, measuring the properties per unit of mass of three rings per condition. Among others, the following properties have been observed:

- Hc (A/m): Coercivity value of the sample, considering an ideal hysteresis loop discharging from 10000 A/m of magnetic field applied.
- μ_{max}: Maximum permeability achieved while inducing the first magnetic field
- Hysteresis Losses – E (mJ/kg): Energy product of the hysteresis loop, which is area contained within the curve and shows the energy losses due to the microstructural state.

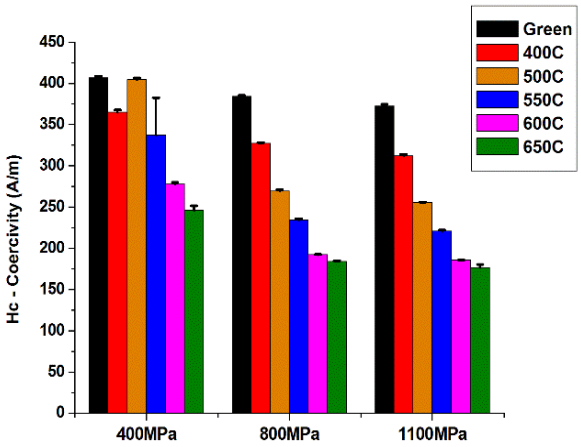

Figure 5.4.2a – Coercivity Plot in function of the temperature in the heat treatment

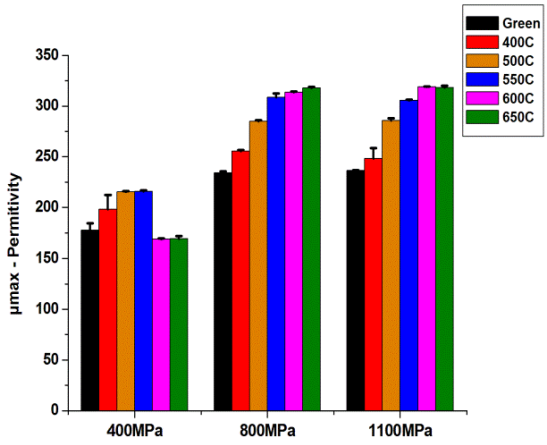

Figure 5.4.2b – Permeability Plot in function of the temperature in the heat treatment

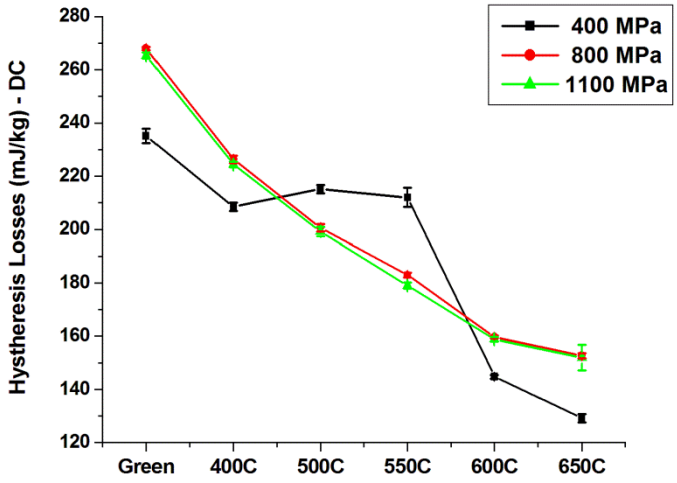

Figure 5.4.2c – Hysteresis Losses obtained for different temperatures and compaction pressures

Other parameters measured, like Bmax defined below, and the numeric values of all these parameters can be found in Appendix B:

- B_{max} (T): Maximum magnetic induction achieved on the sample, dependant on the intensity of the magnetic field applied, in our case always 10.000 A/m

5.5 TRS

The TRS measurements previously described in section 4.4.1 were performed with three bars per condition. The representation of the values and its corresponding deviation is again shown as a function of temperature and pressure in figures respectively. High values were obtained for 400MPa, while in 800MPa and 1100Mpa series similar but lower values were obtained, as shown in Figure 5.5. Not significant effect of the pressure was observed between 800MPa and 1100MPa series

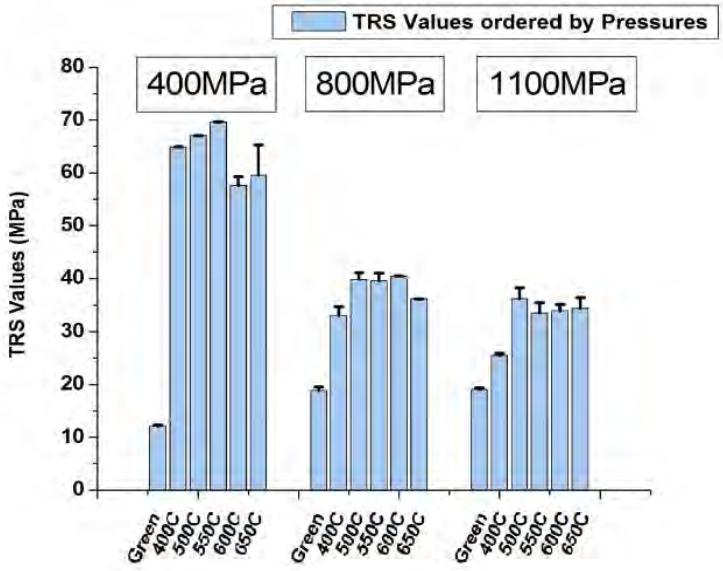

Figure 5.5 – TRS values in growing order of compaction pressure

All TRS values are shown in Appendix B, section iii.

6. Discussion

6.1 Microstructural Evolution

As can be observed in Figure 6.1a, the evolution of the LAB over temperature has a clear tendency in all conditions studied. The strain state is characterized by local misorientation factor, low angle boundaries and, to some degree, the recrystallization factor map which all give a clear idea of the relief of stresses during the annealing process, both for big areas and particles. Brewer et al (44) have correlated the misorientation mapping to the plastic deformation of their material. For the purpose of this investigation, the density of dislocations and the evolution of the strain state over the heat treatment of the strain state, into a more relaxed state, is assessed by means of EBSD (see section 5.3). In this context a trend is observed in the microstructure of the SMC component from a high density of dislocations to a lower one with increasing temperature. This is shown both in LAB maps (Fig. 5.3.1) and from the cumulative distribution of the LAGB (Figure 5.4.3.a). This effect is related to a lower hysteresis loss in the magnetic tests, while mechanical properties on the macro-scale (TRS) show no significant change. However, nanoindentation tests show a lower hardness values for unstrained and recrystallized areas, linking the magnetic and the mechanical properties through the microstructure.

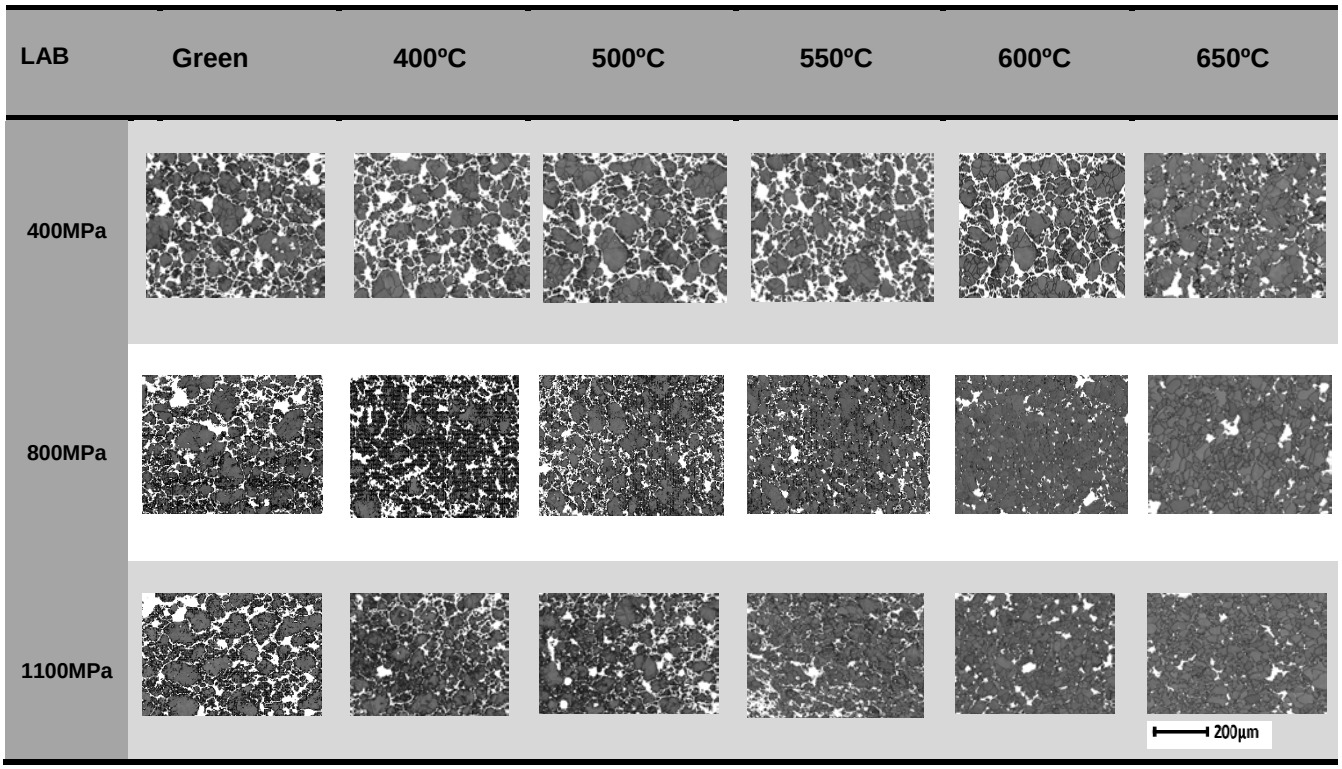

Figure 6.1 – LAB images for a big map per sample per condition

Besides the study of the distribution of strain, an investigation of the internal microstructure of powder particles is possible with EBSD; grains within particles are revealed, enabling a grain distribution analysis. Shokrollahi et al (45) stated that the particle size is a relevant factor to the magnetic properties of sintered soft magnetic materials; though microstructure is referred also as a relevant factor in the magnetic performance. The influence of the grain size within the powder particles is a determining parameter, since SMC materials are not sintered. The boundary parameter and the recrystallization factor show a definite path for the three stages of a heat treatment of a metal: recovery, recrystallization and grain growth (see section 2.2 for theoretical background and 5.3.2 and following sections for results).

From the cumulative probability plot and area coverage plots a shift in the size of the particles is observed starting at 550ºC, being more pronounced at 600 and 650ºC. The boundary density parameter represented in section 5.3.4 also shows a similar trend when comparing the perimeter and area of the grains considered. Mean and median values additionally indicate recrystallization and possibly the beginning of grain growth phenomena, both for 800 and 1100MPa series, while there is no clear trend in 400MPa series (see Appendix C).

In respect to the texture, IPF in section 5.3.6 show no preferential orientation for big areas considered in the cross section. Compaction direction (Y axis for all the maps) or the radial direction (X axis in the case of the rings), show no great differences in orientation of the all grains considered. The qualitatively random distribution of colours within neighbour grains and particles considered, shown in IPF couloring maps, ascertained by the small difference in the exp. densities of the IPF (both shown in section 5.3.6) is indicative of a material is behaving in an isotropic way.

6.2 Correlation of properties

6.2.1 Microstructure and Mechanical properties

Efforts trying to relate mechanical and magnetic properties had been done before (46), however the strained status of the powder based material, or its evolution over the annealing process have never been clearly stated.

In the case of the early maps performed on SMC particles, the observations of LAB and the local misorientation maps stated differences in strain state within neighbour grains considering the same particle. Small grains free of LAB first visualised on components heat treated at 500ºC, and complimentary nanoindentation tests lead to a robust assessment of the microstructural evolution. As it has been stated in section 5.2, nanoindentation and EBSD results correlate with respect to the LAB and the hardness values obtained. As it is shown in Figure 6.2.1a, new grains formed at the edge of the particles, show a lower value of hardness compared to the surroundings.

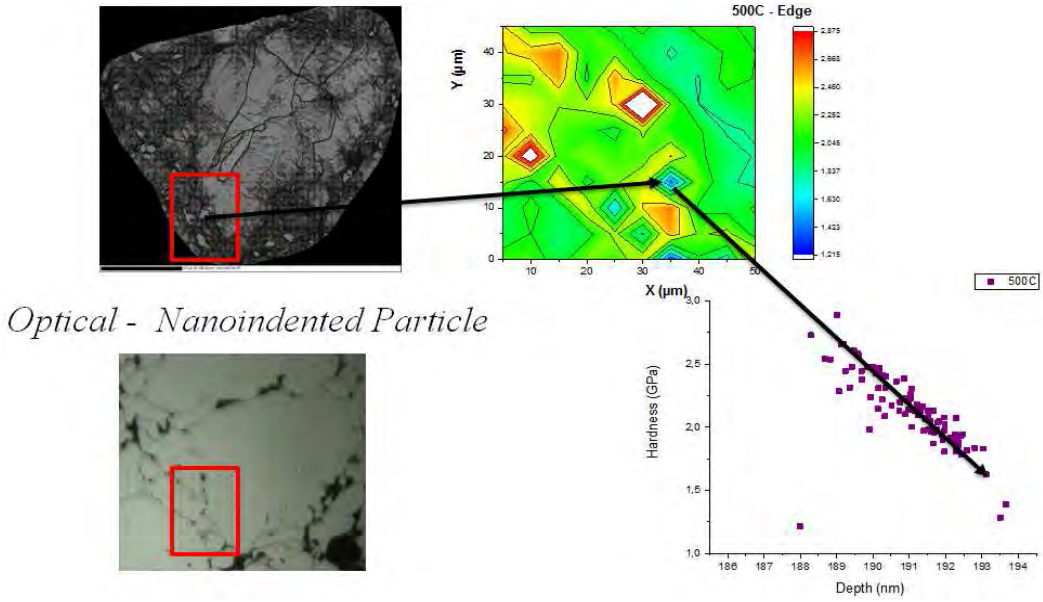

Figure 6.2.1a – Analysis of a recrystallized area both through EBSD and Nanohardness approach

Results from both EBSD and nanoindentation facilitate to more valid constructed recrystallization factor maps, by choosing the right parameters in order to consider a recrystallized grain (see Figure 6.2.1b).

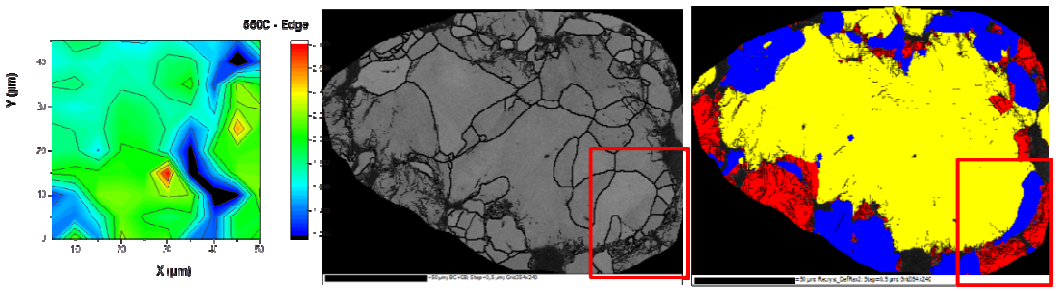

Figure 6.2.1b – Nanoindentation contour map (left), LAB-EBSD map (middle) and Recrystallization Factor map (right) of a single iron particle of a component compacted at 800MPa.

The recrystallization factor builds the maps considering the internal amount of strain per grain, being with yellow colour in the maps representing substructured grains that are neither entirely deformed nor recrystallized. In order to tune the angle boundary limits set in deformed and strain free regions, a conservative approach when building the maps was taken, by correlating the results obtained in the nanoindentation to the ones obtained from EBSD (see Figure 6.2.1b). Local misorientation maps also validate the recrystallization and substructured areas, since this approach is more strain-sensitive to depicting localized strain. In this manner, annealing and growth of recrystallized grains have been verified by means of several techniques, stating that the recrystallized areas (shown in blue in the EBSD maps) are in fact areas free of strain, both possible result of the stress relief during the annealing process or the recrystallization taking place in the deformed areas. By utilizing the recrystallization factor components in this way, quantification of the deformed, substructured and strain free areas is possible. From the recrystallization factor maps quantitative results based on the area covered by the grains were obtained, in which recrystallization percentage exceeds 50% of the area mapped, after 600ºC, as shown in section 5.3.5.

The fact that recrystallized grains appear on the edges of the particles reveal how the annealing process is taking place in a powder based material. Small grains appear on the highly deformed areas, normally where contact between particles has taken place. These grains grow later on, to the inside of the particles, and not the other way around. This result could also be responsible for the grain size reduction observed with increasing annealing temperature starting from a green component, as shown in the grain size and area distributions. It was also observed that, the central area of big particles as the ones mapped in this investigation, are subjected to little changes since these zones were not so much affected by the compaction or the recrystallization processes. The presences of substructure in these grains also indicate some degree of deformation which could be potential sites for recrystallization initiation.

6.2.2 Magnetic Behaviour and Microstructural Evolution

As stated in section 5.4, the magnetic performance of the material was evaluated for resistivity, AC and DC tests. In the case of resistivity, the effect of the coating should be considered as well as the plastic strain, which is disappearing over temperature.

DC results obtained are really similar for 800MPa and 1100MPa series. Coercivity was reduced over temperature, reaching stable values at 600 and 650ºC degrees. A similar behaviour was observed for the hysteresis losses. Permeability also shows a trend over temperature which could be explained by the microstructural change evaluated. 400MPa series results for DC show no trends with changing pressure or temperature.

AC behaviour was constant over pressures and temperatures for the three rings considered. Only changes in the orders of magnitude for different magnetic induction values (0.5T, 1T and 1.5T) are observed, as stated on the AC tests (Appendix B). The evolution of the eddy current losses is growing, represented by the linear fits, while hysteresis losses, constant value of the linear fit, decrease over temperature. The effect of a higher hysteresis loss at 650ºC is an artefact from the linear fit performed, confirmed by the hytheresis losses observe in the DC measurements (section 5.4.2).

These hysteresis losses can be related to the microstructural status of the components. By utilizing the EBSD technique the microstructure has been evaluated in multiple ways. Regarding the Recrystallization Factor represented in Figure 6.2.2, the area covered by new grains free of strain observed on the edges of the particles, free of strain, will have a strong influence on the final hysteresis losses values. Thus, the higher the degree of recrystallization induced by the treatment of the material will lead to lower hysteresis losses.

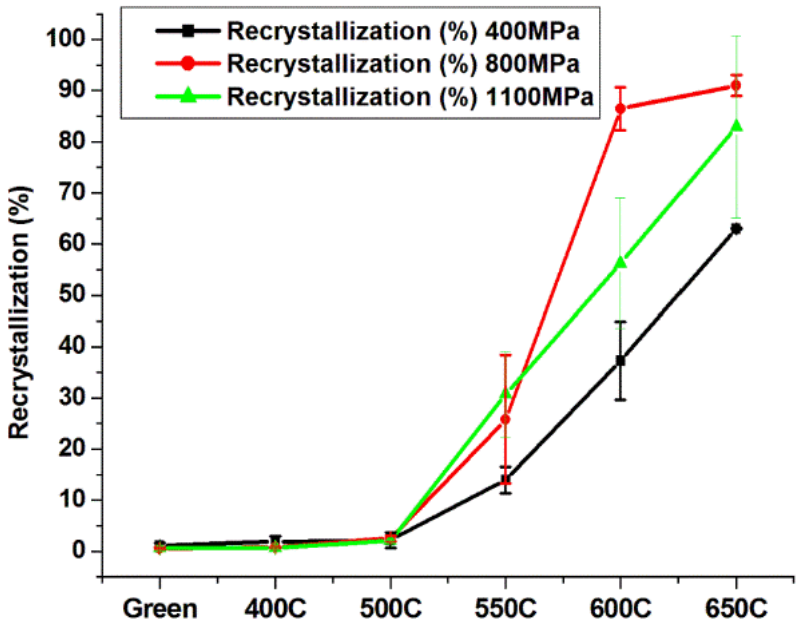

Figure 6.2.2a – Comparison of Recrystallization Percentage at all temperatures and all compaction pressures

For the 650ºC series, even though the recrystallization percentage is always higher, the magnetic behaviour described with the DC tests (see Figure 6.1.2c), experience a slight change corresponding to the smaller difference in recrystallization percentage. The same behaviour is observed for coercivity or hysteresis loss values (section 5.4.2). This can be relate to the fact that the particles show a higher strained state to the ones showed by the particles at 600ºC, see section 5 and Appendix C. There are no substantial grain size differences, so the heat treatment could be affecting the microstructure in other ways that generate strain; creating precipitates in the grain boundaries, degrading the coating and the oxide layers surrounding the iron particles, etcetera. Additionally, once that most of the strain is eliminated the grain boundary could become a more relevant factor to magnetic behaviour, even though these hypotheses are advised to be investigated in future work.

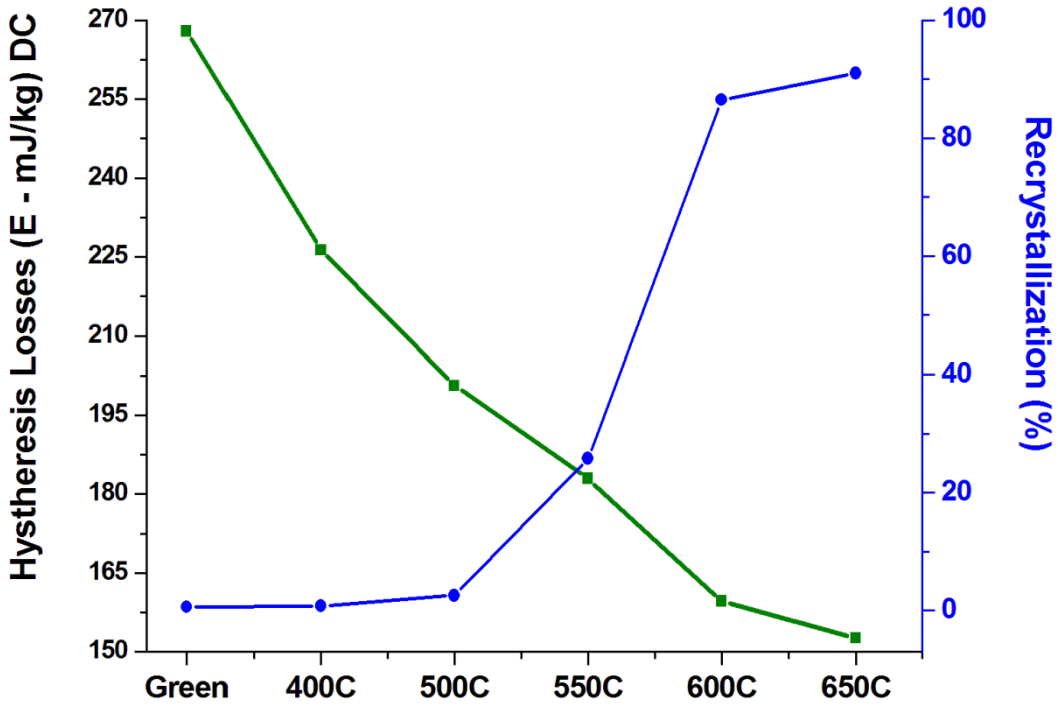

Figure 6.2.2b – Inverse tendency in recrystallization and hysteresis losses values for all conditions

7 Conclusions

- Microstructural evolution and deformation state of SMC components have been evaluated and assessed in respect to their processing conditions (i.e. compaction pressure and annealing temperature).
- Correlation between EBSD and nanoindentation techniques on powder particles allows the verification of the recrystallization state of processed components through the annealing process. Quantification of the amount of deformation can be obtained by comparing the nanohardness values from strained areas and strain-free areas.
- EBSD allows quantitative determination of the evolution of the grain size within the powder particles, as well as the difference in recovery, recrystallization and grain growth stages.
- SMC components show a random distribution in texture all over the microstructure before and after processing. Neither single particles, nor big areas mapped exhibited any preferential orientation, in respect to the compaction direction or the radial direction of the rings.
- Magnetic behaviour of SMC materials is equally related to the microstructure and to the insulating coating. The hysteresis losses can be linked to the microstructural state through EBSD, and this way explain the magnetic performance of the final components, correlating it to the manufacturing process and the deformation stated derived from it

8 Acknowledgments

First I should mention the amazing people in the Materials and Manufacturing Department of Chalmers University of Technology. Special thanks to Lars Nyborg, as head of the department and examiner of this project work; for trusting students coming from abroad in search of inspiration. To all the master and bachelor thesis students who were working in that part of the M building in the past, present and future; thank you for making the perfect environment.

Special thanks to all the supervisors of this master thesis, Uta Klement and Jose Manuel Torralba, for making it possible. To Ann-Cathrin Hellsén, for her constant supervision, guidance and support. Last but not least, Christos Oikonomou, who was really the engine of this investigation, even though I sometimes took his patience to limits beyond imagination. Tack!

To all the people in Höganäs AB, thank you for “dealing” with me both as a student and as a summer worker. I cannot write all the names here, but it would be unfair not mentioning the wonderful people at the Soft Magnetic Composites department: Ye Zhou, Ann-Cathrin Hellsén, Eddie Hedin, Mika Nilson, Jeronimo Lacno, Lars-Olov Pennander, Lars-Åke Larson...and more that I am probably forgetting. Excuse me and thanks to you all.

To Miguel Monclús and Jon-Mikel Molina, who helped me in IMDEA Materials Institute in Madrid. This project owes them a lot, thank you!

Raquel and Carlos de Oro Calderón: you are the best. I have more to thank you both that you would probably ever recognize, but I am delighted that you had crossed my way.

Finally, to all the amazing people I have met last year. LONG LIVE ERASMUS!

And my parents, Antonio and María: thank you for trusting me and made it happen.

Lucía, my sister, moral support, confident, friend and more…Thanks!

9. Index of Figures

10. Bibliography

1. *Soft Magnetic Materials (SMC's).* **H. Shokrollahi, K. Janghorban.** 189, s.l. : Journal of Materials Processing Technology, 2008, Vol. 1.

2. **Höganäs AB.** Soft Magnetic Composites. *Business Area.* [Online] 2015. https://www.hoganas.com/en/business-areas/soft-magnetic-composites/.

3. *Soft Magnetic Composites - Materials and Applications.* **L. O. Hultman, A. G. Jack.** s.l. : IEEE International, 2003.

4. **J. M. Torralba, M. Campos.** Powder Technology. *OCW: Open Course Ware.* [Online] Universidad Carlos III de Madrid, 2008. http://ocw.uc3m.es/ciencia-e-oin/tecnologia-de-polvos.

5. **Lall, C.** *Soft Magnetism, Fundamentals for Powder Metallurgy and Metal Injection Molding.* Princeton, New Jersey : Metal Powder Industries Federation (MPIF), 1992. Monographs in P/M Vol. 2.

6. **Lawley, A.** *Atomization: The production of Metal Powders.* Princeton, New Jersey : Metal Powder Industries Federation (MPIF), 1992. Monographs in P/M. Vol. 1.

7. **German, R. M.** *Powder Metallurgy Science.* Princeton, New Jersey : Metal Powder Industries Federation (MPIF), 1994.

8. **ASM Handbook: Volume 7.** *Powder Metal Technologies and Applications.* Materials Park, OH 44073-0002 : ASM - The Materials Information Society, 1998.

9. **Thümmler, F.** *Introduction to Powder Metallurgy.* s.l. : ed. I.J.a.J.V. Wood, The Institute of Materials, Series on Powder Metallurgy, 1993.

10. **Callister, W. D.** *Materials Science and Engineering, Eight Edition.* s.l. : John Willey Sons, 2011.

11. **Reed-Hill, R. E.** *Physical Metallurgy Principles.* s.l. : Van Nostrand - University, 1964.

12. **Kittel, C.** *Introduction to Solid State Physics - 8th ed.* s.l. : John Willey & Sons, Inc., 2005.

13. **J. C. Anderson, R. D. Rawlings, J. M. Alexander.** *Material Science.* s.l. : Chapman and Hall, 1990.

14. **Hosford, W. F.** *Physical Metallurgy.* s.l. : CRC Press, 2010.

15. **Guy, A. G.** *Elements of Physical Metallurgy.* s.l. : Metallurgy and Materials - ed. A.-W.P. Company, 1974.

16. **Cullity, B. D.** *Introduction to Magnetic Materials.* s.l. : John Willey & Sons, 2009.

17. **Höganäs AB.** SMC Handbook. *Somaloy training PMG.* Höganäs : s.n., 2010.

18. *Soft Magnetic Sintered and Composite Materials.* **Jansson, P.** s.l. : Advanced Materials and Technologies, 2003, Vol. 2A1.

19. **Oikonomou, C.** Surface Characterization of Soft Magnetic Composite Powder and Compacts. Gothenburg : Chalmers University of Technology, 2014.

20. *Soft Magnetic Iron Powder Materials AC Properties and their Application in Electrical Machines.* **L. O. Pennander, A. G. Jack.** s.l. : Euro PM, 2003.

21. *Physical Origin of Losses in Conducting Ferromagnetic Materials.* **Jr., C. D. G.** 8276-8280, s.l. : Journal of Applied Physics, 1982, Vol. 53.

22. **Randle, O.E a. V.** *Introduction to Texture Analysis; Macrotexture, Microstexture and Orientation Mapping.* s.l. : CRC Press, 2009.

23. **Cullity, B. D.** *Elements of X-ray diffraction.* Reading, Mass. : Addison-Wesley, 1978.

24. *Electron Backscatter Diffraction (EBSD) Technique and Material Characterization Examples.* **Tim Maitland, S. S.** s.l. : Scanning Microscopy for Nanotechnology Techniques and Applications, 2007, Vol. XIV.

25. *Processing Aspects of Soft Magnetic Composites.* **Jansson, Patricia.** s.l. : EuroPM200 - Soft Magnetic Materials Workshop, 2000.

26. **Leila Bjerregaard, K. G., Birgit Ottesen, Michael Rückert.** *Metalog Guide.* s.l. : Struers, 2000.

27. **Adam J. Scwartz, M. K., Brent L. Adams, David P. Field.** *Electron Backscatter Diffraction in Material Science.* s.l. : Springer, 2000.

28. **Instruments, Oxford.** *Characterizing local strain variations around crack tips using EBSD mapping.*

29. *A review of Strain Analysis Using Electron Backscatter Diffraction.* **Stuart I. Wright, M.M.N., David P. Field.** 316-319, s.l. : Microscopy and Microanalysis, 2011, Vol. 17.

30. **Fischer-Cripps, A. C.** *Nanoindentation.* New York : Springer, 2002. Mechanical Engineering.

31. **Irene de Diego Calderón, M.J.S., Jon Molina Aldareguia, M. A. Monclús, I. Sabirov.** *Deformation behaviour of high strength multiphase steel and macro- and micro-scales.* s.l. : Materials Science&Engineering, 2014. 611.

32. *Nanoindentation studies of materials.* **Schuh, C. A.** 5, s.l. : Materials Today, 2006, Vol. 9. 32-40.

33. *Measurement of hardness and elastic modulus by instrumented indentation: Advances in understanding and refinements to methodology.* **Oliver, W. C. Pharr, G. M.** s.l. : Journal of Materials Research, 2003, Vol. 19. 3-20.

34. **Hysitron.** Quasistatic Nanoindentation: An Overview. [Online] 2014. https://www.hysitron.com/resources-support/education-training/nanoindentation.

35. *Critical Review of Analysis and Interpretation of Nanoindentation test data.* **Fischer-Cripps, A. C.** s.l. : Surface & Coatings Technology, 2005, Vol. 200. 4153-4165.

36. *An experimental Investigation of the Deformed Zone Associated with Indentation Hardness Impressions.* **L. E. Samuels, T. O. Mulhearn.** s.l. : Journal of the Mechanics and Physics of Solids, 1956, Vol. 5. 125-134.

37. *The theory of wedge indentation of ductile materials.* **R. Hill, E. H. Lee, S. J. Tupper.** s.l. : Proc. R. Soc. London, 1945, Vol. A188. 273-289.

38. **Fischer-Cripps, A. C.** *Introduction to Contact Mechanics.* s.l. : Springer, 2007.

39. *An improved technique for determining hardness and elastic modulus using load and displacement sensing indentation.* **W. C. Oliver, G. M. Pharr.** 06, s.l. : Journal of Materials Research, 1992, Vol. 7. 1564-1583.

40. *Determination of elastoplastic Properties by Instrumented Sharp Indentation.* **A. E. Giannakopoulos, S. S.** 10, s.l. : Scripta Materialia, 1998, Vol. 40. 1191-1198.

41. *Measurement of Residual Stresses Using Nanoindentation Method.* **Li-Na Zhu, B.-S.X., Hai-Dou Wang, Cheng-Biao Wang.** s.l. : Solid State and Material Sciences, 2014, Vol. 40. 77-89.

42. *The response of Solids to Elastic/Plastic Indentation. I. Stresses and Residual Stresses.* **S. S. Chiang, D. B. M., A. G. Evans.** s.l. : Journal of Applied Physics, 1982, Vol. 53.

43. **Brockhaus.** Brockhaus Measurements. [Online] 2011. http://www.brockhaus.com/en/brockhaus/.

44. *Misorientation Mapping for Visualization of Plastic Deformation via Electron Back-scaterred Diffraction.* **L. N. Brewer, M. A. O., L. M. Young, T. M. Angeliu.** s.l. : Microscopy and Microanalysis, 2006, Vol. 12. 85-91.

45. *The effect of compaccction parameters and the particle size on magnetic properties of iron-based alloys used in soft magnetic composites.* **H. Shkrolahi, K. J.** s.l. : Materials Science and Engineering, 2006, Vol. 134. 41-43.

46. *New lines of investigation on the effects of processing conditions on soft magnetic composite materials behaviour for electromagnetic applications.* **Marco Actis Grande, A. C., P. Ferraris, R. Bidulsky.** s.l. : IEEE, 2010. 986-991.

Appendix A: Analysis of SMC and of ABC Particles

Loose SMC and ABC powder particles were prepared in a similar way to the description in Section 3, mixing the powder with Polyfast Resin, preparing a sample which was then polish on different steps until 1µm, and then a final OPU so a mirror-like surface was achieved.

Figures A.i to A.iii show four particles per type of powder and their qualitatively differences towards EBSD extracted information. All maps were taken with 0,5µm step-size, Magnification 1000x and 20kV gun voltage, as SEM-EBSD parameters.

SMC	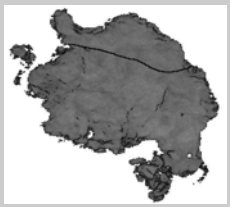	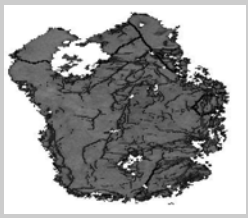	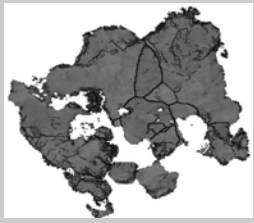	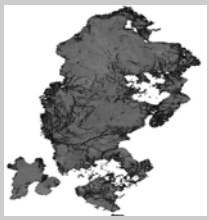
ABC	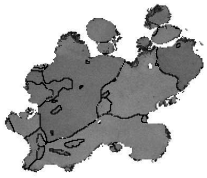	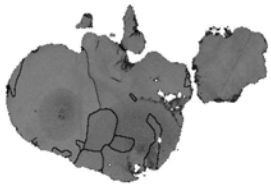		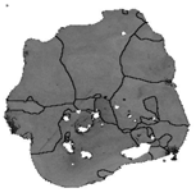

Figure A.i – LAB of SMC and ABC powder particles

SMC	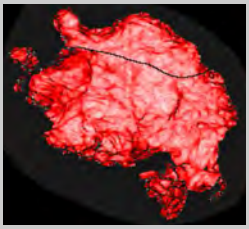	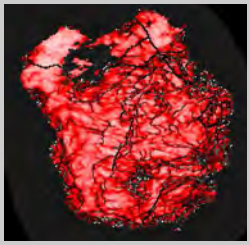	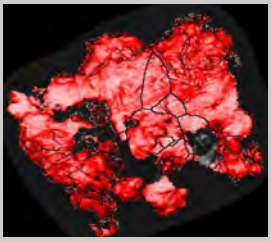	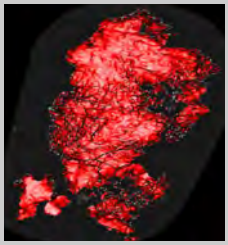
ABC	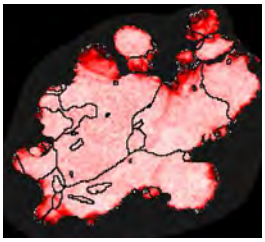	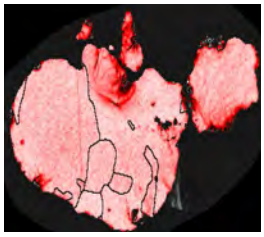		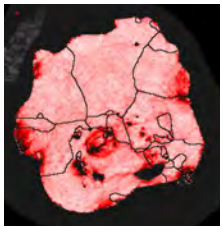

Figure A.ii – Local Misorientation Factor of SMC and ABC powder particles

SMC	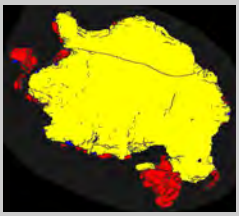	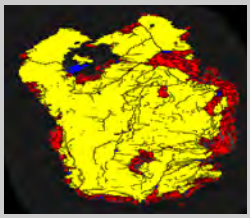	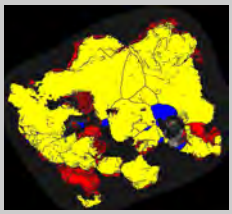	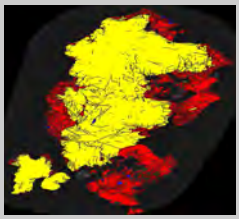
ABC	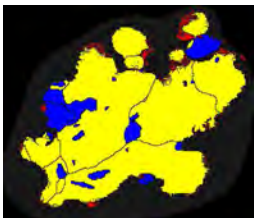	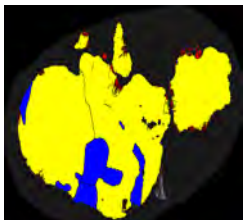	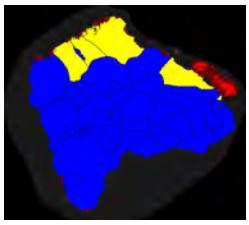	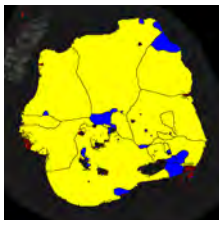

Figure A.iii – Recrystallization and Low Angle Boundaries of SMC and ABC powder particles

From a qualitative point of view, SMC Particles look more strained and deformed that ABC particles. On these last particles grains are also smaller, some of them recrystallized, while in SMC particles this percentage is quite low.

Appendix B: Numerical values

I. Mechanical Test: TRS values

Order by Temperature			Order by Pressure		
	Mean Values	Dev		400MPa	Dev
Green - 400MPa	11,98	0,33	**Green**	11,98	0,33
Green - 800MPa	18,87	0,64	**400ºC**	64,89	0,08
Green - 1100MPa	19,01	0,37	**500ºC**	67,05	0,01
			550ºC	69,58	0,11
400ºC - 400MPa	64,89	0,08	**600ºC**	57,62	1,63
400ºC - 800MPa	33,06	1,64	**650ºC**	59,50	5,81
400ºC - 1100MPa	25,46	0,46			
				800MPa	
500ºC - 400MPa	67,05	0,01	**Green**	18,87	0,64
500ºC - 800MPa	39,81	1,33	**400ºC**	33,06	1,64
500ºC - 1100MPa	36,20	2,05	**500ºC**	39,81	1,33
			550ºC	39,55	1,46
550ºC - 400MPa	69,58	0,11	**600ºC**	40,37	0,11
550ºC - 800MPa	39,55	1,46	**650ºC**	36,20	0,04
550ºC - 1100MPa	33,52	2,00			
				1100MPa	
600ºC - 400MPa	57,62	1,63	**Green**	19,01	0,37
600ºC - 800MPa	40,37	0,11	**400ºC**	25,46	0,46
600ºC - 1100MPa	33,94	1,26	**500ºC**	36,20	2,05
			550ºC	33,52	2,00
650ºC - 400MPa	59,50	5,81	**600ºC**	33,94	1,26
650ºC - 800MPa	36,20	0,04	**650ºC**	34,41	2,05
650ºC - 1100MPa	34,41	2,05			

Figure B.I – TRS values

II. Magnetic tests graphics and results

II.i DC tests

(All taken at 10kA/m)

		400MPa			800MPa			1100MPa		
Green	Bmax-DCH (T)	1,13	(+/-)	0,01	1,38	(+/-)	0,00	1,41	(+/-)	0,00
	Hc [A/m]	407,08	(+/-)	1,37	384,28	(+/-)	1,16	373,02	(+/-)	1,50
	μ_{max}	177,42	(+/-)	6.91	234,14	(+/-)	1.58	236,35	(+/-)	0,25
400C	Bmax-DCH (T)	1,11	(+/-)	0,02	1,37	(+/-)	0,00	1,41	(+/-)	0,01
	Hc [A/m]	364,76	(+/-)	3,06	327,20	(+/-)	0,62	311,84	(+/-)	2,09
	μ_{max}	198,27	(+/-)	13,94	255,36	(+/-)	1,11	248,19	(+/-)	10,39
500C	Bmax-DCH (T)	1,10	(+/-)	0,00	1,40	(+/-)	0,00	1,44	(+/-)	0,00
	Hc [A/m]	404,62	(+/-)	1,88	269,11	(+/-)	2,04	255,49	(+/-)	0,47
	μ_{max}	215,54	(+/-)	0,48	284,75	(+/-)	1,23	285,77	(+/-)	2,12
550C	Bmax-DCH (T)	1,09	(+/-)	0,00	1,42	(+/-)	0,00	1,45	(+/-)	0,00
	Hc [A/m]	337,43	(+/-)	45,24	234,03	(+/-)	1,61	220,23	(+/-)	1,66
	μ_{max}	215,79	(+/-)	1,16	308,68	(+/-)	3,65	305,54	(+/-)	0,65
600C	Bmax-DCH (T)	1,00	(+/-)	0,00	1,40	(+/-)	0,00	1,45	(+/-)	0,00
	Hc [A/m]	277,38	(+/-)	2,45	192,41	(+/-)	0,55	185,45	(+/-)	0,67
	μ_{max}	168,54	(+/-)	1,07	313,55	(+/-)	0,76	318,96	(+/-)	0,43
650C	Bmax-DCH (T)	0,98	(+/-)	0,00	1,39	(+/-)	0,00	1,43	(+/-)	0,00
	Hc [A/m]	246,01	(+/-)	5,53	184,32	(+/-)	0,53	176,51	(+/-)	4,25
	μ_{max}	169,14	(+/-)	2,61	317,65	(+/-)	1,35	318,25	(+/-)	1,71

Figure B.II.i – Magnetic results extracted from DC tests

II.ii Resistivity and Conductivity values

(Sorted by temperatures including deviation per set of measurements)

	Resistivity [µOhm*m]	Dev. Res.	Conductivity [S/m]	Dev. Conduct.
400MPa - Green	41795	10771	25	6
800MPa - Green	9462	1128	106	12
1100MPa - Green	104102	20702	9	2
400MPa – 400C	3160	29	316	2
800MPa - 400C	30281	3424	33	3
1100MPa - 400C	62695	10044	16	2
400MPa - 500C	1327	40	754	23
800MPa - 500C	8931	297	112	3
1100MPa - 500C	14468	454	69	2
400MPa - 550C	95	31	11118	3135
800MPa - 550C	214	58	4901	1287
1100MPa - 550C	300	63	3428	727
400MPa - 600C	6	0	166105	2004
800MPa - 600C	6	0	154553	12919
1100MPa - 600C	8	0	115970	2202
400MPa - 650C	1	0	769431	40134
800MPa - 650C	1	0	521758	64085
1100MPa – 650C	2	0	402590	33641

Figure B.II.ii – Resistivity and Conductivity values

II.iv AC losses linear fit over frequency

A linear fit per temperature has been performed so the two essential components of the losses can be distinguished. The constant value (at the intercept with the y-axis) is identified as the Hysteresis Losses, while the increasing linear behaviour is related with the Eddy Current Losses. This shows a quadratic dependency to the frequency, as explained in section 2.4.

- **Rings compacted at 400MPa**

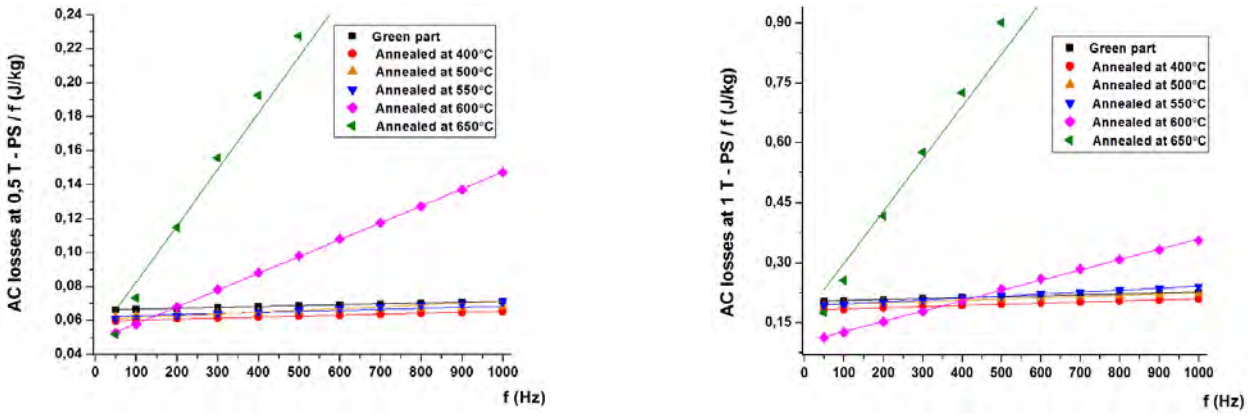

Figure B.II.iv.a – Energy losses representation over frequency for AC test at 0.5T and 1T (400MPa)

- **Rings compacted at 800MPa and 1100MPa**

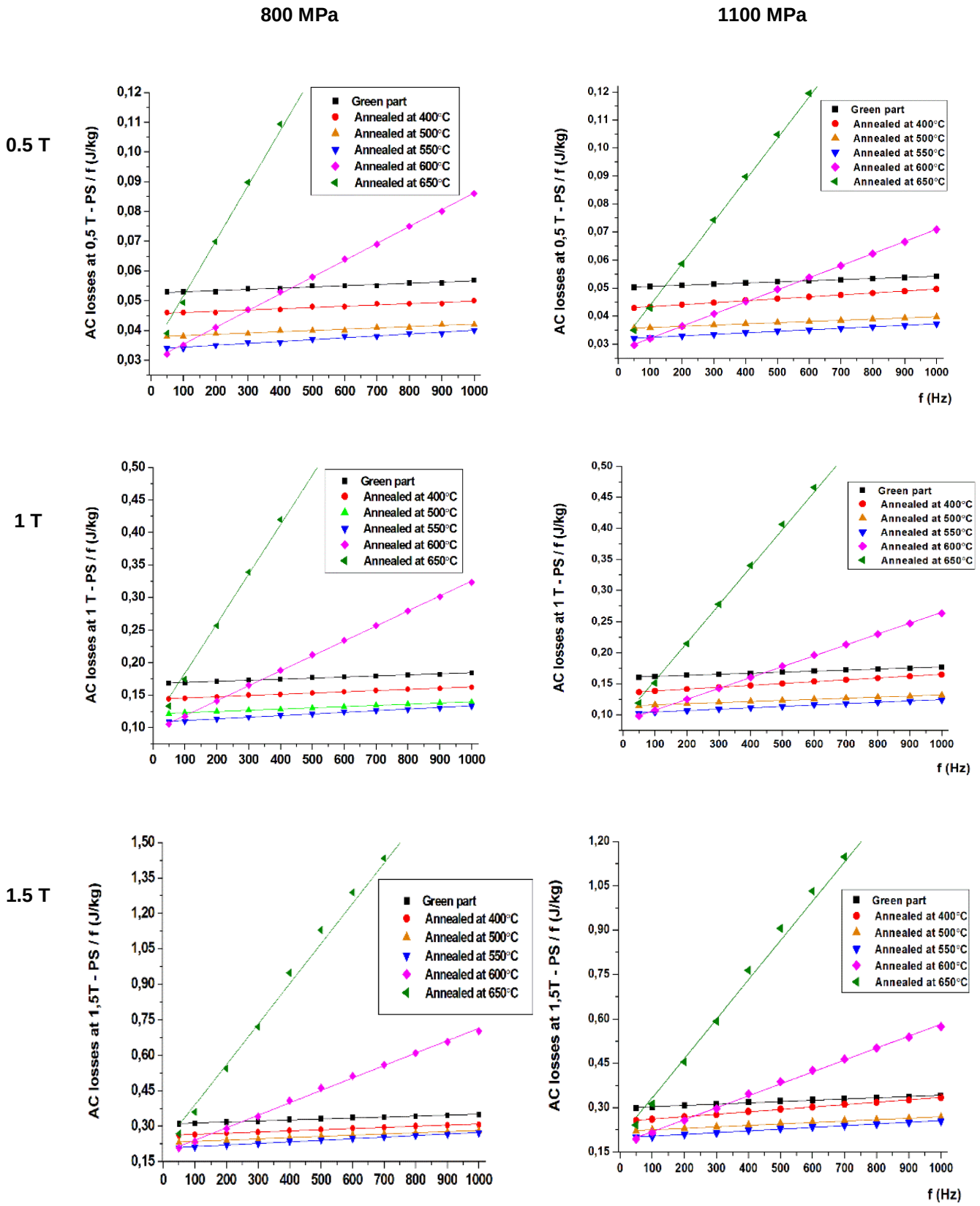

Figure B.II.iv.b – Energy losses representation over frequency for AC test at 0,5T, 1T and 1,5T (800MPa and 1100MPa)

Appendix C

I. Particles in Components compacted at 400MPa

Low Angle Boundaries (LAB) and High Angle Boundaries (HAB)

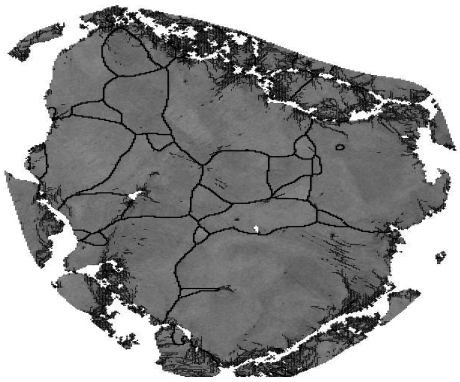

GREEN

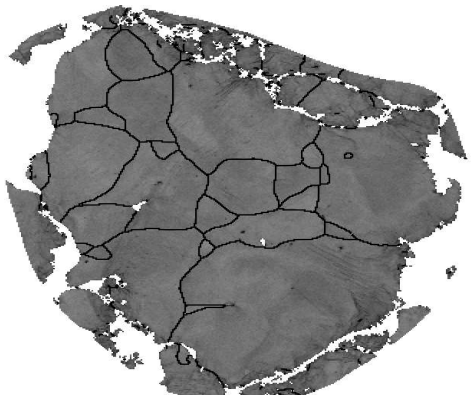

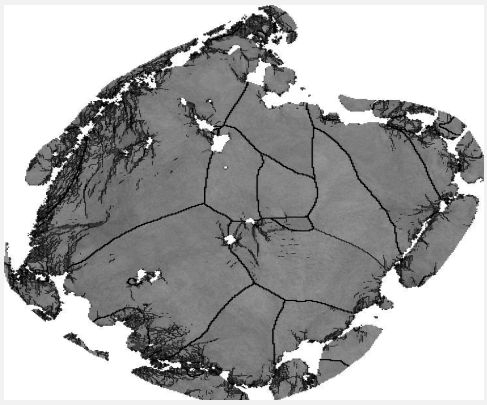

400C

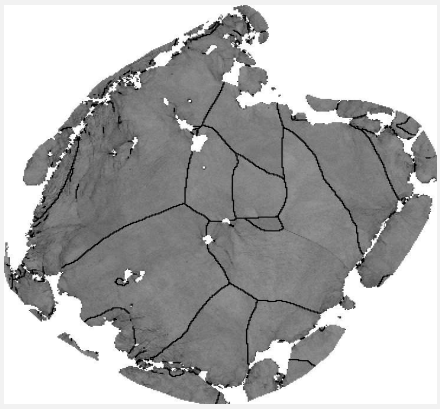

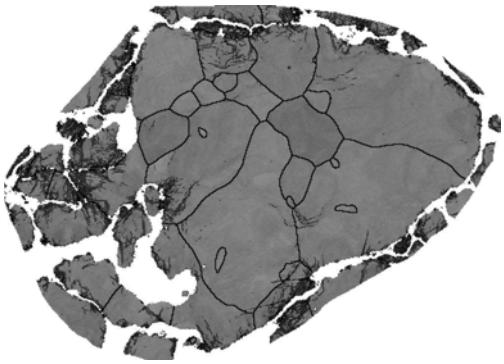

500C

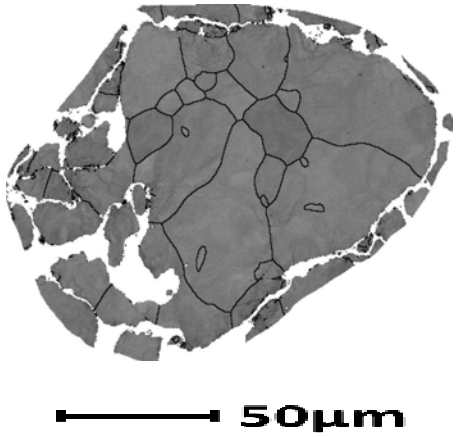

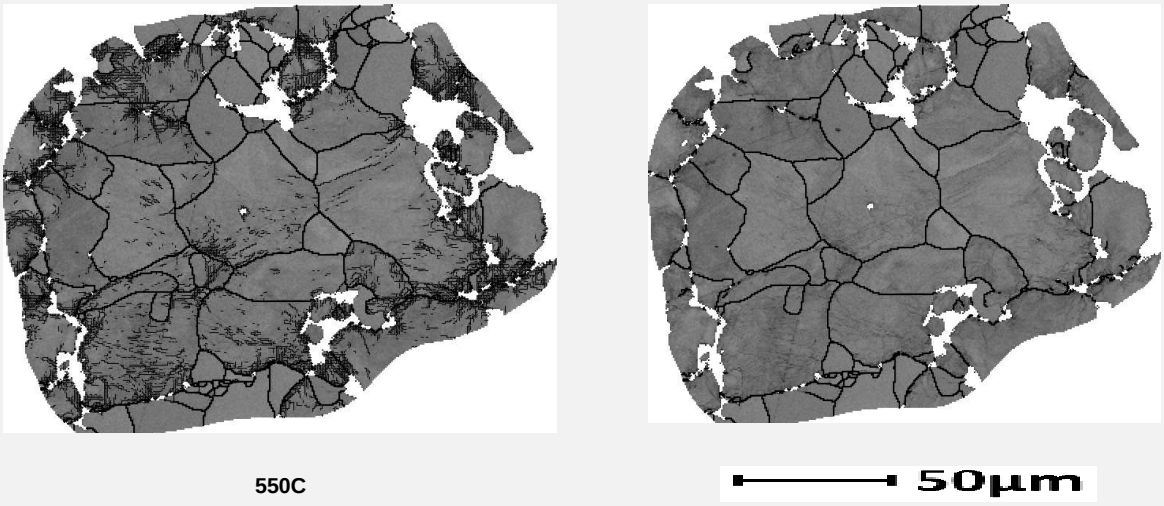

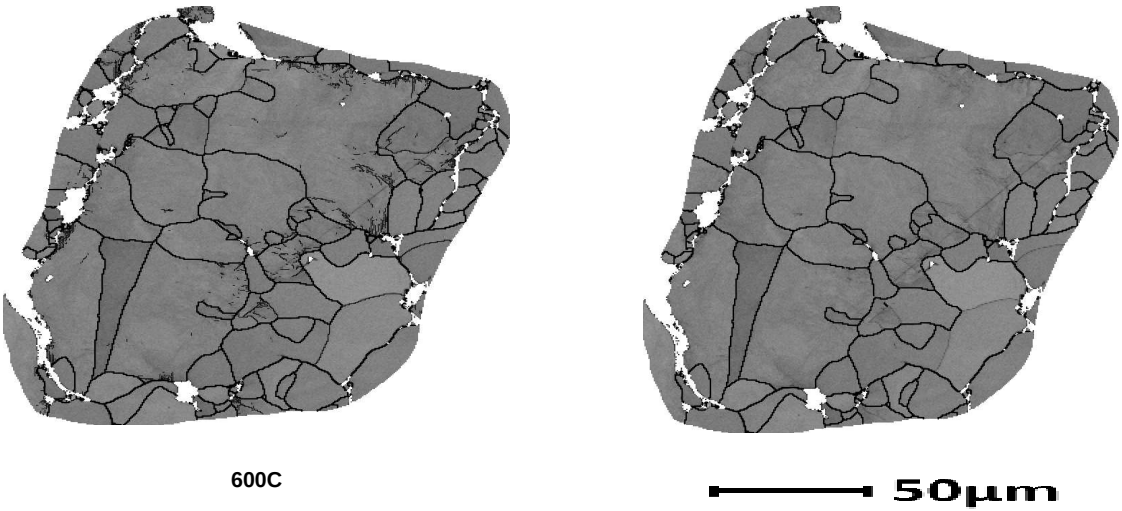

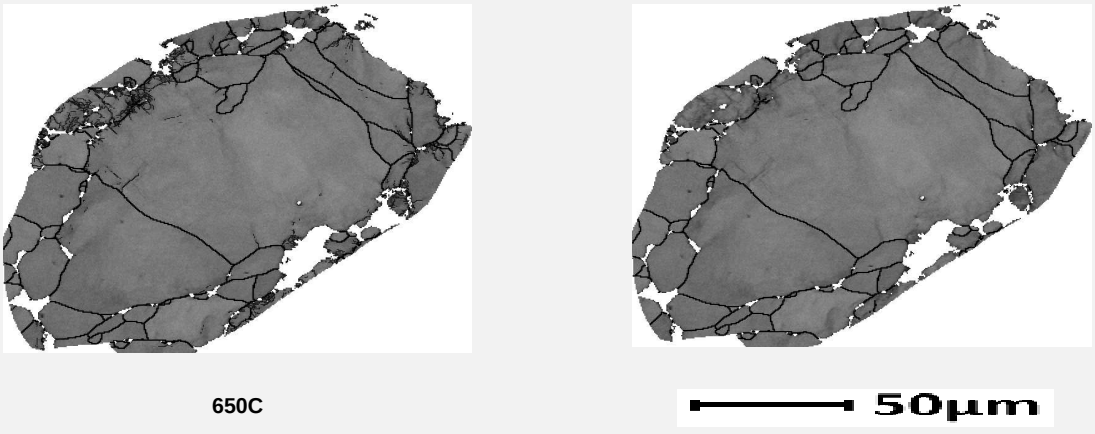

Figure C.i – LAB and HAB of particles of components compacted at 400MPa

Recrystallization Factor

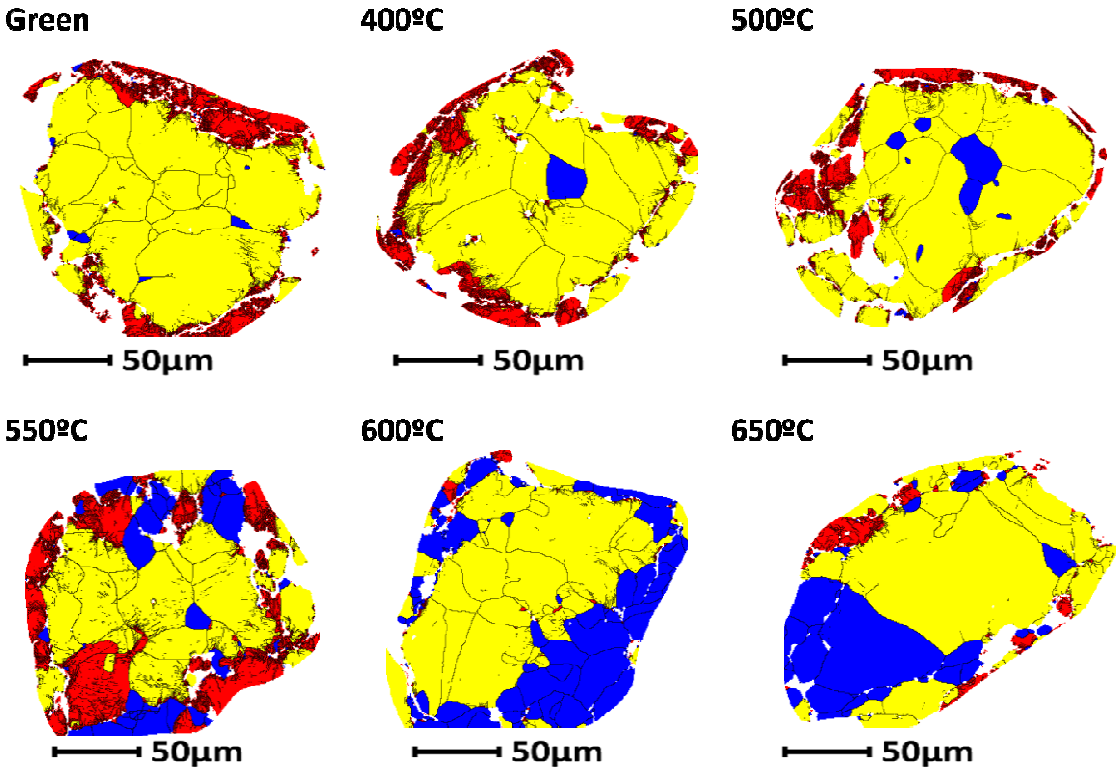

Figure C.ii – Recrytallization Factor maps of particles in components compacted at 400MPa

Local Misorientation Factor

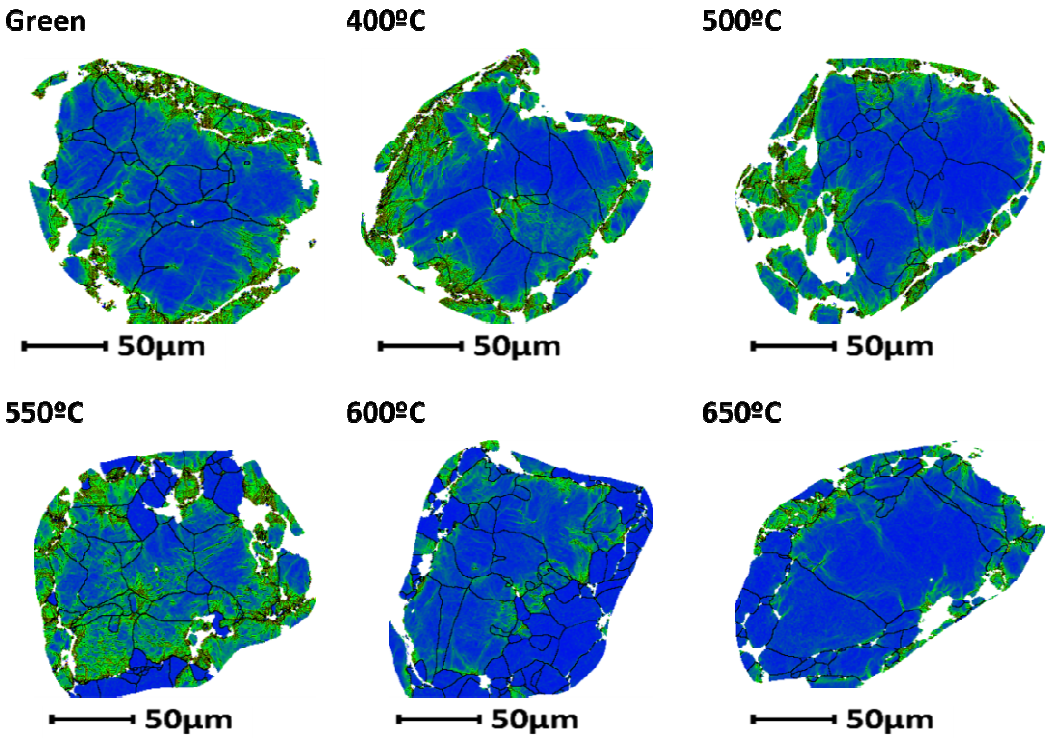

Figure C.iii – Local misorientation maps of particles in components compacted at 400MPa

IPF maps

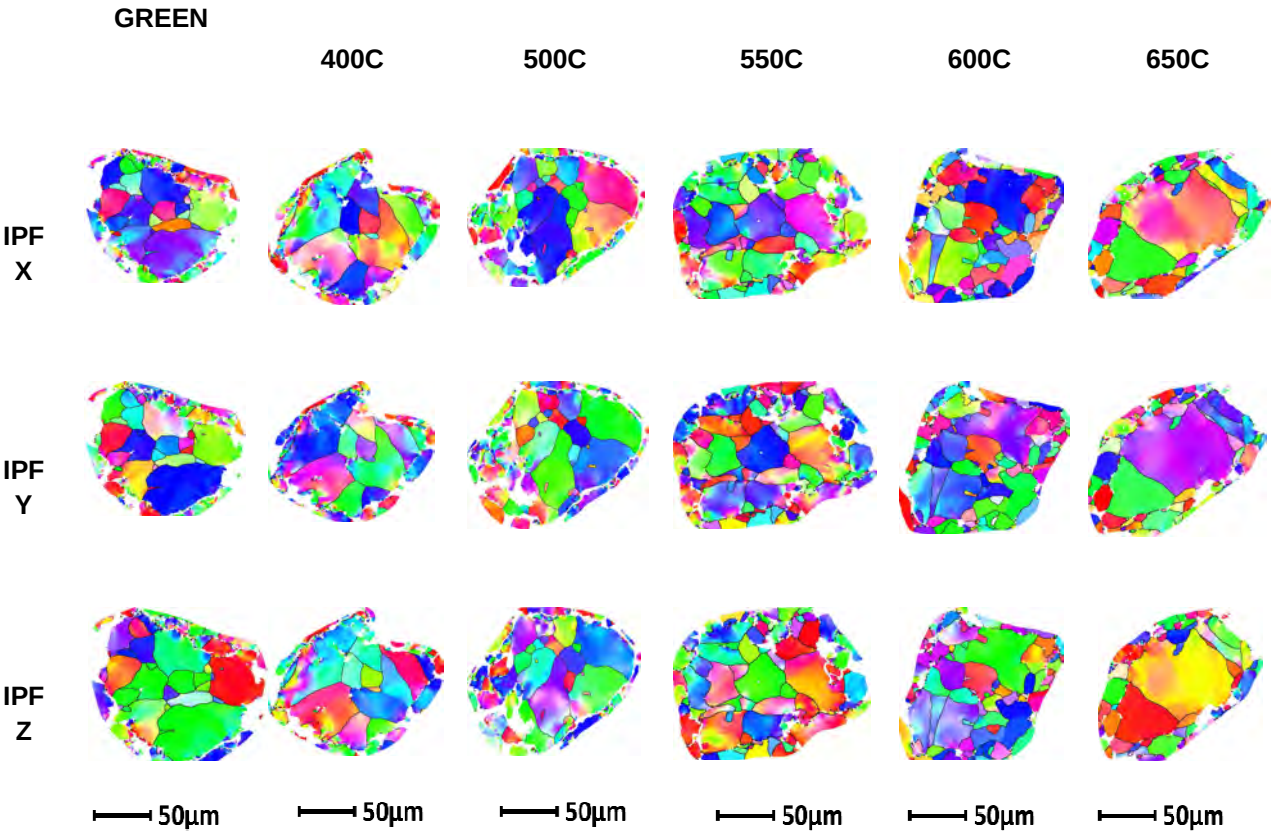

Figure C.iv – IPF coulouring maps of particles in components compacted at 400MPa

II. Particles in Components compacted at 1100MPa

Low Angle Boundaries (LAB) and High Angle Boundaries (HAB)

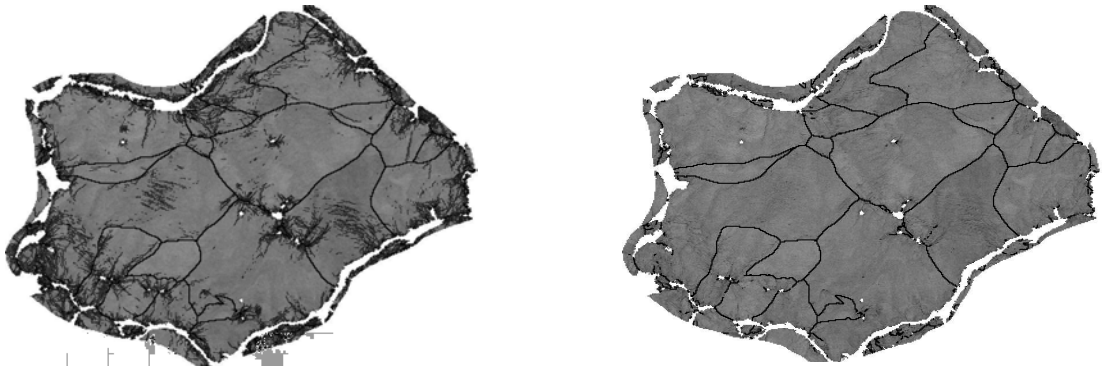

GREEN

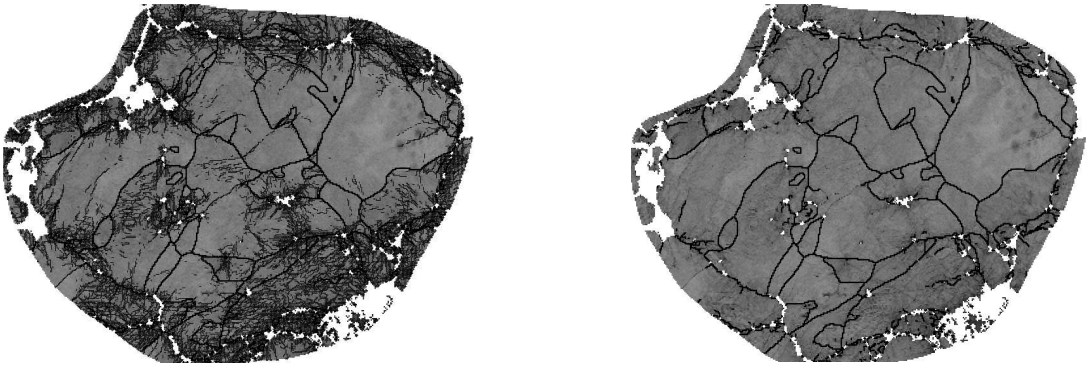

400C

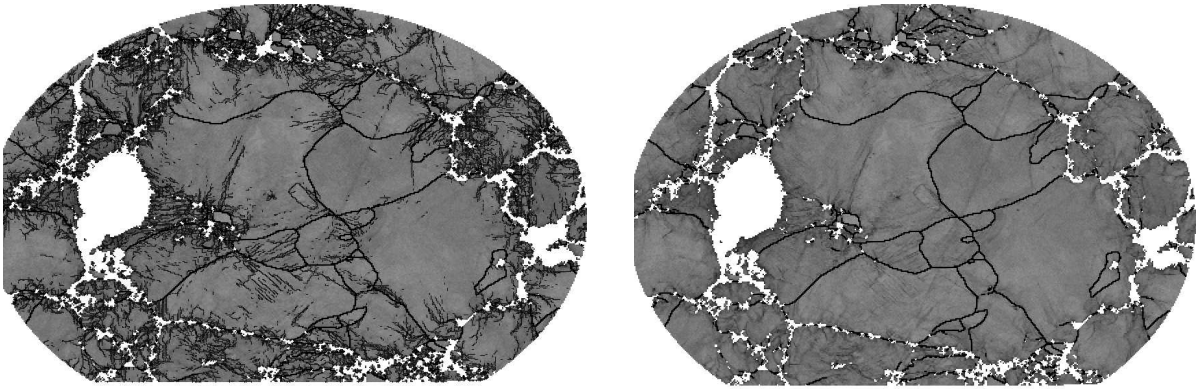

500C

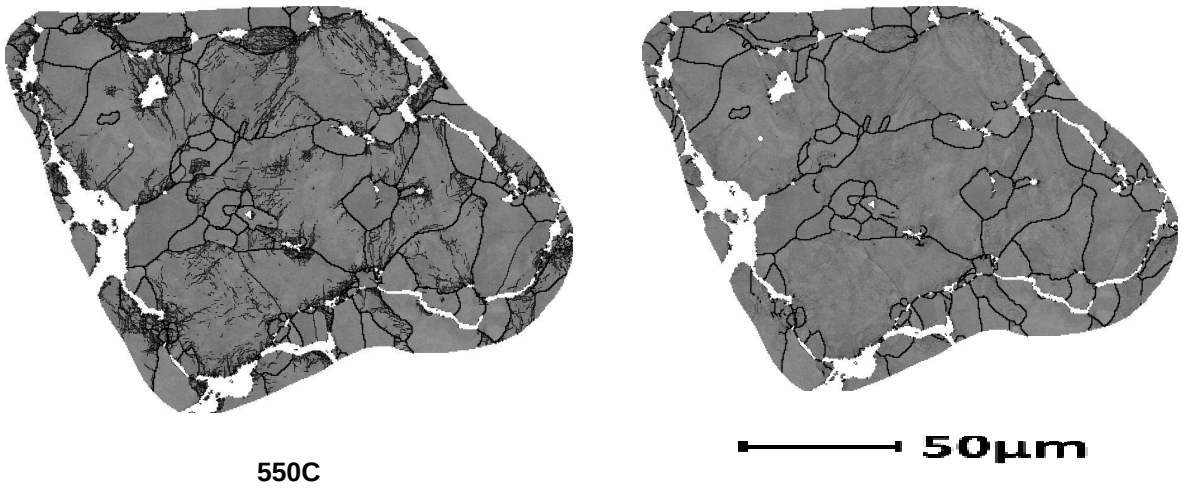

550C

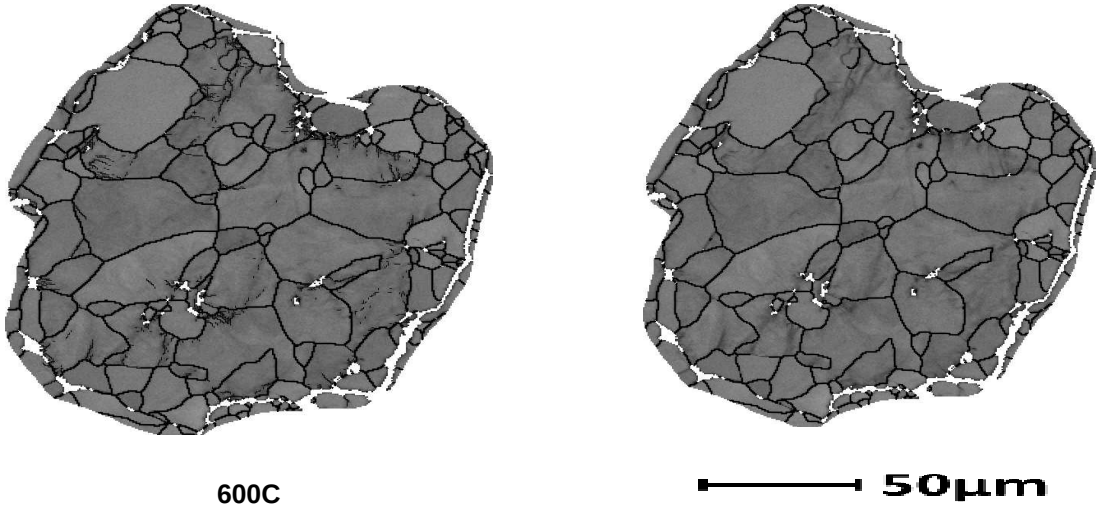

600C

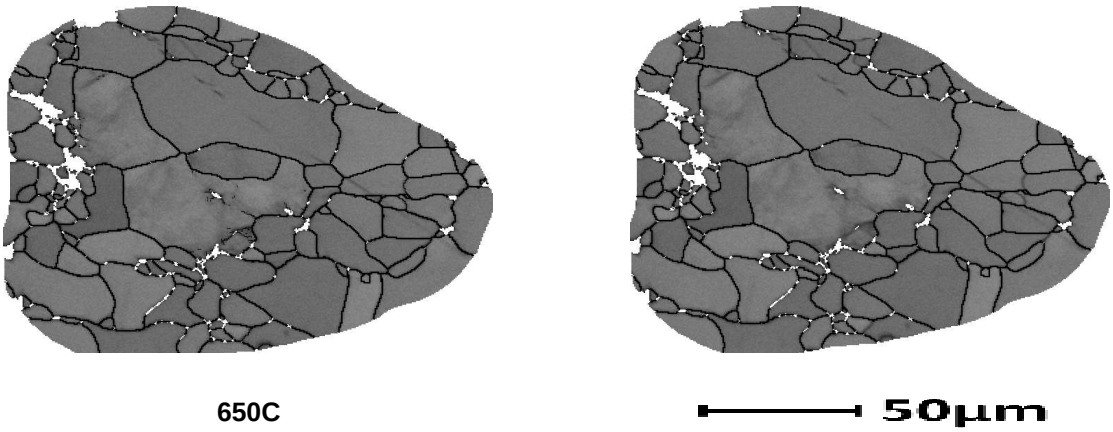

650C

Figure C.v – LAB and HAB of particles of components compacted at 1100MPa

Recrystallization Factor

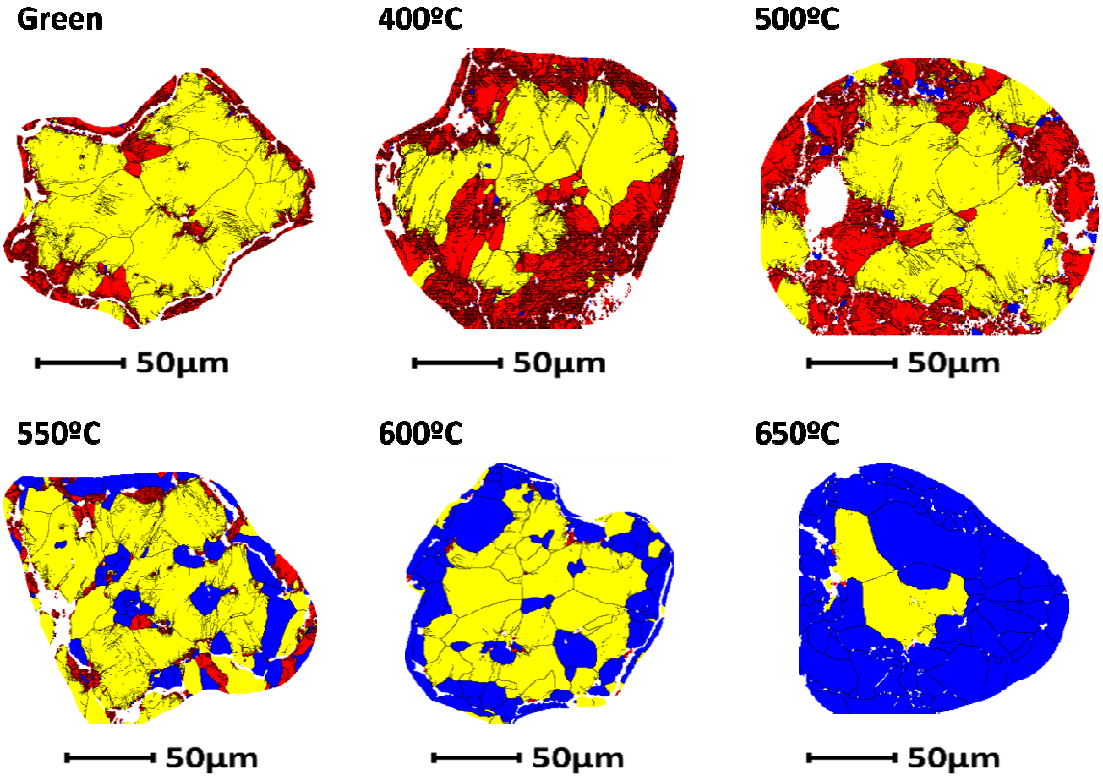

Figure C.vi – Recrystallization factor maps of particles in components compacted at 1100MPa

Local Misorientation Factor

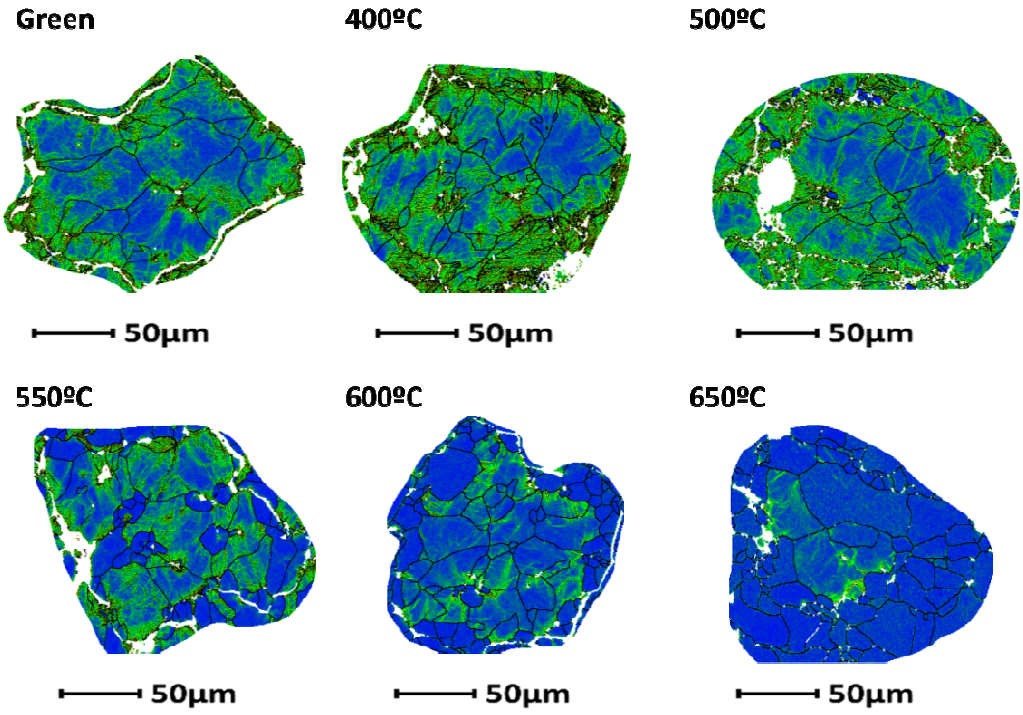

Figure C.vii – Local misorientation maps of particles in components compacted at 1100MPa

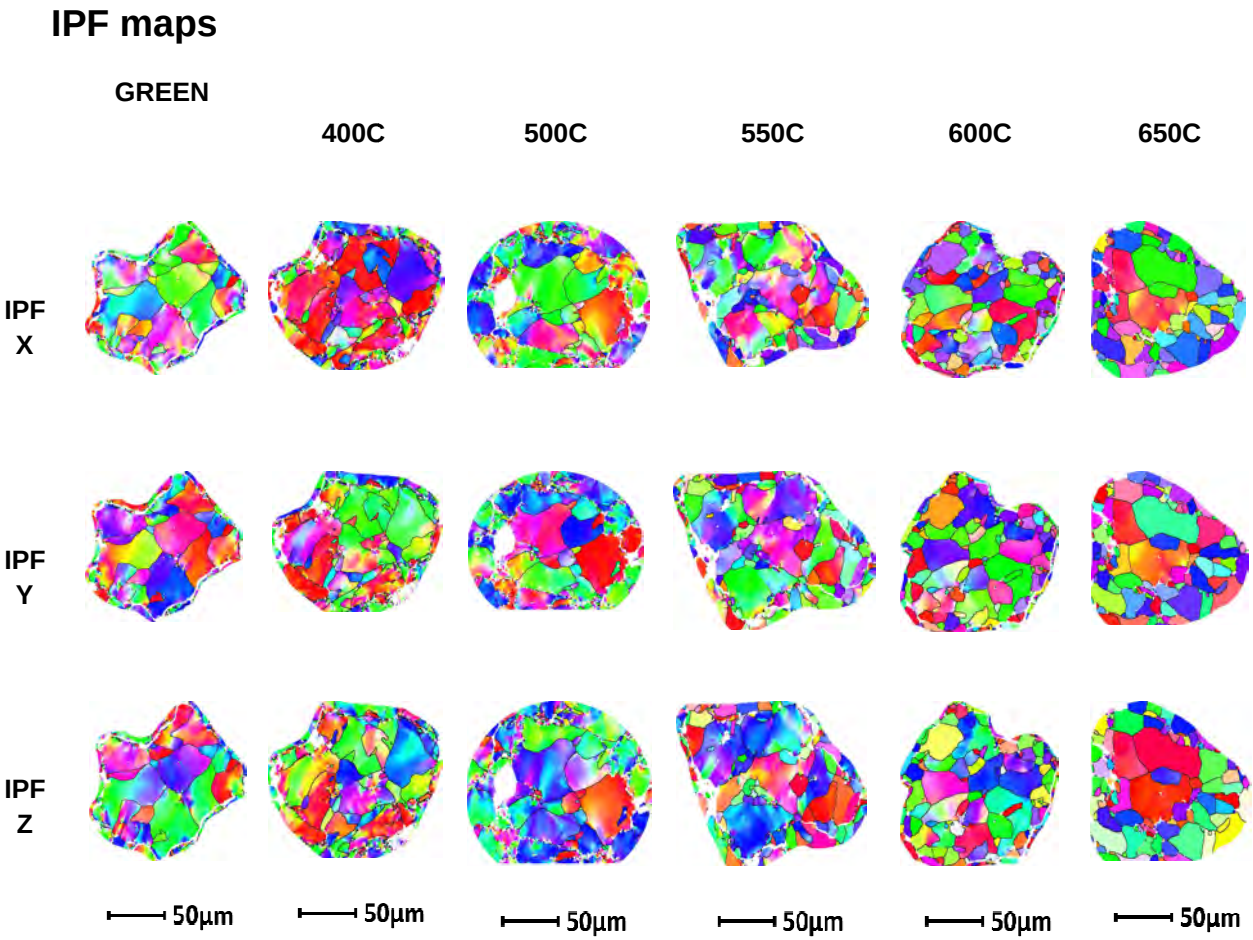

Figure C.viii – IPF coulouring maps of particles in components compacted at 1100MPa

III. Analysis of Big Areas on the Cross Section of Final Components compacted at 400MPa

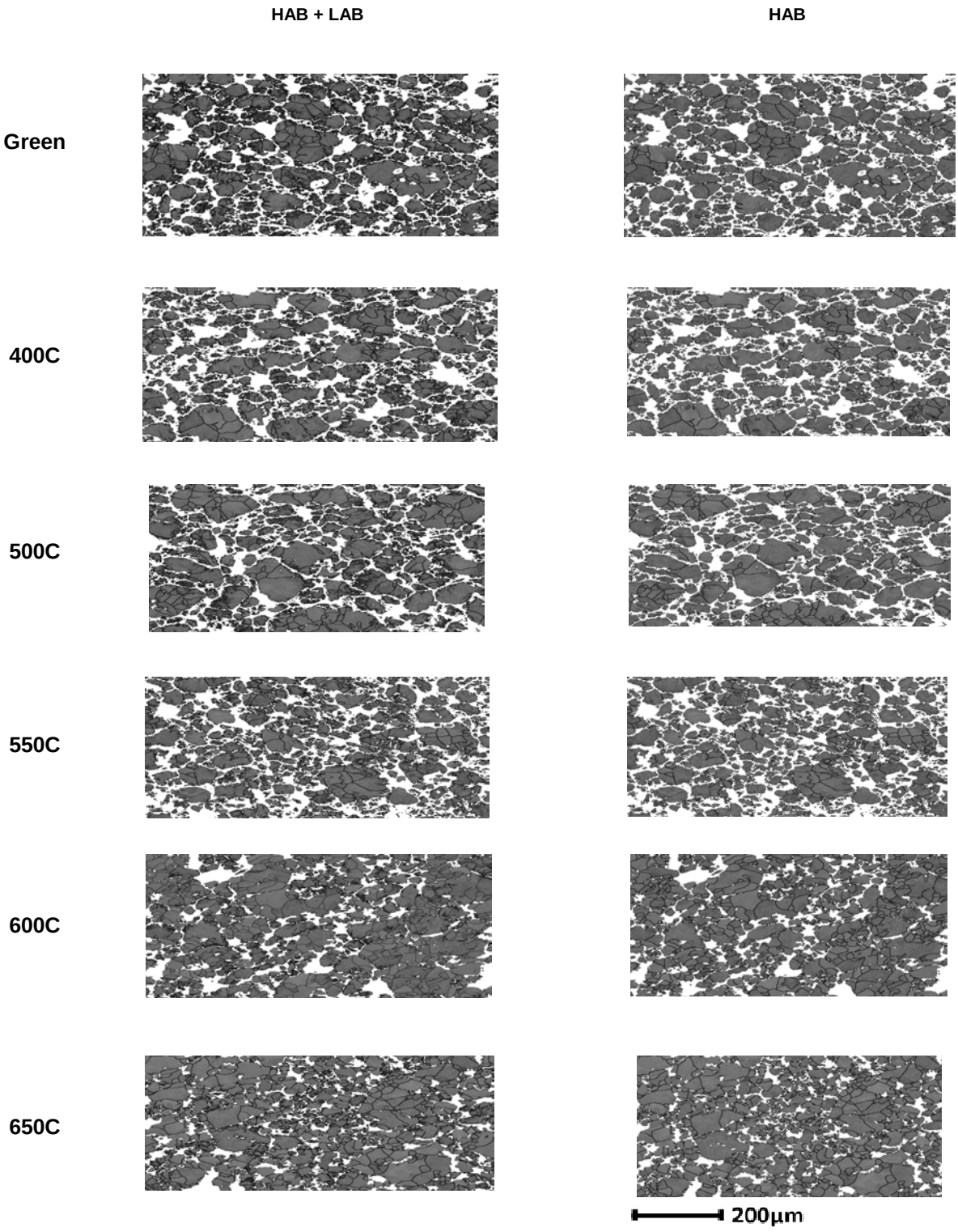

Figure C.ix – LAB and HAB of larger areas of components compacted at 400MPa

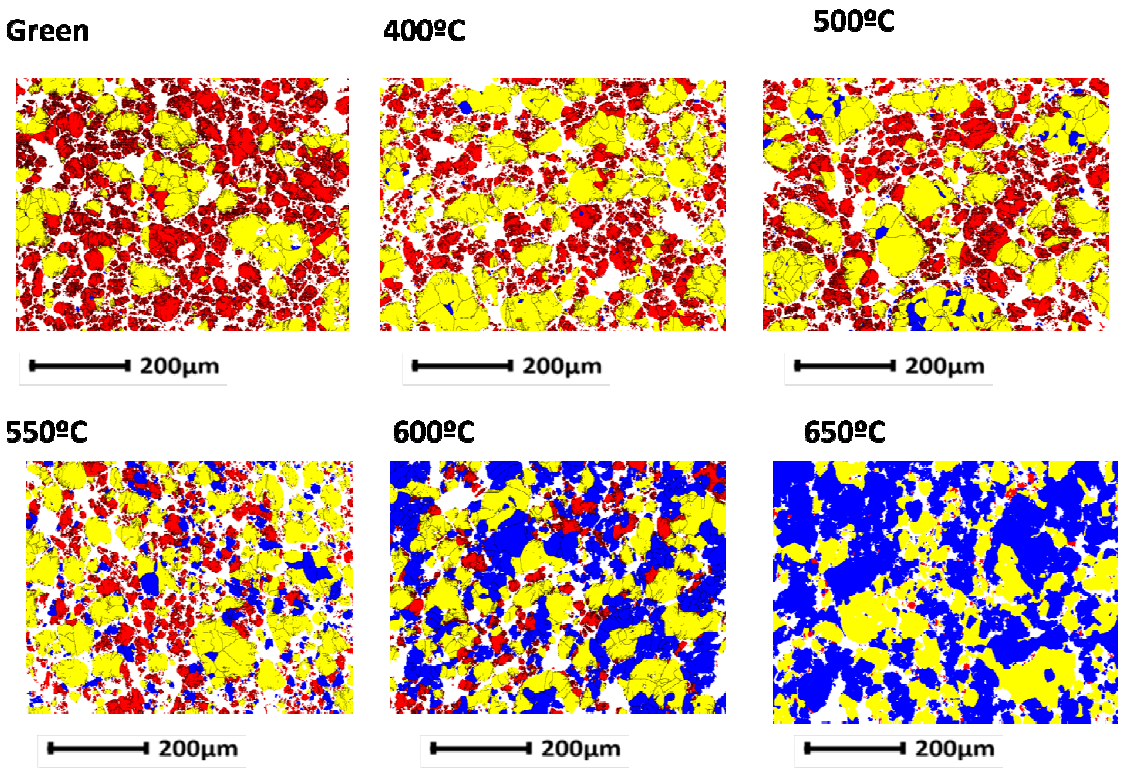

Figure C.x – Recrystallization factor maps of big areas in components compacted at 400MPa

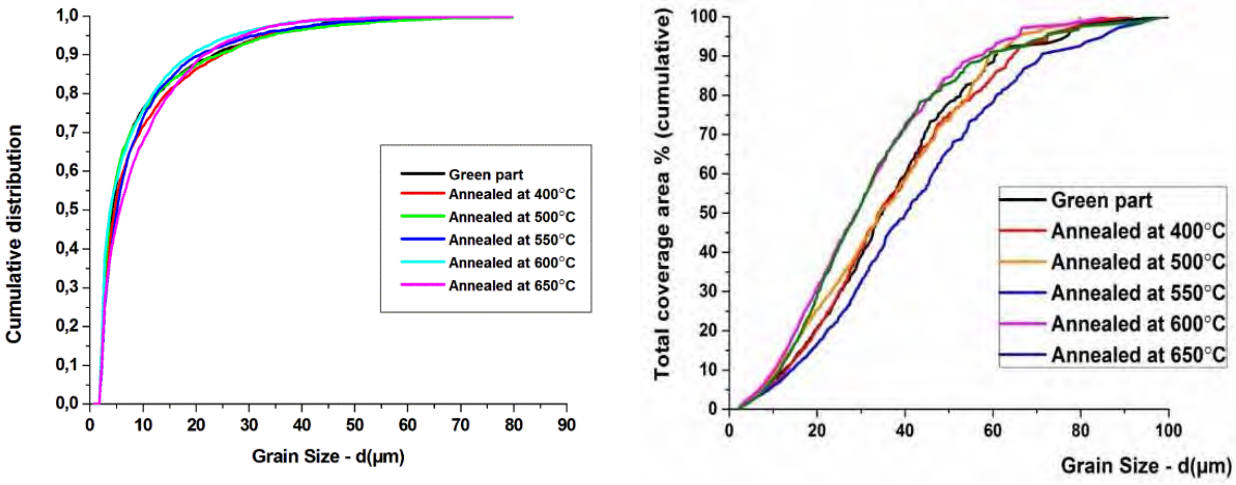

Figure C.xi – Grain size analysis over cumulative probability plots *(left)* and area coverage plots *(right)* of bigger areas of components compacted at 400MPa

400MPa	Green	400C	500C	550C	600C	650C
Mean	4,89	7,85	9,35	9,27	8,13	9,61
Median	4,65	5,17	4,37	5,53	4,37	6,28
Max	111,85	91,91	85,12	98,73	64,32	81,34

Figure C.xii – Mean, median and maximum values of big maps of components compacted at 400MPa

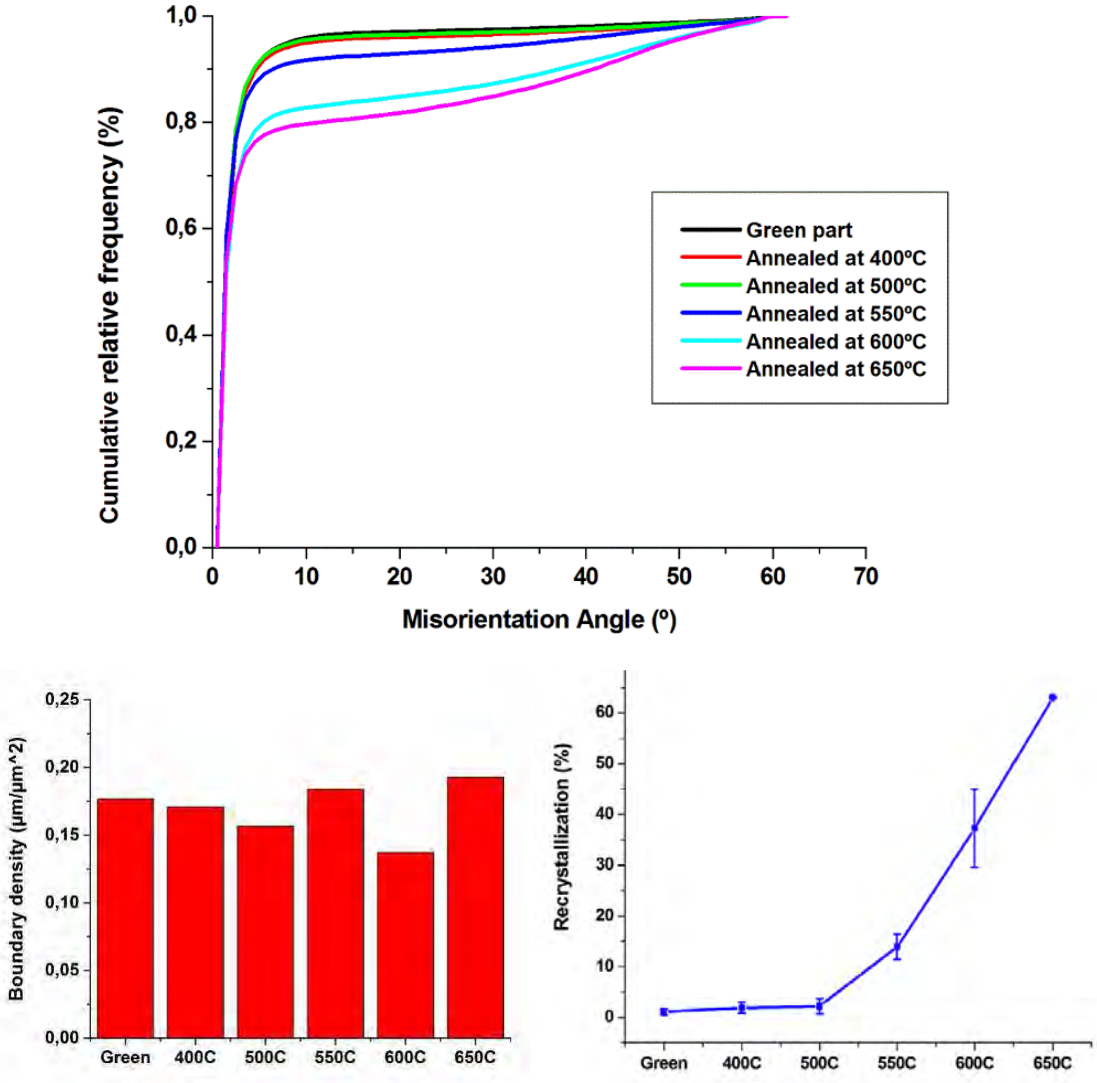

Figure C.xiii – Misorientation angle cumulative plot *(upper)*, boundary parameter *(lower – left)* and recrystallization percentage *(lower – right)* of components compacted at 400MPa

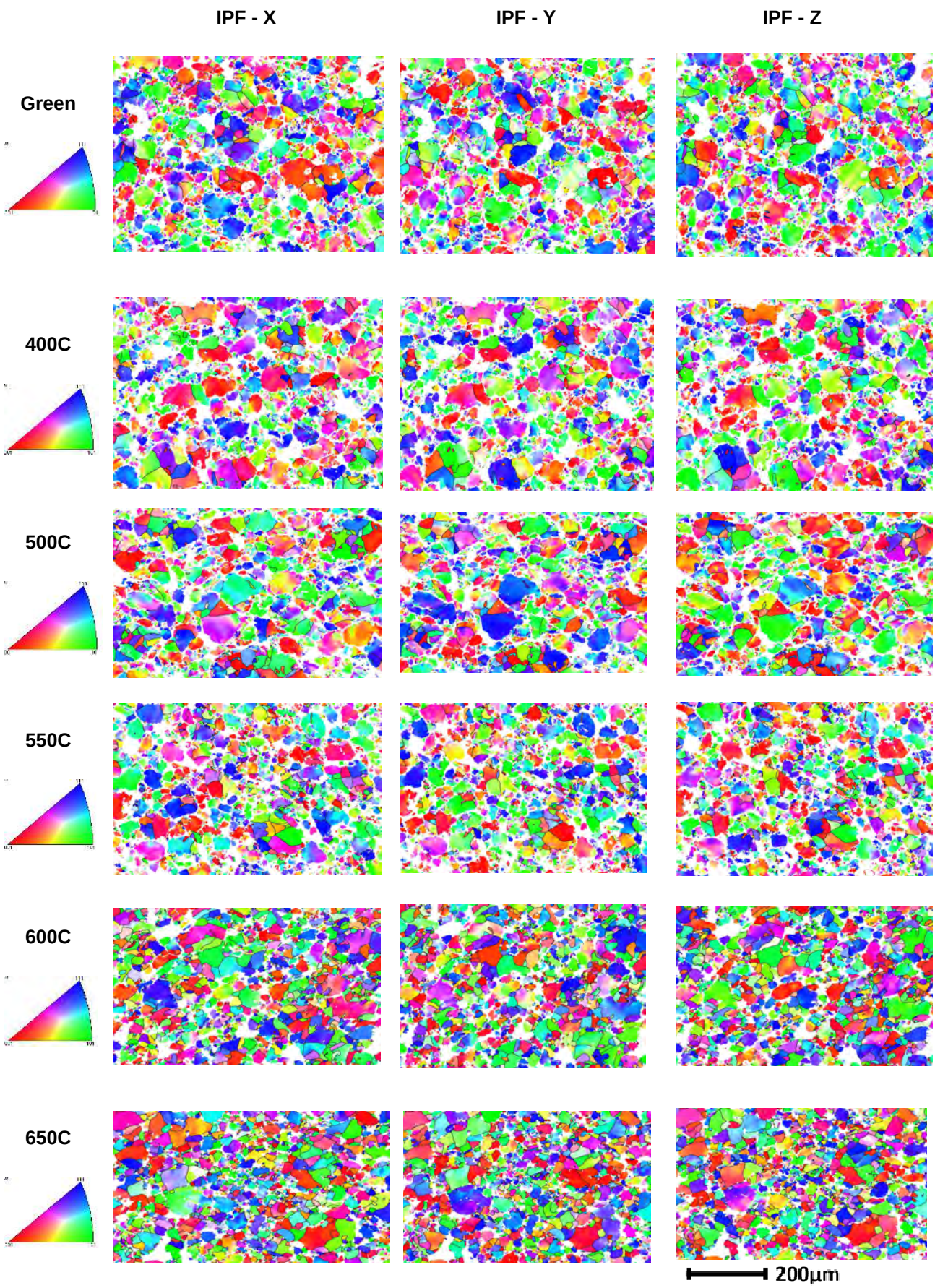

Figure C.xiv – IPF couloring maps *(above)* and IPF *(next page)* of big areas of components compacted at 400MPa

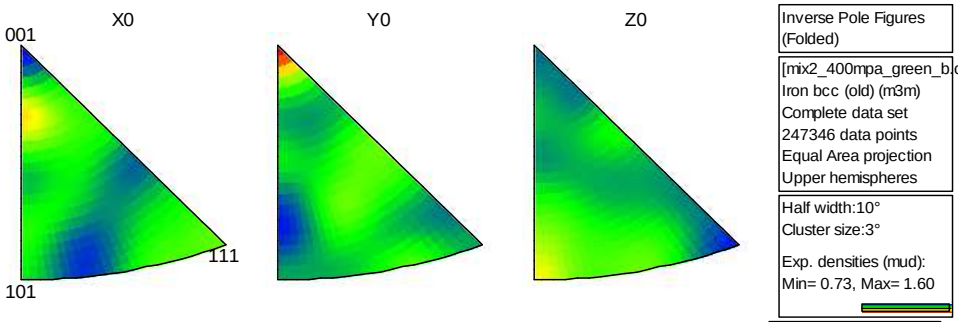

GREEN

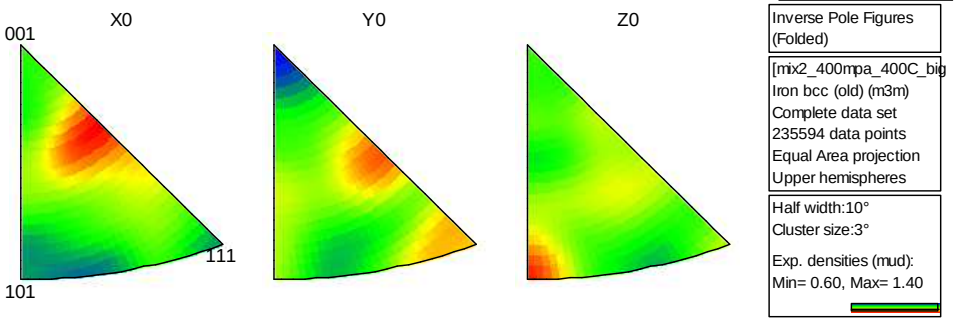

400C

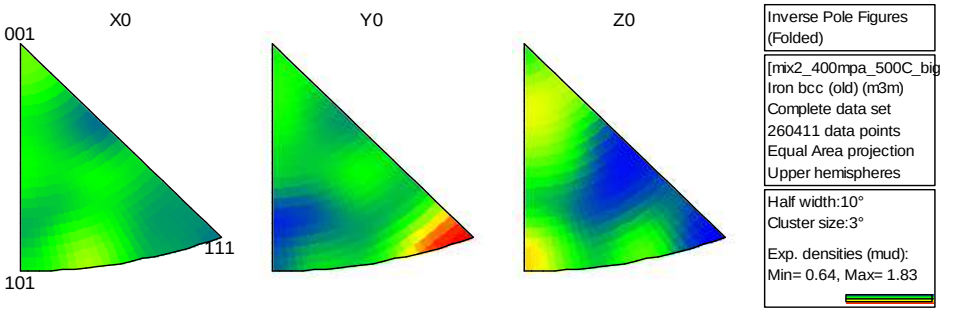

500C

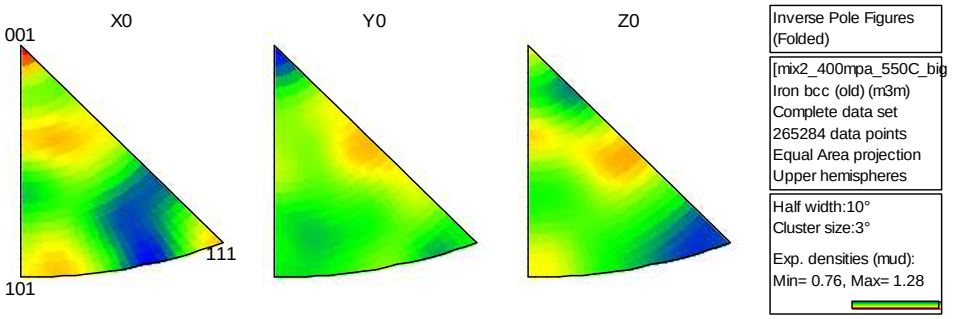

550C

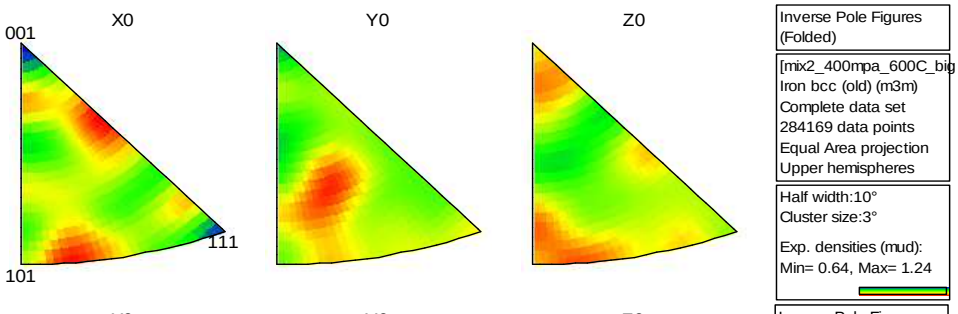

600C

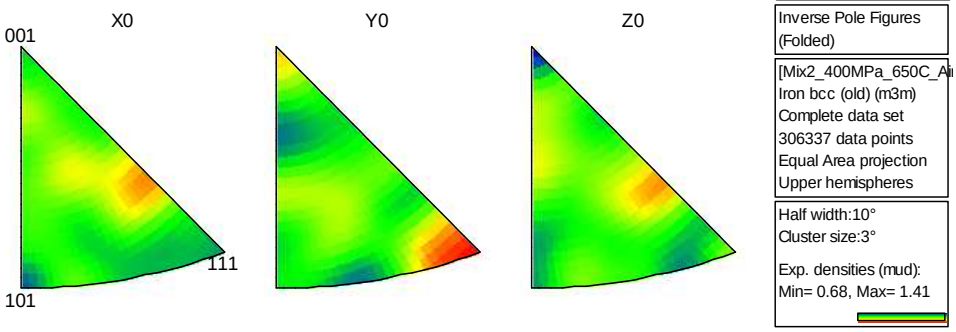

650C

IV. Analysis of Big Areas on the Cross Section of Final Components compacted at 1100MPa

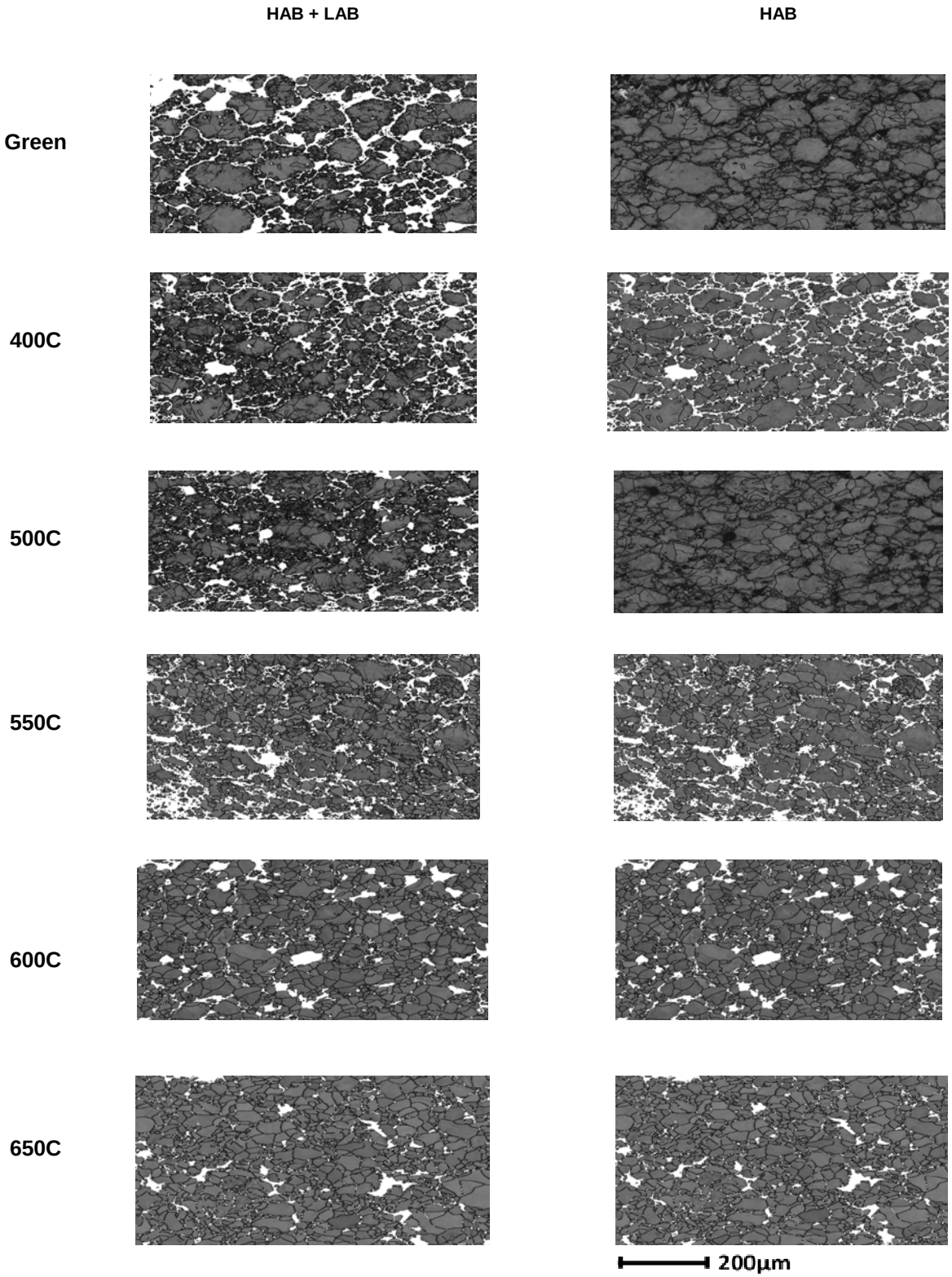

Figure C.xv – LAB and HAB of larger areas of components compacted at 1100MPa

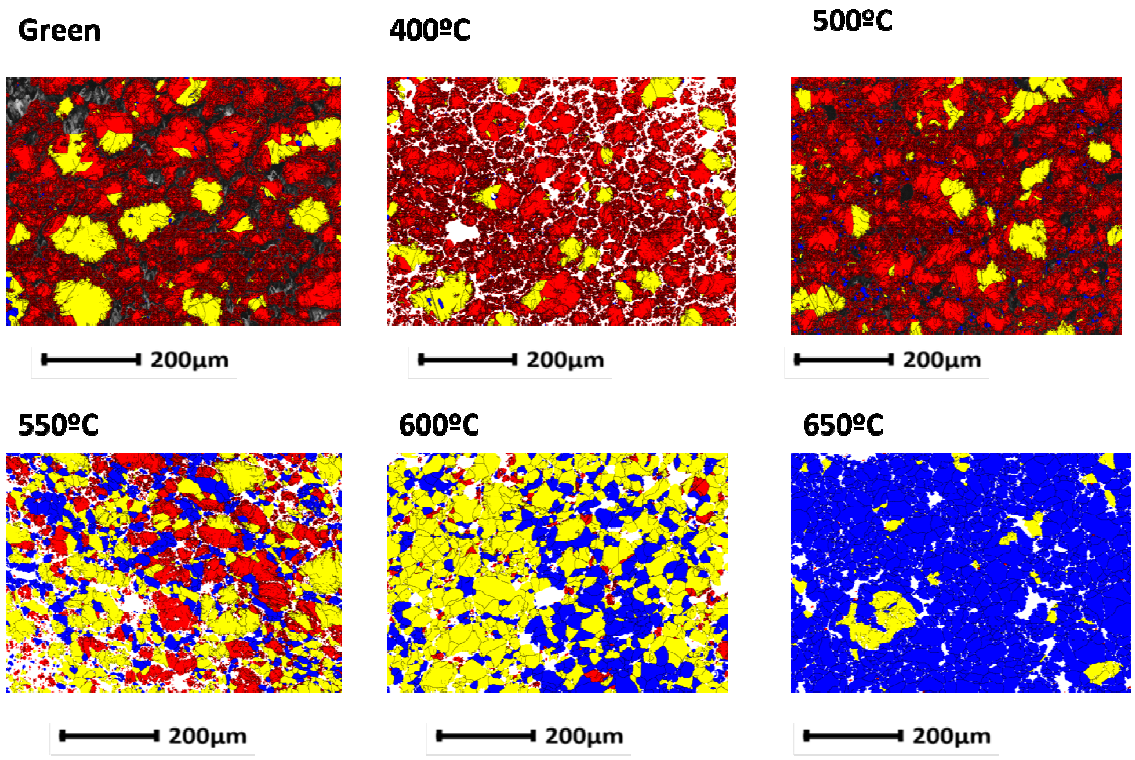

Figure C.xvi – Recrystallization factor maps of big areas in components compacted at 1100MPa

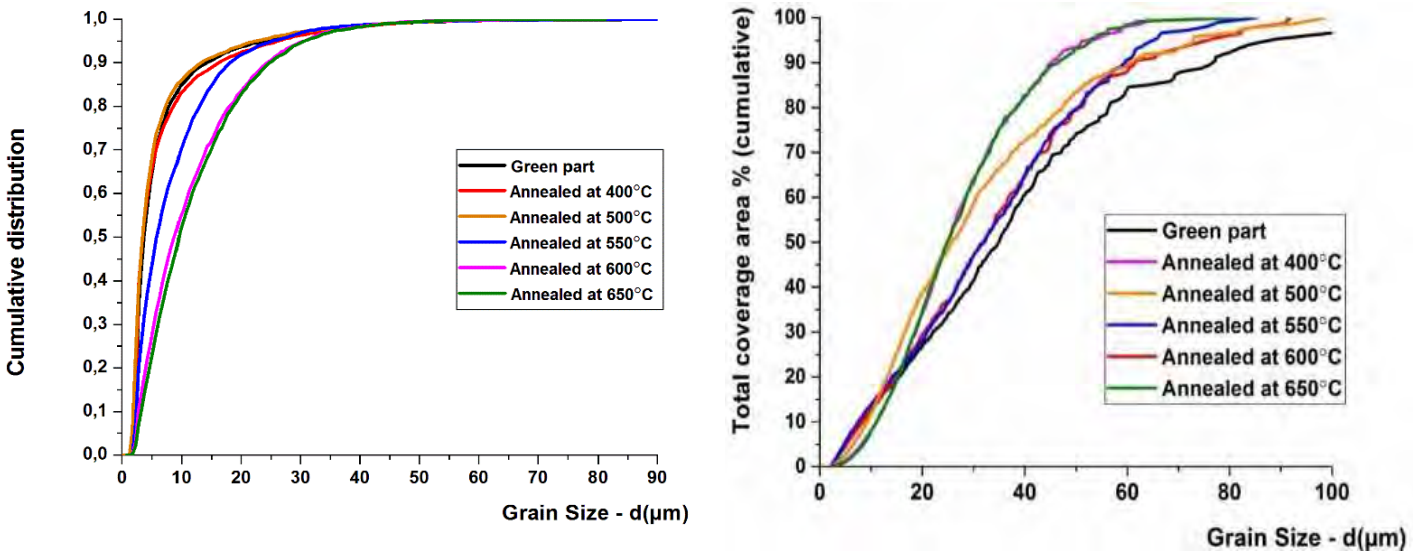

Figure C.xvii – Grain size analysis over cumulative probability plots *(left)* and area coverage plots *(right)* of bigger areas of components compacted at 1100MPa

800MPa	Green	400C	500C	550C	600C	650C
Mean	6,97	7,85	6,53	9,01	11,9	12,5
Median	4,07	3,91	3,91	6,28	9,09	9,84
Max	111,7	82,3	85,3	98,7	64,3	81,3

Figure C.xviii – Mean, median and maximum values of big maps of components compacted at 1100MPa

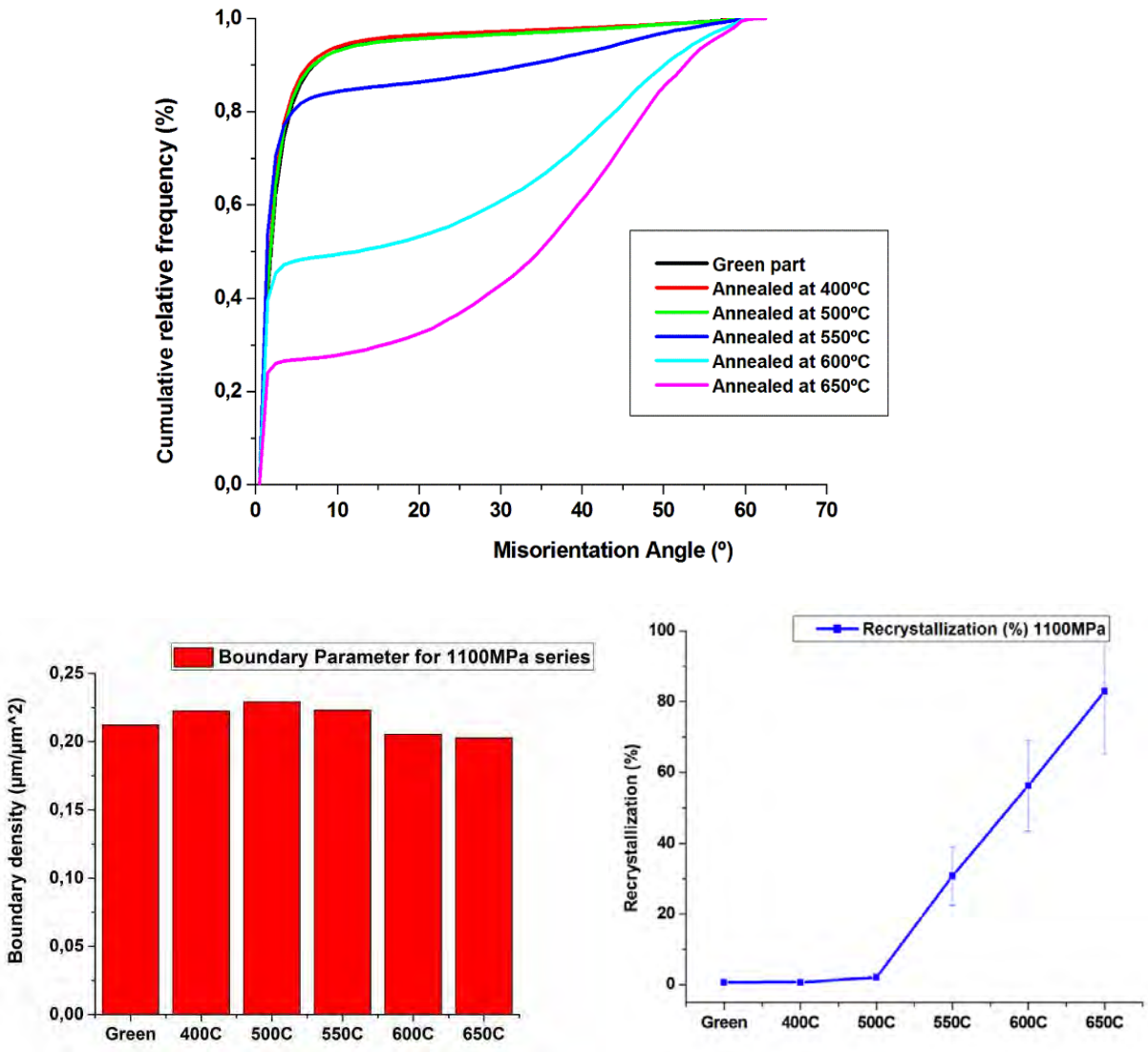

Figure C.xix – Misorientation angle cumulative plot *(upper)*, boundary parameter *(lower – left)* and recrystallization percentage *(lower – right)* of components compacted at 1100MPa

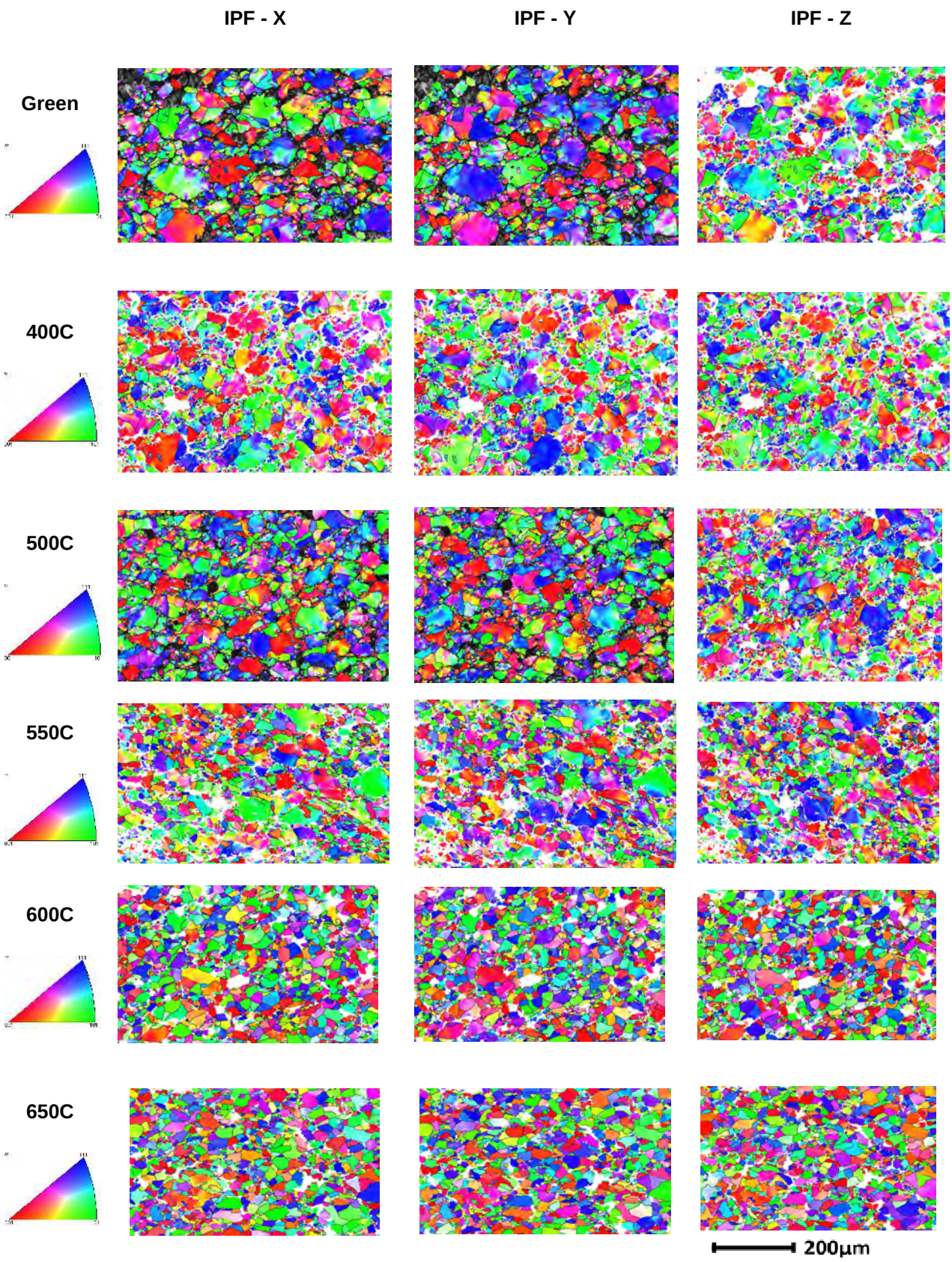

Figure C.xx – IPF couloring maps *(above)* and IPF *(next page)* of big areas of components compacted at 1100MPa

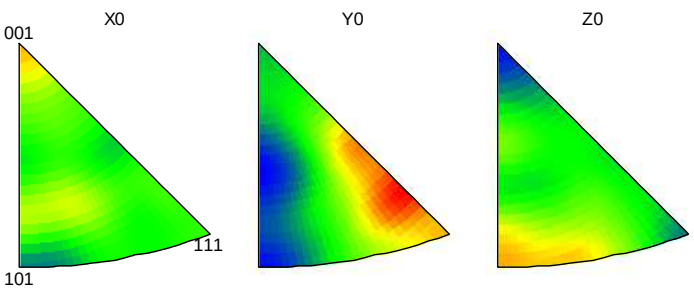

Inverse Pole Figures (Folded)
[mix2_1100mpa_gre.cpr]
Iron bcc (old) (m3m)
Subset1
266382 data points
Equal Area projection
Upper hemispheres
Half width:10°
Cluster size:3°
Exp. densities (mud):
Min= 0.64, Max= 1.49

GREEN

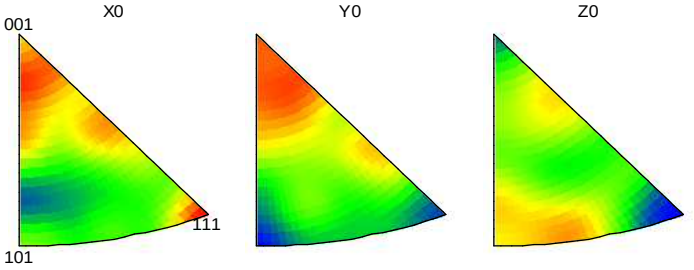

Inverse Pole Figures (Folded)
[mix2_1100mpa_400c.cp
Iron bcc (old) (m3m)
Complete data set
249186 data points
Equal Area projection
Upper hemispheres
Half width:10°
Cluster size:3°
Exp. densities (mud):
Min= 0.68, Max= 1.29

400C

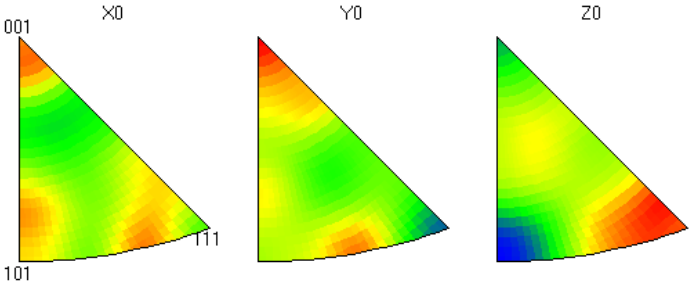

Inverse Pole Figures (Folded)
[mix2_1100mpa_500c.cp
Iron bcc (old) (m3m)
Complete data set
283534 data points
Equal Area projection
Upper hemispheres
Half width:10°
Cluster size:3°
Exp. densities (mud):
Min= 0.65, Max= 1.26

500C

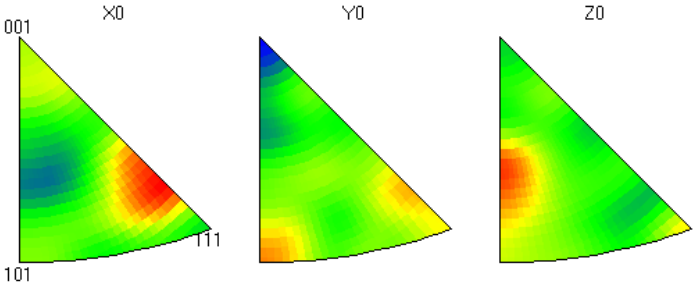

Inverse Pole Figures (Folded)
[mix2_1100mpa_550c.cp
Iron bcc (old) (m3m)
Complete data set
295858 data points
Equal Area projection
Upper hemispheres
Half width:10°
Cluster size:3°
Exp. densities (mud):
Min= 0.75, Max= 1.27

550C

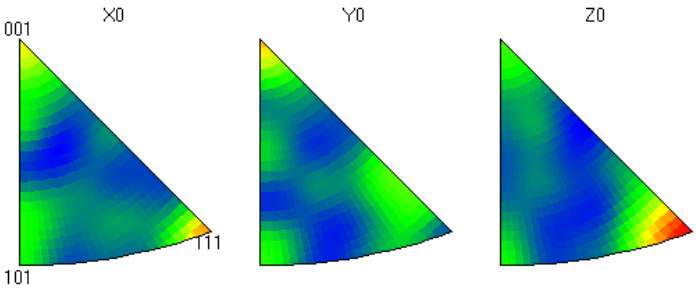

Inverse Pole Figures (Folded)
[mix2_1100mpa_600c.cp
Iron bcc (old) (m3m)
Complete data set
320004 data points
Equal Area projection
Upper hemispheres
Half width:10°
Cluster size:3°
Exp. densities (mud):
Min= 0.83, Max= 1.65

600C

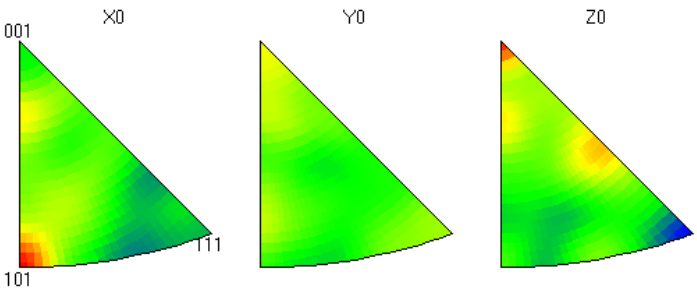

Inverse Pole Figures (Folded)
[Mix2_1100MPa_650C_
Iron bcc (old) (m3m)
Complete data set
324472 data points
Equal Area projection
Upper hemispheres
Half width:10°
Cluster size:3°
Exp. densities (mud):
Min= 0.58, Max= 1.54

650C

Appendix D: Assessment of the compacting and annealing process steps on the performance of finished Soft Magnetic Composite components

(published on EuroPM2015 - Functional Materials - Conference proceedings, 4-7 October 2015)

Manuscript refereed by Dr Yoko Pittini-Yamada (Meyer Sintermetall AG, Switzerland)

Christos Oikonomou[1] (christos.oikonomou@chalmers.se), Daniel Castillo Gutiérrez[2] (danicastillogutierrez@gmail.com), Miguel Monclús[3] (miguel.monclus@imdea.org), Jon Mikel Molina-Adareguia[3] (jon.molina@imdea.org), Lars Nyborg[1] (lars.nyborg@chalmers.se)

[1] Department of Materials and Manufacturing Technology, Chalmers University of Technology, SE-41296 Göteborg, Sweden
[2] Universidad Carlos III de Madrid, Av. de la Universidad, 30, 28911 Leganés, Madrid, Spain
[3] IMDEA Materials, C/ Eric Kandel, 2, Tecnogetafe, 28906 Getafe, Madrid - Spain

Cores for electromagnetic applications made of Soft Magnetic Composite (SMC) materials consist of individually electrically insulated magnetic iron particles, processed by conventional powder metallurgy (PM) routes. The core loss characteristics of a finalized SMC component are related to the process treatments that it has been subjected to. In this context, the effect of uniaxial compaction and annealing steps has been assessed for different pressure and temperature regimes by means of electron backscatter diffraction (EBSD) and nano-indentation techniques. Deformation maps obtained with EBSD were coupled with nano-mechanical testing, denoting the degree of induced stresses and their relaxation in the cross sections of the parts. The development of the internal microstructure and extent of mechanical deformation under processing were also evaluated and correlated to the performance of the parts under question. The results reveal a more direct approach for determining the relationship between magnetic properties and processing treatment of SMC components.

Keywords: Electron Backscatter Diffraction (EBSD), nanoidentation, mechanical deformation, internal microstructure, Soft Magnetic Composites (SMC)

1. INTRODUCTION

Soft magnetic materials are typically used in electromagnetic applications for efficient energy generation, transition and distribution. Their utilization comes mainly in the form of cores for inductors and transformers in AC and DC applications [1, 2]. In this context, soft magnetic composite (SMC) materials are being manufactured by conventional powder metallurgy (PM) techniques which offer profitable and sustainable production routes in high volumes [3-5]. Their isotropic nature opens new design possibilities, while their high electrical resistivity provides with significantly reduced core losses in a wider frequency range of applications [5, 6]. These aspects render the SMC materials as strong candidates for such applications and challenge the more traditionally used laminate steels and ferrites [4]. Their concept is based on individually encapsulated pure iron power particles with an electrically insulating coating, which can be mixed with a lubricant or a binder substance before pressed to finished components through uniaxial compaction. A subsequent low temperature heat-treatment is required in order to relax the induced stresses during the compaction process or act also as a curing step if necessary [3, 4]. Thus, the magnetic performance of SMC components is very much depended on the integrity of the insulating coating after all processing steps and additionally to the efficiency of the post annealing treatment. The latter is directly related to the hysteresis losses and permeability of a component, since there is a relationship between the microstructure and amount of plastic deformation of the material to its magnetization. Metallurgical aspects such as anisotropy, residual stresses, impurities, etc. are well known to influence the magnetic domain wall motion of the material [7-9]. Many simulation models that take into account such variables as dislocations density, grain size, and crystallographic texture have been developed over the years to assess their influence in this type of core loses [10-12]. Additionally, numerous magnetic measurement methods also exist operating on different models that attempt to evaluate various contribution to the total losses, though still many ambiguities exists in terms of testing reproducibility and correlation between simulations and

measurements [13]. The present investigations aim to contribute to this effort with a more unambiguous and sophisticated approach in terms of providing the necessary experimental information for accurate simulation. It is thus the scope of the current study to establish a robust methodology that will allow to model and assess the effect of compaction and annealing process steps of SMC components to their magnetic performance. In more detail, the development of internal microstructure, grain orientation and mechanical deformation of powder particles in finished parts after different processing conditions were complementary evaluated by means of electron backscatter diffraction (EBSD) analytical technique and nanoindentation mechanical testing. EBSD is a powerful technique that offers the possibility to characterize and map elastic and plastic stain on the micro level with all the advantages that a microscopic tool as such provides [14, 15]. This information can be well correlated to nanoindentation testing which in turn provides information on local mechanical properties that are related to the local microstructure [16]. Additionally, phase identification, grain size analysis and crystallographic texture information are possible to acquire with less ambiguity to more traditional metallographic methods for fully recrystallized and deformed materials by means of EBSD [17-19]. Finally, the magnetic performance of the SMC parts under questions were tested in different magnetization conditions and the results were correlated to those acquired with the EBSD and nanoindentation techniques.

2. EXPERIMENTAL PROCEDURE

For the purposes of the current study, commercially available SMC powder coated with inorganic insulating layer was used as base material. The grade was admixed with 0.5 wt. % of organic lubricant and subsequently pressed at room temperature with uniaxial compaction technique at 800MPa. The samples were prepared in toroid shape with an inner diameter of 45 mm, outer diameter of 55 mm and height of 5mm. Post heat-treatment was performed in a non-reducing atmosphere at 400°C, 500°C, 550°C and 600°C temperature regimes. Prior to their magnetic testing, the magnetic toroids were coiled with copper wire having a drive and a sense windings of 100 turns each. The core losses of all samples were measured using a testing system by Brockhaus Messtechnik at 0.5 T, 1 T and 1.5 T from 50 Hz up to 1000 Hz. For EBSD analysis a LEO Gemini 1550 (CARL ZEISS – LEO electron microscopy, Gmbh, Germany) FEG SEM was used, while data evaluation was performed with Channel 5 software from HKL Technology Inc. (Hobro, Denmark). For all measurements 20 kV acceleration voltage was utilized with step size of 1 μm over a total area of 0.7 mm^2. All samples were subsequently fractured and their cross sections were polished down to 1 μm finish with diamond suspension followed by a final abrasive polishing with colloidal silica suspension of 0.04 μm particle size. The same samples were subsequently used for nanoindentation measurements at the previously analyzed areas with EBSD, in order to correlate the acquired information with both techniques. For that purpose, a Triboindenter TI 950 (Hysitron Inc., Minneapolis, MN, USA) instrument was used in force control testing mode, at a maximum value of 10.000 μN. For each sample an array of 10x10 indentations was performed at an imposed maximum depth of 200nm with a Berkovich type indenter. The spacing between indents was set at 5μm in both vertical and horizontal directions.

3. RESULTS AND DISCUSSION

In **Figure 1** the coupling between the nanoindendation and EBSD techniques is shown for small cross sectional areas of single powder particles in SMC samples processed under different conditions. At the EBSD maps (middle images) band contrast information, used as a background, is overlaid with the low ($2° < \theta < 15°$) and high ($\theta > 15°$) angle boundaries. The presence and density of low angle boundaries is related to the plastic deformation of the material and the amount of plastic strain present in the form of dislocation density [14]. The band contrast exhibits the quality of the diffraction patterns and can be used as qualitative means for identifying deformed regions where the pattern quality degrades. As it can be observed from these EBSD maps the highly strained regions are located at the interparticle contacts or at internal pores/defects and for such size of powder particles the main interior volume appears to have sustained less deformation. Additionally, with increasing annealing temperature it is evident that the density of dislocations is significantly reduced denoting the start of recovery process, while the grain structure as indicated by the high angle boundaries is changing with the presence of an increased amount of smaller and more equiaxed sized grains that point out to recrystallization. These observations correlate well with the nanoindentation measurements at regions of the powder particles where areas of high and low density of low angle boundaries exist according to EBSD. Indeed, as shown in the contour maps (right images) in **Figure 1**, for all conditions investigated there is a wide range of nano-hardness values that covers those areas. In more detail, the green component as expected holds the highest nano-hardness values due to its high amount of

deformation while the lowest values were observed for the component heat-treated at 600°C at the areas where the density of low angle boundaries was minimum. Moreover, it can be observed that at the parts annealed at 500°C and 550°C new recrystallized grains exist at the border of the powder particles that nucleate and grow from highly stressed regions. These small grains have lower nano-hardness values and also appear to be “clean” in terms of low angle boundary presence as shown by EBSD.

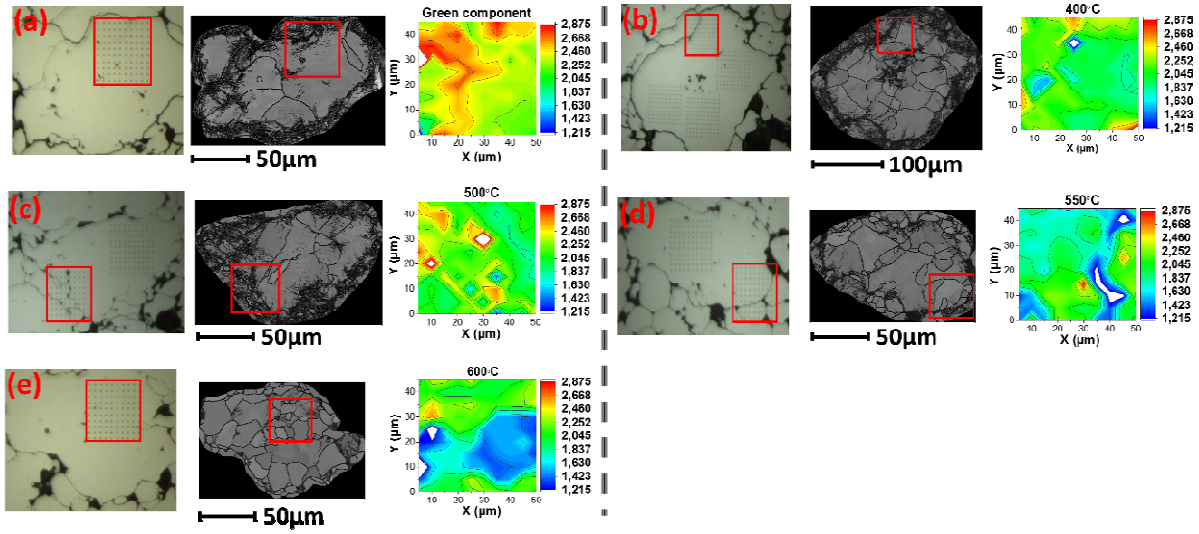

Figure 1: Nanoindentation measurements and EBSD maps on single powder particles for (a) green part, (b) 400°C, (c) 500°C, (d) 550°C and (e) 600°C.

Based on such information, deformation maps that assess the amount of recovered/recrystallized, substructured and deform material present can be acquired from larger areas. In **Figure 2** such maps are shown for all processed conditions, while in **Table 1** the percentages are summarized for each area in every case. It can be seen that for the green components and up to 500°C the amount of deformation reaches values of 80% of the total area measured. This percentage though dramatically decreases at 550°C and 600°C to approximately 3%. Moreover, the substractured areas which are bounded by low angle boundary regions have lower fraction in all cases and continuously decrease with increasing annealing temperature down to approximately 10% at 600°C. It can be seen from such maps that deformed regions have high density in low angle boundaries while the recovered/recrystallized are practically free. Furthermore, big particles tend to retain more substructure areas whereas smaller grains is size appear to be more heavily deformed even at higher temperature. Hence, there is a direct link that can be assessed with this method between the amount of deformation during compaction and annealing process steps and with the particle size distribution of the base material.

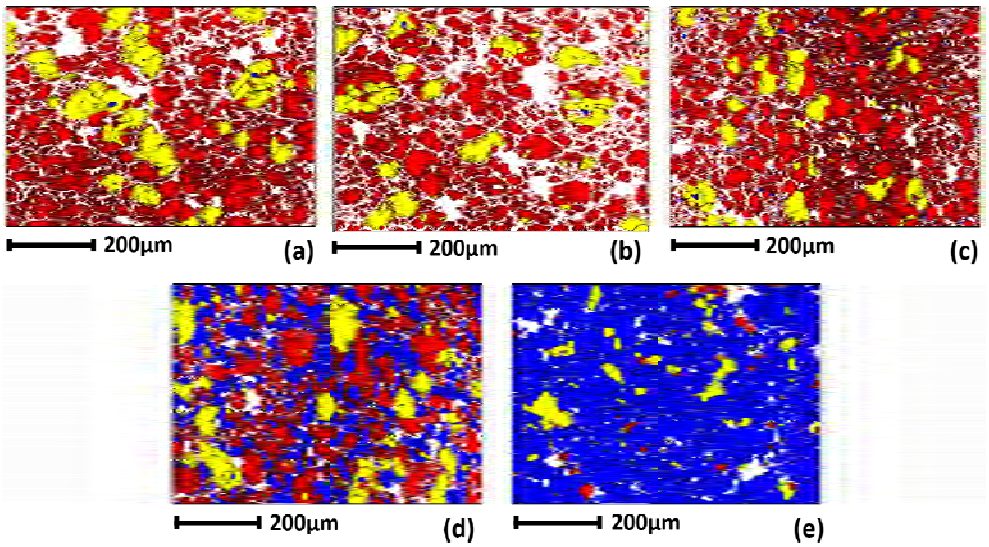

Figure 2: Recrystallization maps overlaid by low angle boundaries (2°< θ <15°) for (a) green part, (b) 400°C, (c) 500°C, (d) 550°C and (e) 600°C. Red colour represents deformed areas, yellow is for substructured and blue for recovered/recrystallized regions. Low angle boundaries are depicted with black colour.

In **Figure 3,** all components are represented in all Euler angles for the same large areas as before and overlaid by high angle boundaries. Every colour represents certain orientation and is assigned to every measured point. For all processed SMC parts it can been seen that the orientation of the grains in space appear to have random directions. This can be better illustrated by using pole figure in respect to certain crystallographic orientations as shown in the same figure for {100}, {110} and {111} plane families. The intensity of the contours represented by rainbow scale was lower than 2.2 m.u.d in all cases and the distribution of the measured points was uniform in respect to all axis (X_0, Y_0, Z_0). These results indicate that there is no preferential texture in the material after compaction and also that it retains its isotropic behaviour after annealing in different temperatures. Additionally, in many cases the crystallographic gradient within grains can be noticed, especially at larger powder particles, which is associated with the presence of substructure in the material and its degree can also be assessed.

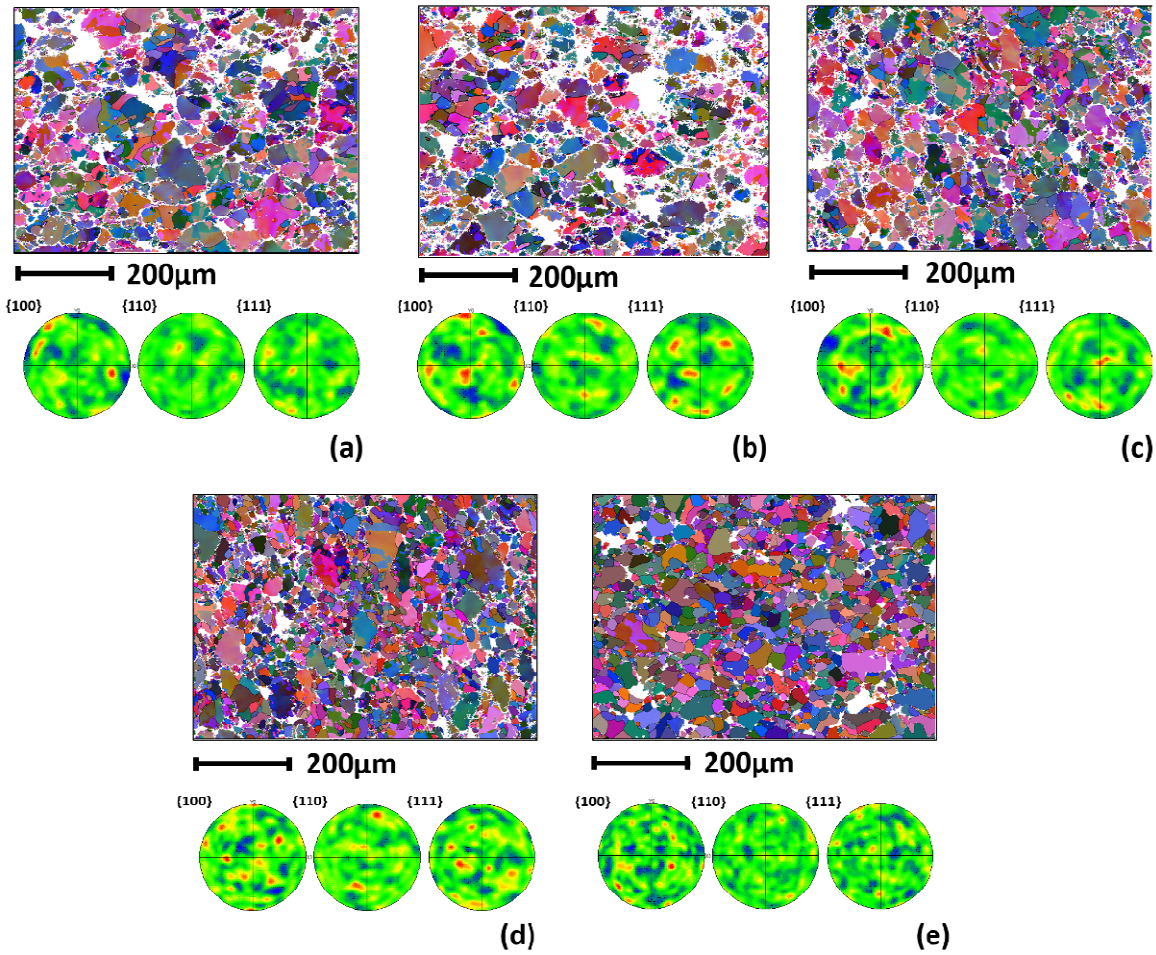

Figure 3: All Euler angles maps overlaid by high angle boundaries (θ > 15°) and their respective {100}, {110} and {111} pole figures for (a) green part, (b) 400°C, (c) 500°C, (d) 550°C and (e) 600°C.

	Deformed (%)	Substructured (%)	Recrystallized / Recovered (%)	Mean value (µm)	Median value (µm)
Green part	79.3	20.1	0.6	7.5	4
Annealed at 400°C	69.7	29.5	0.8	7.1	3.7
Annealed at 500°C	80.9	16.5	2.6	6.6	3.9
Annealed at 550°C	56.4	17.8	25.8	8.1	5.4
Annealed at 600°C	3.2	10.3	86.5	11.7	9.3

Table 1: Recrystallization fractions of all SMC components along with mean and median values from their particle size analysis.

The grain boundary analysis possibilities offered with EBSD technique reveal information such as grain size statistics, misorientation profiles and grain boundary density that can be evaluated with a more unambiguous manner than traditional metallographic methods. In **Figure 4** the cumulative grain size distributions are shown for all SMC processed components based on the equivalent circle diameter method, while on **Table 1** the mean and median values of the distributions. A distinct difference, especially at the lower sized grains between 2 μm and 10 μm range, can be observed for the samples heat-treated at 550°C and 600°C towards higher values with the latter having larger grains. The median values of the distributions also denote the fact that at 550°C and 600°C the distribution is shifter to higher values as compared to the green state and lower annealing temperatures. Moreover, the high angle grain boundary density profile plotted at **Figure 4** for all SMC components shows that there is an increase at the grain boundary interface from green state to 400°C and a maximum at 500°C, which begins to decline from 550°C. These results point to the onset of recrystallization stage and can well correlate with the previous nanoindentation measurements on small grains close to the interparticle regions that showed lower nano-hardness values for these temperature regimes. In addition, the increase in grain size at 600°C indicate also the onset of grain growth to the material. A comparison of the angle misorientation profiles of the correlated grain boundaries, i.e. between neighboring boundaries, shows a great reduction in frequency at the low angles ($2° < \theta < 15°$) after 550°C and especially at 600°C. These are related to the deformed regions where the dislocations density is high and can be used as an indication for the ending of the recovery stage of the material. Combining this information with the grain size distribution and grain boundary length one can identify that the recovery and recrystallization stages overlap to a certain extent and under which processing conditions that occurs.

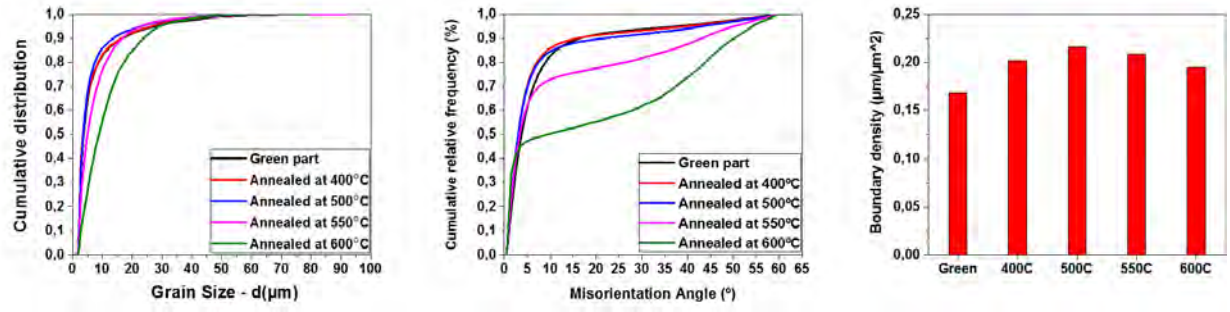

Figure 4: Cumulative grain size distribution based on equivalent circle diameter method (*left*), misorientation angle (*middle*) and grain boundary density profiles (*right*).

In **Figure 5** the results of the magnetic testing of all SMC parts are shown for different induction and frequency values. By dividing the total losses with the frequency, the hysteresis losses which are attributed to the material's properties are represented by a constant value at the plot, i.e. at 0 Hz where the linear fit meets the ordinate, while the eddy current losses become a linear relationship to the applied frequency. The hysteresis losses as shown here are highest for the green part and reduced gradually with increasing annealing temperature. Moreover, the lowest values exist for the parts treated at 600°C at 0.5T, while with increasing induction level the components at 550°C and 600°C tend to have similar values. These results can correlated best with the great reduction observed at the low angle boundary frequency for these temperatures and with the increased recrystallization fraction as observed from the previous analyses.

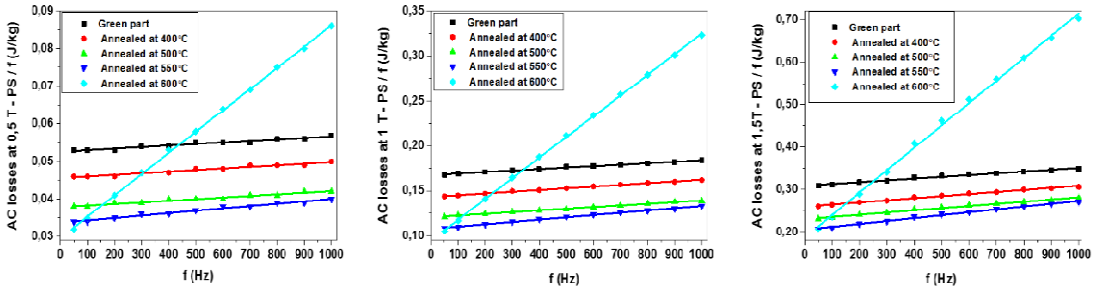

Figure 5: Core losses at different inductions and frequencies for all SMC processed components.

4. CONCLUSIONS

In the present study, the coupling between EBSD and nanoindentation techniques was demonstrated in investigating the deformation behaviour and microstructure development of SMC finished components under compaction and annealing process treatment steps. Microstructural characteristics such as grain size distribution, grain boundary relationship and density, as well as the degree of deformation, were quantified using the aforementioned techniques. It was shown that it is possible to assess the onset of the recovery and recrystallization stages in the material in an unambiguous manner. Finally, the results from the aforementioned investigations were correlated with experimental measurements of magnetic testing that were performed for different induction and frequency conditions.

5. REFERENCES

[1] O. Gutfleisch, M.A. Willard, E. Bruck, C.H. Chen, S.G. Sankar, J.P. Liu, *Magnetic materials and devices for the 21st century: stronger, lighter, and more energy efficient*, Advanced materials, 23, 7, (2011) 821-842.

[2] W.T. McLyman, *Transformer and Inductor Design Handbook - Fourth Edition*, Taylor and Francis Group, LLC, (2011)

[3] M. Persson, P. Jansson, A.G. Jack, B.C. Mecrow, *Soft Magnetic Composite Materials - Use for Electrical Machines*, IEEE Conference Publication, No. 412, (1995), 242-246.

[4] H. Shokrollahi, K. Janghorban, *Soft magnetic composite materials (SMCs)*, Journal of Materials Processing Technology, Vol. 189, No. 1-3, (2007) 1-12.

[5] O. Andersson, P. Hofecker, *Advances in Soft Magnetic Composites – Materials and Applications*, International Conference on Powder Metallurgy & Particulate Materials, PowderMet 2009, Las Vegas, Nevada, 2, (2009). ISBN: 978-0-9819496-1-1

[6] L.O. Hultman, A.G. Jack, *Soft Magnetic Composites - Materials and Applications*, Electric Machines and Drives Conference, IEMDC'03, IEEE International, Vol. 1, (2003), 516-522.

[7] C. Kittel, *Physical theory of ferromagnetic domains*, Reviews of Modern Physics, Vol. 21, No. 4, (1949) 541-583.

[8] J.W. Shilling, G.L. House JR, *Magnetic properties and domain structure in grain-oriented 3% Si-Fe*, IEEE Transactions on magnetics, Vol. MAG-10, No. 2, (1974) 195-223.

[9] D.C. Jiles, *Microstructure and Stress Dependence of the Magnetic Properties of steels*, Review of progress in quantitative nondestructive evaluation, Vol. 9, (1990) 1821-1827.

[10] L. Dupre, M.J. Sablik, R. Van Keer, J. Melkebeek, *Modelling of microstructural effects on magnetic hysteresis properties*, Journal of Physics D: Applied Physics, 35, (2002) 2086-2090.

[11] G. Ban, P.E. Di Nunzio, S. Cicale, *Identification of microstructure effects in magnetic loss behaviour of 3.2% SiFe N.O. electrical steels by means of statistical power loss model*, IEEE Transactions on magnetics, Vol. 34, No. 4, (1998).

[12] F.J.G. Landgraf, J.C. Teixeira, M. Emura, M.F. de Campos, C.S. Muranaka, *Separating Components of the Hysteresis Loss of Non-Oriented Electrical Steels*, Materials Science Forum, Vol. 302-303, (1999).

[13] A. Krings, S. Nategh, A. Stening, H. Grop, O. Wallmark, J. Soulard, *Measurement and modeling of iron losses in electrical machines*, Proc. 5th Int. Conf. Magn. Metall., Gent, Belgium, (2012), 101–119.

[14] S.I. Wright, M.M. Nowell, D.P. Field, *A Review of Strain Analysis Using Electron Backscatter Diffraction*, Microscopy and Microanalysis, Vol. 17, No. 03, (2011) 316-329.

[15] L.N. Brewer, M.A. Othon, L.M. Young, T.M. Angeliu, *Misorientation Mapping for Visualization of Plastic Deformation via Electron Back-Scattered Diffraction*, Microscopy and Microanalysis, Vol. 12, No. 01, (2006) 85-91.

[16] C.A. Schuh, *Nanoindentation studies of materials*, Materials Today, Vol. 9, No. 5, (2006) 32-40.

[17] K.P. Mingard, B. Roedbuck, E.G. Bennett, M. Thomas, B.P. Wynne, E.J. Palmiere, *Grain size measurement by EBSD in complex hot deformed metal alloy microstructures*, Journal of Microscopy, Vol. 227, No. 3, (2007) 298-308.

[18] *ASTM E2627-13, Standard Practice for Determining Average Grain Size Using Electron Backscatter Diffraction (EBSD) in Fully Recrystallized Pollycrystalline Materials*, ASTM International, West Conshohocken, PA, (2013).

[19] K. Güth, T.G. Woodcock, L. Schultz, O. Gutfleisch, *Comparison of local and global texture in HDDR processed Nd-Fe-B magnets*, Acta Materiallia, Vol. 59, No. 5, (2011) 2029-2034.